Statistical Characterisation of Long Term Climate Change

Alexander Norman Dalgleish

A thesis submitted in fulfilment of the requirements
for the degree of Doctor of Philosophy
to the
University of Edinburgh
1996

Declaration

This thesis has been composed by myself and it has not been submitted in any previous application for a degree. The work reported within was executed by myself, unless otherwise stated.

Abstract

The strong causality between the Earth's orbital fluctuations and palaeoclimatic variations is ideal for application of many statistical time series techniques. The coincident spectral peaks in both data sets, coupled with physical explanations for this "forcing", allow us to assume an input-output relationship.

Confirmation of the "Milankovitch Theory" has lent heavily on statistical methods, in particular spectral analysis and associated techniques such as band-pass filtering and cross-spectral analysis. We provide a summary of the application of these techniques, including the variety of spectral techniques used.

Analysis in this thesis focuses on four time series, namely SPECMAP, Ocean Drilling Program site 677 oxygen isotope record, Devil's Hole oxygen isotope record, and a magnetic susceptibility record from Chinese Loess deposits.

We introduce the technique of Complex Demodulation, which, unlike spectral analysis, can indicate variations in the strength and phase of periodicities in a time series. Amongst other results, this confirms the modulation of the precession periodicity (23 ka) by eccentricity, and highlights phase variations consistent with possible dating errors.

Having established independently the orbital forcing, we then proceed to model the palaeoclimatic variations as a function of the past orbital fluctuations. Simple linear modelling confirms some relationship between the two data sets, but cannot reproduce the magnitude of the ice age variations nor the rapidity of the deglaciations. This is indicative of possible nonlinearity in the Earth's response to orbital variations. However, linear models do suffice for hindcasting of palaeoclimatic records when used in conjunction with the transformation of an existing time series.

The AVAS and ACE techniques allow us to model the possible nonlinearity suggested by linear models. Comparison of AVAS and ACE led us to concentrate on application of AVAS, for theoretical and practical reasons. Results indicate

that the effect of precession is linear, with perihelion near vernal equinox corresponding with warmer climate. Obliquity's effect is also generally linear, though with a stronger warming for very high values. The role of eccentricity is more difficult to interpret. Northern hemisphere summer insolation variations were prescribed as a regression variable but proved to be redundant.

Interaction modelling, using Generalised Additive Models, allows us to visualise the combined effect of two orbital variables. This confirms the combined role of high obliquity and vernal perihelion in the deglaciations, and also permitted the last 200 ka to be reproduced independently of eccentricity.

The cause of the deglaciations, and therefore the Earth's 100 ka ice age cycle, is the combined warming effect due to precession and obliquity variations (during a glacial period), and not eccentricity (other than through its modulation of the precession effect). We therefore conclude that the Earth's ice age cycle operates as follows:

- The Earth naturally accumulates ice;
- After a period of ice accumulation an internal threshold or positive feedback mechanism is activated, leading to a glacial collapse. Possible mechanisms for this are the internal dynamics of the great ice sheets, or positive feedback due to the expansion of the mid-latitude forests;
- This collapse is triggered by the warming pulse which results from high obliquity and autumnal perihelion, possibly due to the extended summer experienced in the Northern hemisphere during such an orbital configuration.

Acknowledgements

My first thanks must go to Geoffrey and Eric for initiating and supervising such an interesting and stimulating project. The whole subject area of this thesis constantly amazed me, and I am grateful to have had the opportunity to study it in such detail. Eric is also thanked for attempting (in vain?) to improve my grammar, and Geoffrey for all the opportunities to travel, particularly the two weeks of free Chianti in Tuscany! I would also like to thank Dr Eddie McKenzie, Strathclyde University, for his invaluable help with chapter 5.

This project was carried out as part of the EC project "Simulation of the effect of long term climatic change on groundwater flow and the safety of geological disposal sites", EC project no. F12W-CT90-0046.

Thank you to the University of Edinburgh, and specifically the staff of the Geology and Geophysics department.

This thesis was formatted using LaTeX (Lamport.L. 1985, Kopka and Daly 1993), and the postscript figures were generated using the S-Plus (Becker et al. 1988, S-PLUS 1996) software package.

The following people all helped me by reading through early drafts of the chapters: Alastair, Grandpa, Marianne, Nikki and Trevor.

Many people contributed to making my life in Edinburgh the joy that it was. Of the people who have shared large quantities of that life, I particularly want to thank Alastair, Baz, Dave, Jon and Mandy, for introducing me to Underworld, climbing (and carrot cake!), the important things in life, Nick Hornby and Wendolene. To my other friends, be they in/around/from/no longer in/completely unrelated to Edinburgh, thank you.

I would like to thank my Granny and Grandpa for all their help and encouragement, and being my two oldest "best friends" in Edinburgh.

Finally, I wish to thank my Mum and Dad for everything they have given me over the last 26 years. I love you both.

Contents

List of Figures

List of Tables

List of Abbreviations

ap after present

bp before present

Ma Million years

ka thousand years

AVAS Additivity and Variance Stabilisation

ACE Alternating Conditional Expectations

AR Autoregressive

ARIMA Autoregressive Integrated Moving Average

CD Complex Demodulation

GAM Generalised Additive Model

RV Random Variable

SD Standard Deviation

TSA Time Series Analysis

e Eccentricity

ϵ Obliquity

ω In orbital terms, the angle between the perihelion and the vernal equinox

W Watts

ELA Equilibrium Line Altitude

O^{18}, C^{14} etc. Isotopes of the elements

LGM Last Glacial Maximum

MIS Marine Isotope Stage

Chapter 1

Introduction

Over 150 years ago Louis Agassiz discovered compelling evidence that the world had experienced a great cold period (Agassiz 1840), and subsequent work confirmed that this was not a unique event. The question then arose: what caused these "Ice Ages"?

1.1 The Climate of the Quaternary

The Quaternary is the latest geological period, and extends from the present day back to 1.8 Ma bp. This is the time period of interest in this thesis.

Figure 1.1 shows the SPECMAP time series for the last 782 ka, as derived by chemical analysis of the oxygen isotope variations in deep ocean cores. Positive values indicate cooler times and negative values signify warmer times. The recent climate has been dominated by a regular glacial/interglacial cycle: the Earth grows steadily colder towards a glacial maximum, and then rapidly warms into an interglacial, with seven repetitions of this cycle in the last 700 ka, giving an average period of 100 ka. Figure 1.1 also shows the concurrent variations in solar energy received by the Earth at high Northern latitudes in the summer.

Figure 1.2 contains spectral analyses of the SPECMAP record and the insolation record for latitude 65° North in the summer. Peaks in this analysis represent periodicities in the data. The SPECMAP analysis contains a dominant 100 ka period, and then further higher frequencies at approximately 41, 23 and 19 ka. The 41, 23 and 19 ka periodicities also appear in the insolation record, but not the 100 ka. In the following sections we will discuss the sources of these rhythmic variations.

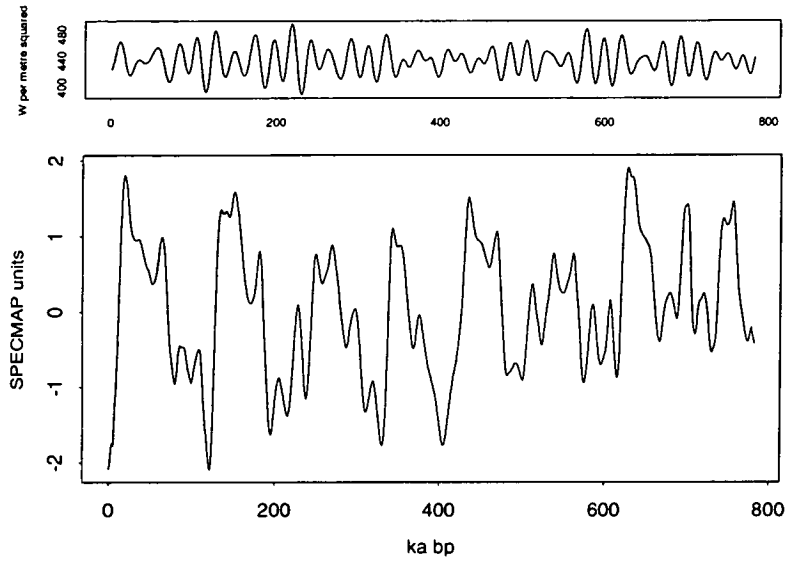

Figure 1.1. Top: the variations in insolation received by the Earth at latitude 65° North in July for the last 800 ka (Berger and Loutre 1991). Bottom: the SPECMAP record, indicating the succession of Quaternary ice ages. Positive values indicate periods of high ice volume (cold), and negative values indicate more temperate periods, such as the present day (Imbrie et al. 1984).

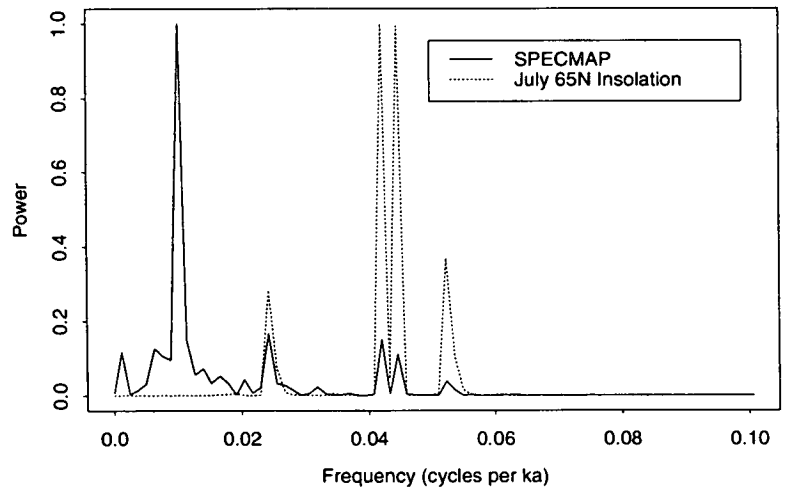

Figure 1.2. Spectral analysis of the SPECMAP record, showing the presence of periodicities at 100, 41, 23.7, 22.4, and 19 ka, and the corresponding analysis of the latitude 65° North insolation changes which contains four of these periodicities.

1.2 The History of the Astronomical Theory

The early Ice Age theories covered a wide range of physical explanations, such as solar variability, carbon dioxide variations, epochs of high volcanic activity, or even dust-clouds in outer-space (Imbrie and Imbrie 1979).

It was relatively soon after Agassiz's discovery of widespread glaciation that Joseph Adhemar first suggested a connection between the ice ages and variations in the Earth's orbit around the Sun (Adhemar 1842), the beginning of the "Astronomical Theory". In particular, Adhemar reasoned that, due to the precession of the equinoxes, the two hemispheres of the earth would experience alternating glaciations, citing the Antarctic ice sheet as evidence of the present Southern hemisphere glaciation.

Urbain Le Verrier first demonstrated that the eccentricity of the orbit must be constantly changing (Le Verrier 1855). It occurred to the Scotsman James Croll that these eccentricity variations could be the cause of the glacial periods, and he was the first to publish this idea (Croll 1864). Croll calculated the eccentricity for times during the last 3 million years and noted the cyclical nature of its variations. Croll reasoned that as winter was the key season for snow accumulation it must therefore be the critical season with regards to producing an ice age. Ultimately, Croll concluded that both precession and eccentricity must play important roles in regulating the winter temperatures and thus the occurrence of ice ages. This is summarised in Figure 1.3 which indicates the alternating Northern and Southern hemisphere glaciations during periods of high eccentricity.

The astronomical theory could not be tested until an accurate chronology for the ice ages had been produced. The first estimate of the timing of the last glaciation came from Niagara Falls. Estimates of the time taken to erode the gorge downstream of the falls gave a date of 10 ka bp for the ice retreat. This conflicted with Croll's estimate as Figure 1.3 implies that the last Northern hemisphere glaciation ended approximately 80 ka bp. This, allied to further geological evidence and meteorological calculations on the magnitude of solar heating, led to a loss of interest in Croll's theory.

The flag of the astronomical theory was next taken up by the Yugoslavian Milutin Milankovitch, the man whose name would eventually become synonymous with the theory of orbital forcing of climate. In 1904 the German mathematician Ludwig Pilgrim had published his calculations of all three key astronomical

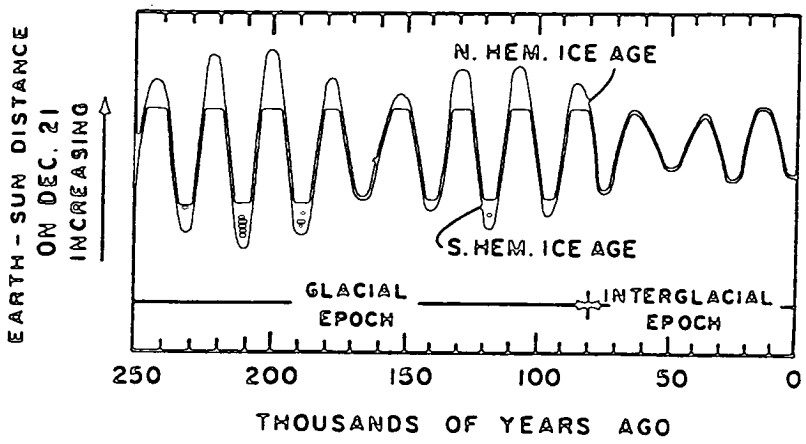

Figure 1.3. The results of Croll's work on the combined effect of variations in eccentricity and precession of the equinoxes. During periods of high eccentricity the hemisphere experiencing a winter solstice far from the sun (near the aphelion) will be in a glacial state. This figure is from Imbrie and Imbrie (1979).

variables: eccentricity, obliquity, and precession. Milankovitch utilised these values to calculate the amounts of solar radiation striking the Earth during each season and at each latitude. Milankovitch also calculated these values for Mars and Venus. Following the publication of this mathematical description of the climate of these three planets, Milankovitch began working with the climatologist Wladimir Koppen. Following discussions with Koppen, Milankovitch calculated the summer radiation at latitudes 55°, 60°, and 65° North back to 650 ka bp, and these matched well with glacial data available at the time. These results were published in Koppen and Wegener (1924) and Milankovitch went on to publish extensively on the subject (Milankovitch 1936, and other references in Imbrie and Imbrie (1979)). The "Milankovitch Theory" was now well established.

The expansion of the Milankovitch theory has subsequently depended upon the steady advances in two seemingly disparate scientific disciplines. Calculation of the (past and future) orbital and insolation variations has gained in accuracy and temporal coverage (Brouwer and van Woerkom (1950); Sharaf and Boudnikova (1967); Anolik et al. (1969); Bretagnon (1974); Berger (1978a); Berger (1978b); Laskar (1986); Laskar (1988); Berger et al. (1988)). This process culminated in the publication of orbital and insolation values for the last ten million years in Berger and Loutre (1991). The values produced in this paper will form

the basis of all Milankovitch investigations in this thesis.

Concurrent with these astronomical advances was a similar progression in the field of palaeoclimatic reconstruction. Geologists were producing longer climatic time series with improved resolution and dating (see, for example, Arrhenius (1952); Broecker et al. (1968); Kukla (1970); Shackleton and Opdyke (1973)). The breakthrough came in Hays et al. (1976) when spectral analysis confirmed the coincident periodicities in the Milankovitch variables and past climate records. The increasingly complex combination of these two data sets through statistical techniques will be discussed in Chapter 2.

1.3 The Earth's Orbital and Insolation Variations

The motion of the Earth around the sun is a complex process. The orbit is elliptical, with the sun at one of the foci. The axis of rotation is not perpendicular to the plane of the ecliptic (the plane containing the orbit), resulting in the annual cycle of the seasons as the Earth progresses round its orbit. In addition, the positions on the orbit of the equinoxes/solstices progress. These various features, and their effect on the receipt of insolation by the Earth, are discussed here.

Figure 1.4 illustrates these variations, and Figure 1.5 shows a plot of the orbital variables for the past 1 Ma.

1.3.1 Orbital Eccentricity

Eccentricity is referred to by e, where

$$e^2 = \frac{a^2 - b^2}{a^2} \tag{1.1}$$

and a and b are the semi-major and semi-minor axes of the orbit respectively. The orbit of the Earth changes from being almost circular to being strongly elliptic, varying in value from almost zero (minimum of 0.000267) to a maximum of 0.057133 during the last 5 Ma. This variation has the effect of increasing the contrast between the seasons in one hemisphere, and reducing them in the other. For example, the present day situation is such that the Northern hemisphere winter is close to the perihelion, and summer is close to the aphelion, thus making the winters milder and the summers cooler. This situation is reversed in the Southern hemisphere. Eccentricity is the only orbital variable which alters the total amount of radiation received by the Earth when integrated over all the

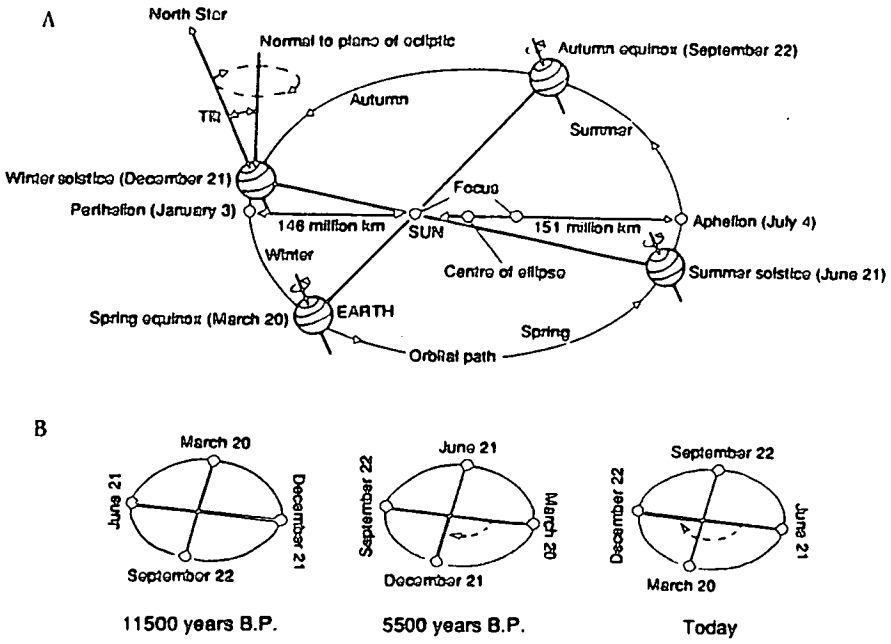

Figure 1.4. A: Geometrical description of the Earth's orbit. The Earth progresses around the orbit in the direction of the arrows, and all dates refer to the present day situation. This illustrates the elliptical nature of the orbit and the seasonal consequences of the Earth's obliquity. B: The effect of the precessing equinoxes. The present situation is that the Northern hemisphere winter solstice occurs shortly before the Earth reaches its point of closest approach to the sun (perihelion). Approximately 11,500 ka bp the winter solstice would have corresponded to the aphelion. From Dawson (1992).

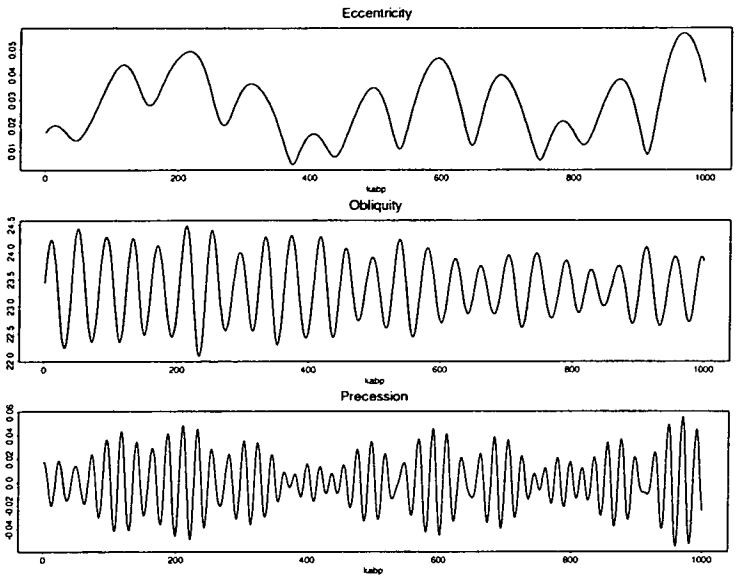

Figure 1.5. The three orbital variables for the last 1 Ma. Obliquity is measured in degrees. Precession is $e \sin \omega$. See text for details. Data from Berger and Loutre (1991).

latitudes and one complete year. The total radiation received is proportional to $(1 - e^2)^{-0.5}$, due to the eccentricity driven variations in the mean distance of the Earth from the Sun. However, this results in variations in the annual radiation budget of less than 0.2%. The main periodicities in the eccentricity variation are 404178, 94782, and 123818 years (Berger and Loutre 1991), but in low resolution spectra these appear as peaks at 400 ka and 100 ka.

1.3.2 Obliquity

The obliquity (inclination) of the Earth's rotational axis, relative to the plane of the ecliptic, varies through time. It has ranged from a maximum of 24.538° to a minimum of 22.079° during the last 5 Ma. The main effect of fluctuating obliquity is to change the quantity of radiation received at high latitudes, with high obliquity leading to higher insolation values towards the poles and a greater range of seasonality. Obliquity has only a minor effect in the tropics. The main periodicity in the obliquity record is 41090 years (Berger and Loutre 1991). We refer to obliquity by ϵ.

1.3.3 Precession of the Equinoxes

We will use the term "precession" to represent "precession of the equinoxes". The Earth's axis of rotation presently points at the Pole Star, but this was not always the case. Through time the axis transcribes a circle in space and consequently the equinoxes (and seasons) "precess" around the orbit (Figure 1.4). The main precession periodicities are 23708, 22394, and 18964 years (Berger and Loutre 1991), and these generally produce spectral peaks at 23 ka and 19 ka. We define the precession variable as the angle between the perihelion and the vernal equinox, and signify this by ω. Precession effects the insolation changes through the formula $e \sin \omega$. This describes how precession changes the seasonal configuration of the Earth-Sun distance, and corresponds to variations in the Earth-Sun distance in June.

1.3.4 Insolation Variations

The orbital variations combine to moderate the insolation received at each latitude throughout the year. Low latitude insolation variations are dominated by eccentricity and precession, whereas obliquity has a stronger effect at high latitudes. Seasonal variations in insolation are important as, for example, a colder winter may have little effect, but a colder summer may enable the snow fields to survive through to the next winter and thus initiate a glacier or ice sheet. In addition, certain latitudes are seen as being particularly sensitive to insolation changes. The mid to high Northern latitudes are sensitive, and therefore important, as they encompass: a large proportion of the Earth's landmasses; many of the Earth's mountainous areas; the source area of the North Atlantic Deep Water (NADW), an important element of the climate system; the areas of the Arctic susceptible to sea ice formation, a highly responsive element of the climate system. For these reasons the insolation curve at latitude 65°N in June/July is often singled out as being the most useful for analysis, or for use as an input to the climate system (Koppen and Wegener 1924, Imbrie and Imbrie 1980). Figure 1.6 shows the insolation values for Northern hemisphere summer and winter for the last 1 Ma. In particular, note the enormous difference in insolation values between the seasons, and yet it will be shown that the relatively small variations in the summer values have a strong effect on climate change.

In Figure 1.2 we observe that, whilst the dominant periodicity in the SPECMAP record is the 100 ka ice age cycle, there is not a significant peak in the insolation

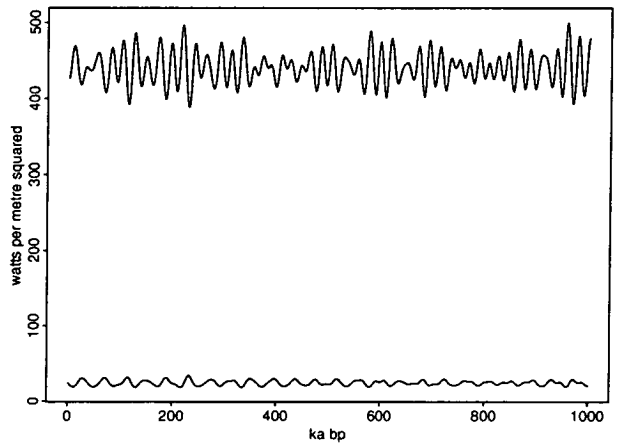

Figure 1.6. Insolation values for 65° North in July and 60° North in December, an indication of Northern hemisphere summer and winter variations. Note the pronounced seasonal differences, and yet the relatively small summer variations are strong enough to drive climate changes. Data from Berger and Loutre (1991).

record at 100 ka. This is because the eccentricity variations have a very small effect on the total amount of insolation received by the Earth. One of the aims of this thesis is to account for this anomaly, and the source of the 100 ka ice age cycle.

In this thesis any discussion of seasonal insolation relates to the Northern hemisphere season, unless otherwise stated.

1.4 Dating

A core of oceanic/terrestrial sediment is extracted, and its chemical composition analysed, thus oroducing a proxy climate indicator. Geologists must then assign a timescale to the data. There are several techniques employed to achieve this, and the selection of which to use is dependent upon the approximate length of the sedimentary record.

1.4.1 Radiocarbon Dating

Prior to the manmade Nuclear explosions of the 1940's, the proportion of Carbon in the atmosphere which was present as C^{14} was in approximate equilibrium. This equilibrium proportion also exists in living tissues, such as new wood or new carbonate shells. The quantity of C^{14} then starts to decay from when the

tissue dies. The half-life of C^{14} is approximately 5700 years, so by measuring its present level of radioactivity it is possible to estimate the age of the sample. There are numerous problems with radiocarbon dating (Bradley 1985), and it is only of practical benefit back to a maximum of 40 ka bp, but it is still one of the most important dating techniques. The pollen data discussed in Section 1.5.4 uses radiocarbon dating.

1.4.2 Other Radiometric Techniques

A wide range of radioactive isotopes exist which can be used for dating over a broad range of timescales. Bradley (1985) and Lowe and Walker (1984) provide detailed descriptions of these techniques. Radiometric dating is particularly useful as it can provide point-estimates of age without the need for a continuous record. For example, Potassium-Argon dating utilises the fact that the radioisotope K^{40} decays to the stable Argon isotope Ar^{40} with a half-life of 1.28×10^9 years. This is useful for dating volcanic or metamorphic rocks, but only for samples older than 100 ka. Argon-Argon dating has recently been applied to lavas in an attempt to clarify the dating of the Earth's magnetic reversals (Baksi et al. 1992) as will be discussed in Section 1.4.3. Uranium series dating ($Th^{230} - U^{234} - U^{238}$) uses the fact that these isotopes all decay to lead. It is believed to be extremely accurate (Ludwig et al. 1992), and was used extensively in constructing the timescale for the Devil's Hole record (Section 1.5.3).

1.4.3 The Palaeomagnetic Record

Through geological time the direction/polarity of the Earth's magnetic field has varied, as indicated in Figure 1.7. These variations enable events to be correlated on a global scale as the reversals are recorded in the magnetic material in the cores. The magnetic reversal events have been dated, although the dates assigned are still under modification (Shackleton et al. 1990). The periods of differing polarity have also been named, with the latest period being known as the Brunhes, and the preceeding one as the Matuyama. However, this technique is not applicable unless the record being dated has intersected one of the reversals, the most recent of which, the Brunhes-Matuyama boundary, occurred at 780 ka bp.

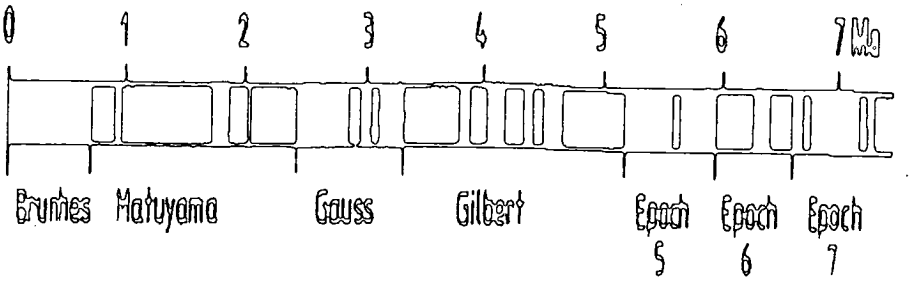

Figure 1.7. The palaeomagnetic record of reversals in the Earth's magnetic field for the last 7 Ma. Black bands represent periods of normal polarity (the present day situation), and white bands periods of opposite/negative polarity. From Jacobs (1994).

1.4.4 Tuning to the Orbital Record

The most commonly used technique for dating palaeoclimate records of sufficient length and continuity is to assume a causal mechanism between the Earth's orbital/insolation variations and the past climate, and then proceed as follows.

1. Assign a rough timescale to the time series of variations in the core. This can be achieved using a limited number of radiometric dates, magnetic reversals, or from correlation of particular events with other previously dated records.

2. Extract the portions of the signal which appear to correspond with the obliquity and/or precession variations. This is achieved using the band-pass filter technique, which we discuss further in Section 2.5.

3. Estimate the time-lag between the orbital variations and the climate variations indicated by the time series.

4. Adjust the data timescale to optimise the correlation between the two filtered records given the time delay.

Given the linear relationship between precession/obliquity and palaeoclimate (Hays et al. 1976) this technique appears well founded. It is vulnerable to accusations of using "circular arguments" as tuning to the orbital record will produce the orbital frequencies in any spectral analysis. However, tuning to a single frequency need not automatically install the presence of the remaining orbital frequencies. In addition, the evidence from untuned data e.g. Kukla et al. (1990), allied with further evidence about the amplitude variations of these periodicities, make it

difficult to argue against the underlying assumptions of "tuning", which is that variations in the Earth's orbit are the underlying drivers behind climate change on this timescale.

1.5 Data sources

Palaeoclimatic data comes from a variety of sources. Here we give a brief introduction to the different data types, their construction, and the information they provide.

1.5.1 Ocean Cores

It was James Croll who first suggested that the sediment on the ocean floor may provide a more complete record of past climates than the fragmentary terrestrial record. Initial palaeoclimate records used the distribution of climate-sensitive foraminifera (microscopic marine organisms) to reconstruct past temperature. Then in 1955, Cesare Emiliani developed a technique for analysing the oxygen isotope variations in the foraminifera (Emiliani 1955). This technique is now widespread. Figure 1.8 describes the method by which, during glacial periods, the lighter O^{16} isotopes are preferentially evaporated from the oceans and stored in the ice sheets. Thus, foraminifera during periods of ice sheet growth will contain a higher proportion of the heavier, O^{18} isotopes.

Two kinds of foraminifera exist, the surface water planktic foraminifera and the bottom dwelling benthic. Thus information can be gained on the isotopic conditions at the top and bottom of the oceans, and at all depths at continental margins.

Interpretation of the isotopic record is further complicated by its relationship with temperature. A drop in water temperature leads to enrichment of the O^{18} values. However, the temperature at the ocean floor is approximately constant, so benthic records indicate the ice volume changes, and planktic records contain the ice volume signal and information on the sea surface temperature (SST) variations.

SPECMAP

The SPECMAP record is the result of work by the SPECMAP (Spectral Mapping) Group (Imbrie et al. 1984). Five deep sea cores were "stacked" together

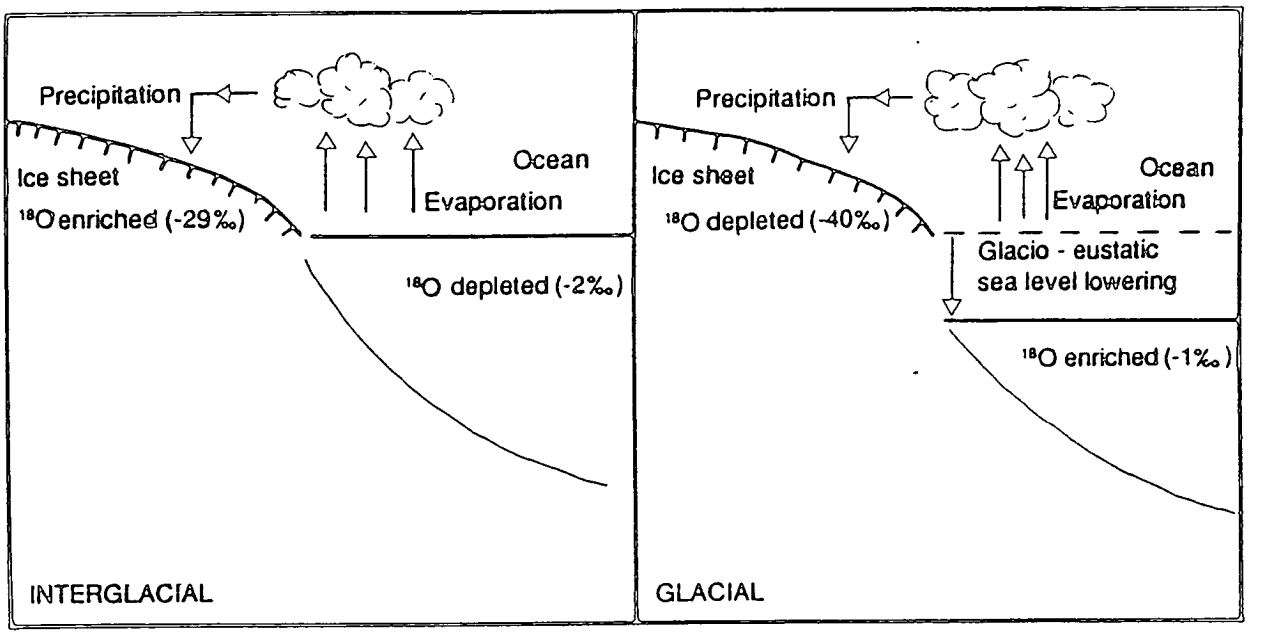

Figure 1.8. A schematic diagram illustrating the processes by which oxygen isotopes are evaporated from the oceans and stored in the ice sheets. During glacial periods the lighter (and therefore more easily evaporated) O^{16} isotopes are stored in the ice sheets. This, combined with the concurrent reduction in sea level, leaves the oceans relatively enriched in the rarer O^{18}. The O^{18} values shown are typical values per millilitre relative to O^{16}. From Dawson (1992).

by averaging and smoothing, and a timescale assigned by matching the filtered elements of the time series to those of the orbital forcing. This technique has become known as "tuning". The stacking process reduced the local temperature component, leaving a dominant ice volume component. The data are thought to signify changes in global ice volume, and hence to be at least a measure of Northern hemisphere climate (as the majority of global ice variations occur in the Northern hemisphere).

The resultant time series extends back to 782 ka bp, and is shown in Figure 1.1. Recent work has suggested that there is an error in the dating of the record at 617 ka bp (Shackleton et al. 1990, Thomson 1990a), a result of missing one of the orbital cycles in the tuning procedure.

Aside from the dating error, the SPECMAP record is an excellent estimate of the past variations in Northern Hemisphere glaciation, and therefore an indicator of global climate.

Ocean Drilling Program

The Ocean Drilling Program (ODP) is an organisation which carries out scientific cruises to all parts of the World's oceans, collecting sediment and rock cores. These are then analysed and the extensive results database is the most globally and temporally comprehensive source of palaeoclimatic information. In this thesis the oxygen isotope record from one such core will be analysed: the ODP Site 677 record (ODP Shipboard Scientific Party 1988), as shown in Figure 1.9.

The ODP Site 677 is in the low-latitude Pacific, and neighbouring cores indicated that the sedimentation rate had been high enough in that area to reveal a detailed climatic record. The isotope record was dated by the tuning technique, and the resolution was considered high enough that the magnetic reversal events were not used as dated tie-points. This resulted in new, older age estimates for the reversals (Shackleton et al. 1990), dates which were subsequently confirmed by radiometric analysis, such as Ar^{40}/Ar^{39} dating in Tauxe et al. (1992).

Marine Isotope Stages

Emiliani was the first to introduce the notation of Marine Isotope Stages (MIS), the simple numbering of the key climatic periods during the Quaternary and Pliocene. Figure 1.10 shows an isotope record and the stage divisions. Odd numbered stages are "warmer", and even numbered stages are "cooler". This

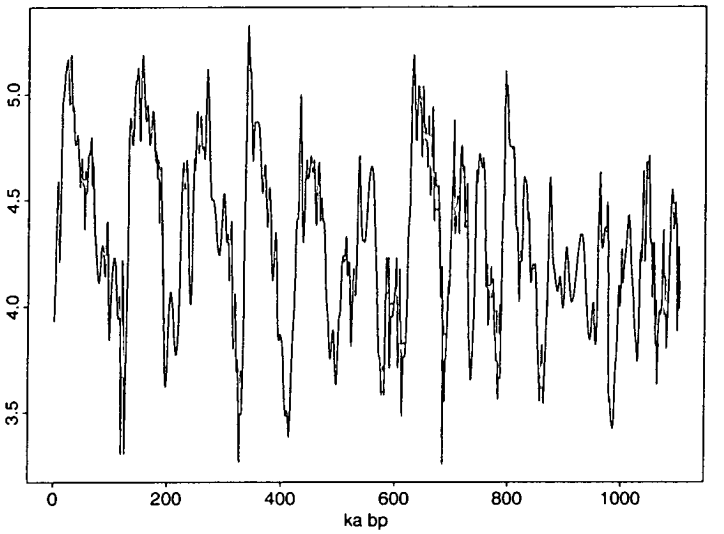

Figure 1.9. The benthonic oxygen isotope record from ODP 677. Units are standard O^{18} units. Data from ODP Shipboard Scientific Party (1988).

numbering system is used to easily identify particular events in the analyses.

1.5.2 Loess

Loess is the accumulation of wind-blown dust in the barren areas surrounding ice sheets. Loess layers, deposited during glacial periods, alternate with soil layers from vegetation present during the interglacials.

In this thesis a 1 Ma record of magnetic susceptibility as recorded in the loess accumulated in China is analysed (Kukla et al. 1990). Like the SPECMAP record, this loess time series is a stacked record, produced from the combination of three separate susceptibility records.

Magnetic susceptibility is a measure of the temporary magnetisation induced in a sample by the application of a low amplitude magnetic field. This is dependent upon the composition, concentration and grain size of the magnetic minerals present (Kukla et al. 1990). Susceptibility values are high in soils and low in loess.

The dating of the record uses the geomagnetic polarity timescale, but is independent of the orbital variations (i.e. the data is not tuned). This enables a direct spectral analysis verification of the Milankovitch theory. Maher and Thompson (1992) concluded that the loess time series provides a magnetic stratigraphy which is directly related to palaeoclimatic changes, to a finer resolution than simply glacial/interglacial. The data is shown in Figure 1.11.

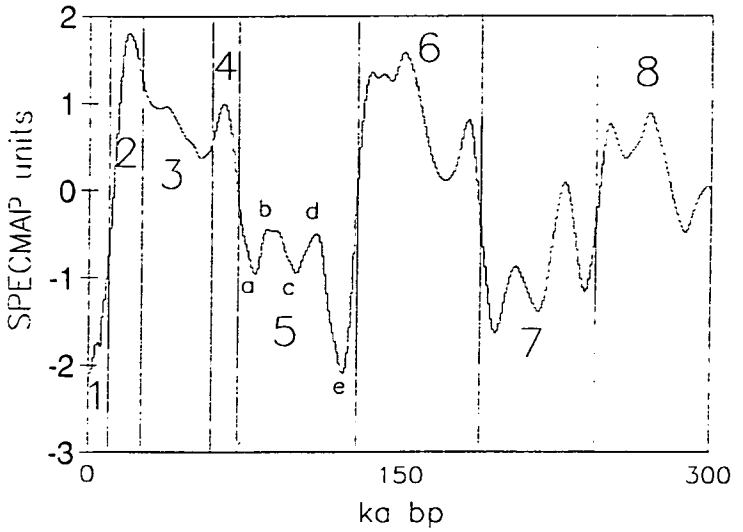

Figure 1.10. The commonly used Oxygen isotope stage numbering. Odd numbered stages are warmer, even stages cooler. Note the subdivision of stage 5 into stages 5a-e.

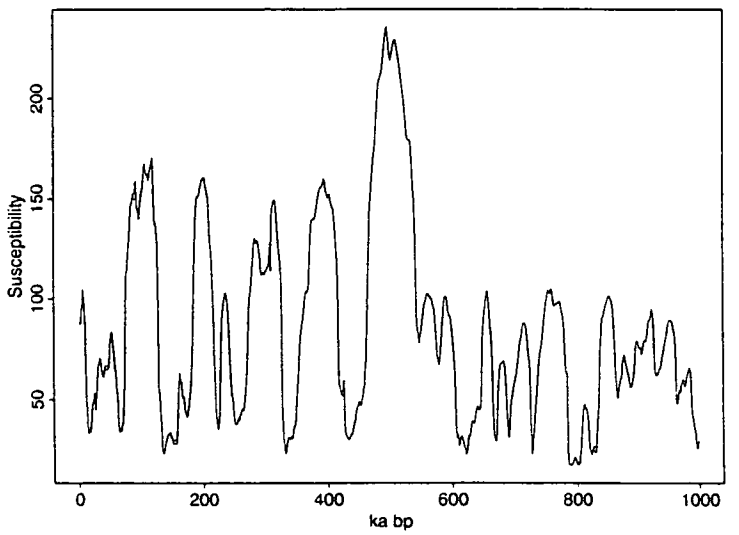

Figure 1.11. The magnetic susceptibility record from the Chinese Loess succession. Periods of high susceptibility correspond with warmer climate. Data is from Kukla et al. (1990).

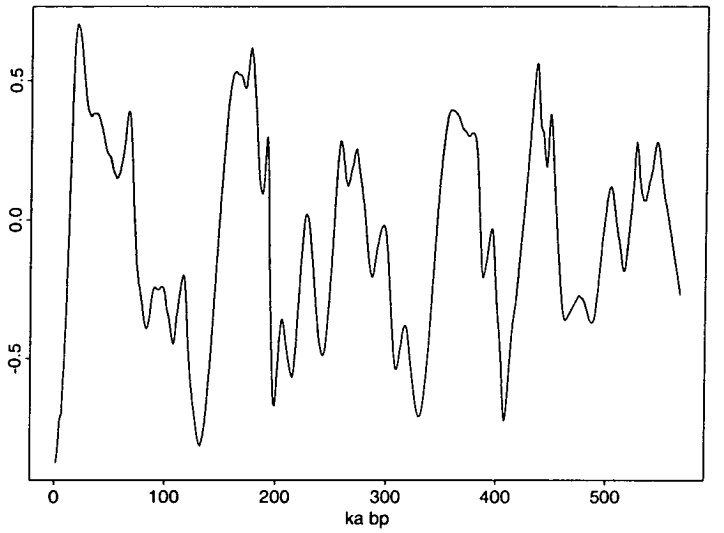

Figure 1.12. The oxygen isotope record from the Devil's Hole calcite vein (Winograd et al. 1992). Note the strong similarity with the SPECMAP record.

1.5.3 Devil's Hole Calcite Vein

The Devil's Hole calcite record is an oxygen isotope record from Nevada, USA (Winograd et al. 1992, Ludwig et al. 1992). The calcite has accumulated on a stalagmite, reaching a length of 23 cm. Analysis of the isotope variations has produced a record covering the last 567 ka. The dating of the record has used the latest radiometric techniques (Section 1.4.2), and is claimed to have a high accuracy level (Ludwig et al. 1992). Winograd et al. (1992) claim that the timings of certain events in the Devil's Hole record, particularly the MIS 5/6 deglaciation, contradict the Milankovitch hypothesis (as the deglaciation occurs before the insolation pulse thought to have precipitated it). However, it is unclear which features of the Devil's Hole record represent local scale variations and which a global signal. Regardless of this, its overall similarity to the marine record is astounding. The data is shown in Figure 1.12.

1.5.4 Lake Cores and Pollen Reconstructions

Pollen Analysis (Palynology) is one of the major sources of terrestrial climate records. Pollen grains and spores are extremely resistant to decay, are produced in vast quantities, and reflect the natural vegetation of an area around the preservation site. Pollen grains can be differentiated by their shape, size, sculpturing

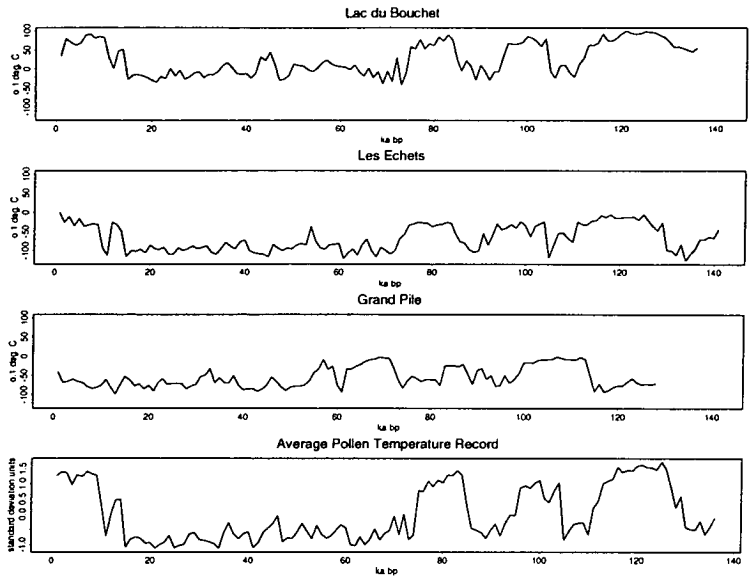

Figure 1.13. The temperature reconstructions, from the analysis of past pollen distributions, for Lac du Bouchet, Les Echets, and Grand Pile (Guiot 1990, de Beaulieu et al. 1991, Guiot et al. 1992). Also shown is an average curve we have constructed to remove regional variations between the records.

etc., leading to identification to plant family, genus, or even species level. The Analogue Method then involves comparison of present day vegetation, and its pollen profiles and climate, with the pollen profiles in the palaeorecord. The resultant transfer function then gives a palaeotemperature estimate by analogue with the modern climate (Guiot 1990).

Proxy inferred temperature data are available from three locations in France, namely Grand Pile, Lac du Bouchet (Plateau du Deves), and Les Echet (Guiot 1990, de Beaulieu et al. 1991, Guiot et al. 1992). Each record covers approximately from the present day back to 140 ka bp, in 1000 year intervals (Figure 1.13). The strength of these records is in their temporal coverage, as continuous terrestrial records of this length are very rare. The data is in 0.1 deg. Celsius anomalies from present day.

1.6 The Climate System

A very brief introduction to the Earth's climate system is provided here. For a fuller description see Henderson-Sellers and Robinson (1986).

The Earth is continually receiving energy from the Sun. A proportion of this is reflected back into space by dust particles, clouds, or the surface of the Earth.

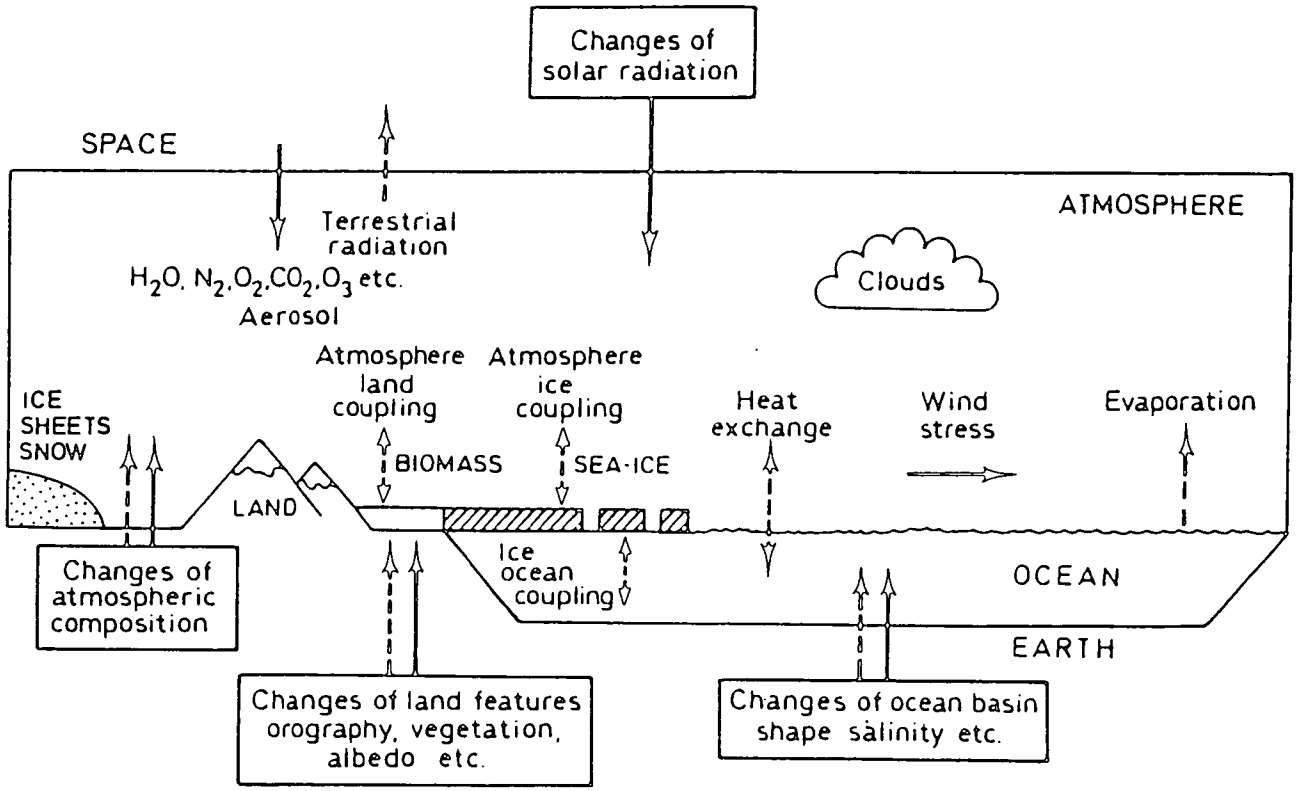

Figure 1.14. A schematic diagram of the various components which constitute the Earth's climate system. Full arrows represent external processes and dashed arrows are examples of internal processes. From Henderson-Sellers and Robinson (1986).

The remaining energy is absorbed by the Earth and is subsequently radiated back towards space. Only at latitudes 40° North and 40° South is the incoming energy and the radiated energy in balance (Imbrie and Imbrie 1979). At all other latitudes the Earth should be warming or cooling. These thermal inequalities are removed by the transportation of energy between the latitudes by processes such as the Trade Winds and the Gulf Stream.

The climate system consists of several major components: hydrosphere, atmosphere, biosphere and cryosphere (ice sheets, glaciers, sea-ice etc.). The relationships between these and other components are described in Figure 1.14. The interactions of these various components are the mechanisms through which the insolation variations are translated into climate changes. In particular, positive feedback processes (such as a reduction in the ice sheet extent producing a drop in albedo and therefore increased warming and further melting of the ice sheets) play a major role in producing many of the climate features, such as deglaciations.

1.7 Spectral Analysis

The technique of Spectral Analysis has been fundamental to the support and analysis behind the Milankovitch theory. We present a short introduction based on the notation of Chatfield (1989). This follows the techniques of Jenkins and Watts (1968) and Priestley (1981). Other statistical techniques will be implemented in this thesis, but these will be introduced when they are required.

1.7.1 The Spectral Density Function

The spectral density function $f(\omega)$, describes the variation in a time series in terms of periodic components at different frequencies. It is also known as the spectrum. It is the derivative of the (assumed differentiable) spectral distribution function $F(\omega)$, which is the contribution to the variance of the time series which is accounted for by the frequencies in the range $(0, \omega)$. Chatfield (1989) shows that the spectrum is the Fourier transform of the autocovariance function $\gamma(k)$. That is

$$f(\omega) = \frac{1}{\pi}\left[\gamma(0) + 2\sum_{k=1}^{\infty}\gamma(k)\cos\omega k\right] \tag{1.2}$$

which can be rewritten

$$f(\omega) = \frac{1}{2\pi}\sum_{k=-\infty}^{\infty}\gamma(k)e^{-i\omega k}. \tag{1.3}$$

1.7.2 The Periodogram

Spectral analysis is a technique for estimating the spectral density function which is suitable for stochastic as well as deterministic functions. This analysis is referred to as analysing a time series in the frequency domain.

Early (19th century) frequency analyses assumed a model of the form

$$X_t = \mu + \alpha\cos\omega t + \beta\sin\omega t + Z_t \tag{1.4}$$

for $t = 1, ..., N$, where Z_t is a white noise process of IID elements and μ, α, and β are to be estimated from the data. This model is linear in these parameters so they can be estimated by least squares.

Fourier analysis is the repeated application of Equation 1.4 at the frequencies $2\pi p/N$ for $p = 1, ..., N/2$. These are known as the Fourier frequencies, and lead

to the finite Fourier series representation of X_t, which is

$$X_t = a_0 + \sum_{p=1}^{(N/2)-1} [a_p \cos(2\pi pt/N) + b_p \sin(2\pi pt/N)] + a_{N/2} \cos \pi t \qquad (1.5)$$

for $t = 1, ..., N$. The coefficients a_p, b_p are the same as the α and β in equation 1.4, for each value of p.

Fourier analysis decomposes the variance of the time series into components at frequencies $\omega_p = 2\pi p/N$, referred to as the p^{th} harmonic. The p^{th} harmonic is equal to

$$a_p \cos \omega_p t + b_p \sin \omega_p t \qquad (1.6)$$

and this can be rewritten as

$$R_p \cos(\omega_p t + \phi_p) \qquad (1.7)$$

where

$$R_p = \sqrt{(a_p^2 + b_p^2)} \qquad (1.8)$$

is the amplitude of the p^{th} harmonic, and

$$\phi_p = \tan^{-1}(-b_p/a_p) \qquad (1.9)$$

is the phase of the p^{th} harmonic.

It can be shown that

$$\sum (x_t - \bar{x})^2/N = \sum_{p=1}^{(N/2)-1} R_p^2/2 + a_{N/2}^2, \qquad (1.10)$$

and this is known as Parseval's theorem. The left hand side is approximately the variance of the data (divisor is N rather than $N - 1$), so that $R_p^2/2$ is the contribution of the p-th harmonic to the data variance. That is, $R_p^2/2$ is the contribution to the variance at the frequency ω_p. A line plot of $R_p^2/2$ against $\omega_p = 2\pi p/N$ gives a line spectrum. However, if we regard $R_p^2/2$ as the contribution to the total variance from frequencies in $\omega_p \pm \pi/N$ then we could plot a histogram with rectangles of area $R_p^2/2$. We then have

$$I(\omega_p) = N R_p^2/4\pi. \qquad (1.11)$$

A plot of $I(\omega)$ against ω is called the periodogram. Calculation of $I(\omega)$ from the data is achieved by

$$I(\omega_p) = [(\sum x_t \cos 2\pi pt/N)^2 + (\sum x_t \sin 2\pi pt/N)^2]/N\pi. \tag{1.12}$$

It can also be shown that the periodogram and the autocovariance coefficient $c_k = \sum_{t=1}^{N-k}(x_t - \bar{x})(x_{t+k} - \bar{x})/N$ are related via

$$I(\omega_p) = (c_0 + 2\sum_{k=1}^{N-1} c_k \cos \omega_p k)/\pi \tag{1.13}$$

or

$$I(\omega_p) = \sum_{k=-(N-1)}^{N-1} c_k e^{-i\omega_p k}/\pi, \tag{1.14}$$

i.e. the periodogram is the finite Fourier transform of c_k. When expressed in this form it appears that equation 1.14 is the obvious estimate of the power spectrum shown in equation 1.3, with the $\gamma(k)$ replaced by their estimates $c(k)$. However, whilst $E[I(\omega)] \to f(\omega)$ as $N \to \infty$ the variance is $Var[I(\omega_p)] = \sigma^4/\pi^2$. This is constant, and does not tend to zero as $N \to \infty$. We say that $I(\omega)$ is not a consistent estimator for $f(\omega)$.

This problem is overcome by essentially smoothing the periodogram. We describe two possible techniques for achieving this.

Weighting the autocovariance function It is clear that the precision of the c_k will decrease as k increases, so we weight the c_k to have less weight as k increases, and to have zero weight above a truncation point $M(< N)$. Our new estimator is

$$\hat{f}(\omega) = \frac{1}{\pi}\left[\lambda_0 c_0 + 2\sum_{k=1}^{\infty} \lambda_k c_k \cos \omega k\right]. \tag{1.15}$$

The λ_k are known as the lag window. A variety of lag windows exist e.g. Tukey, Parzen, or slightly more complex variations e.g. Hanning, Hamming. See Chatfield (1989), Diggle (1990) for further details.

Smoothing the Periodogram An alternative to lag windows is simply to smooth the periodogram directly via

$$\hat{f}(\omega) = \frac{1}{m}\sum_j I(\omega_j). \tag{1.16}$$

It can be shown (Chatfield 1989, Diggle 1990) that these two techniques are very similar. The lag window technique was preferred in the past as it was computationally less intensive, but the growth in computer power and the advent of the fast Fourier transform have led to increased use of the smoothed periodogram.

The main assumption in this type of analysis is that the periodic variations are sinusoidal in nature and are constant throughout the period of interest. For palaeoclimatic data this is generally incorrect, but spectral analysis can still be extremely useful at indicating the periodicities present in a time series.

1.8 Aims

In the above sections we have described the variations in the Earth's orbit, the behaviour of past climate and its reproduction through geological techniques, and introduced the concept of orbital and insolation changes forcing the climate. All these datasets are in time series form.

The aim of this thesis is to analyse this input-output system via a selection of statistical techniques. We assess the benefits and limitations of previously applied techniques. We then go on to introduce several new methods, describe their application, interpret the results, discuss the geological implications, and summarise their benefit and applicability to palaeoclimate analysis.

1.9 A Plan of the Thesis

By considering the Earth's climate as an input-output system there are numerous statistical techniques which can be used to analyse it. Chapter 2 presents a review of past applications of statistical techniques to palaeoclimatic data analysis, including an introduction to the different spectral analysis techniques used.

Spectral analysis has been the foundation on which the Milankovitch theory proof has been based, but the inherent assumptions (that the frequencies present, and their amplitudes, are constant) leads to a loss of information in the analysis. In Chapter 3 we apply the technique of Complex Demodulation. Complex Demodulation yields quantitative estimates of the amplitude and phase variations of the periodicities in the time series. The results of this chapter confirm the orbital forcing of climate, and support the assumptions which allow us to apply the regression models in the subsequent chapters.

In order to understand the limitiations of linear models, in Chapter 4 we

apply some simple regression models to various palaeoclimatic records. These again highlight the obvious connection between the input and output. It also is important to appreciate the limitations of such models, although we show that they have benificial applications in essentially rescaling existing time series.

Having displayed the inability of simple, linear models to reproduce past climate change, Chapters 5 and 6 attempt to overcome these limitations.

It is clear that the Earth's climate system contains many thresholds e.g. collapsing of the ice sheets at some critical size, and we wish to explore for thresholds in the Earth's response to orbital and insolation variations. In Chapter 5 we investigate two nonlinear regression techniques which include a response variable transformation and univariate regressors. These allow us to visualise (in 2D) the relationship between each orbital variable and palaeoclimate.

Having explored the nonlinear effect of each input variable individually, in Chapter 6 we apply further nonlinear techniques which allow the visualisation of the interactions between the orbital and insolation variations.

These two chapters yield important conclusions about the forcing of particular events and the role of each orbital variable in climate change.

We then go on, in the final chapter, to bring together our conclusions about the forcing of the Earth's 100 ka ice age cycle, to discuss the statistical/methodological conclusions, and the implications for particular palaeoclimatic time series.

Chapter 2

Review and Critique of Time Series Analysis Techniques in Palaeoclimatology

"Harvey Sachs suggested the use of time series analysis"

Imbrie and Kipp, 1971

2.1 Introduction

As illustrated in Chapter 1, there is now very strong evidence for modulation of climate by the Earth's fluctuating orbital geometry. The "proof" of this theory has depended heavily on time series analysis (TSA), particularly the frequency domain technique of spectral analysis. With the accurate calculation of the orbital configuration for both past and future (Berger and Loutre 1991) we also have available the necessary input data to investigate the Earth's climate dynamics through statistical modelling.

In this chapter we summarise the previous applications of statistical TSA techniques, and assess their benefits and limitations. One event stands out in the field: the work of Hays et al. (1976) is generally regarded as the first paper to combine high quality palaeoclimate information, of a suitable timescale, with quantitative statistical analysis. We therefore summarise the attempts at statistical analysis prior to 1976, and then investigate the particular areas of analysis that have followed on from this time.

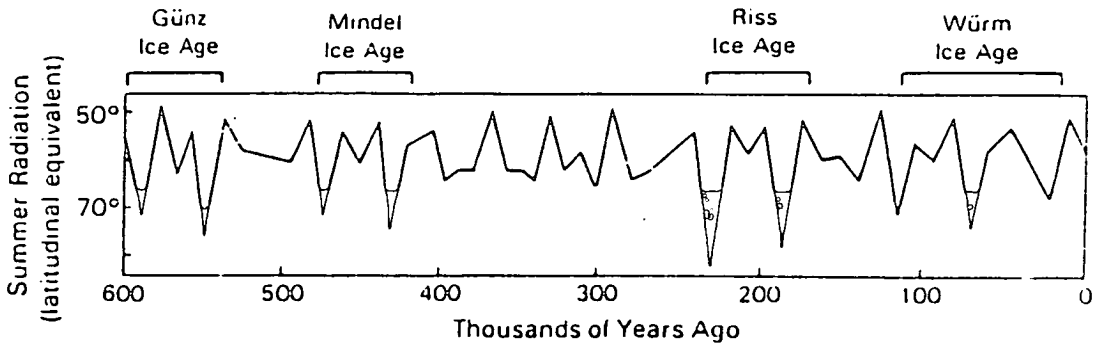

Figure 2.1. The original Milankovitch radiation curve for $65°N$, based on the understanding of the orbital variations at that time. The shaded regions represent periods of low insolation, which Milankovitch identified as corresponding with four European ice ages. The variations in radiation intensity are expressed as latitudinal equivalents. This data was originally published in 1924, although this graph is from Milankovitch (1936).

All this work must be analysed in the context of the data. Palaeoclimatic time series are inexact estimates with respect to both the data values and the timings prescribed to them (see Chapter 1). Many also exhibit awkward statistical properties, e.g. nonstationarity, which break the assumptions made in constructing standard techniques. Therefore, in many cases the application of a particular technique to a particular time series is contrary to the theoretical assumptions. However, through careful and conservative conclusions, all analyses can add some understanding to the wider picture.

2.2 Pre-1976

The ideas behind orbital forcing of the Earth's ice age succession date back to the mid-nineteenth century (Adhemar 1842), but it was impossible to make any positive steps without an accurate chronology for the ice ages and past insolation variations.

The scientific growth of the astronomical theory has been described in Section 1.2. If the first step in time series analysis is to plot the data, then Milankovitch's calculation of the radiation curve for latitude $65°N$ and its visual comparison with the geological data available at that time (Koppen and Wegener 1924) represents the first "statistical" analysis of palaeoclimate (Figure 2.1).

Visual comparison continued up to the early 1960's when the Milankovitch

theory lost favour, due to newly available radiocarbon age estimates of glacial periods (e.g. Goldthwait et al. (1965)). However, other radiometric techniques soon became available, and Broecker et al. (1968) and Mesolella et al. (1969) renewed interest in the orbital theory due to dating of three Barbados coral terraces corresponding with northern hemisphere insolation highs (125, 105 and 82 ka bp). By this time the first example of spectral analysis applied to a palaeoclimatic time series had been produced (van den Heuvel 1966).

Fourier analysis was used by van den Heuvel to investigate the periodicities present in Emiliani's early oxygen isotope data (0-300 ka). Fourier analysis finds the exact periodicities in a curve if the oscillations are sinusoidal in character. Obviously this is not the situation here, but van den Heuvel argues that it is possible to roughly draw a sinusoid of length 40 ka through the data. He first calculated the summations

$$a_n = \sum_{0}^{\lfloor n \rfloor P} T(t)\cos(n\pi t/300000)/300000 \tag{2.1}$$

and

$$b_n = \sum_{0}^{\lfloor n \rfloor P} T(t)\sin(n\pi t/300000)/300000 \tag{2.2}$$

where $T(t)$ is temperature (as a function of time, t), P is the period of interest, $n = 300000/P$ is the number of oscillations with this period in the time series, and $\lfloor n \rfloor$ denotes the largest integer smaller than n. Then

$$R_n = \sqrt{(a_n^2 + b_n^2)} \tag{2.3}$$

is an estimate of the amplitude of the periodicity of wavelength P in T(t). The noise level was estimated as the mean level of the small peaks in the spectrum. Then the probabilities of peaks in the Fourier spectrum being due to noise were calculated according to Whittaker and Robinson (1932) via

$$P(k) = \frac{1}{\sqrt{\pi}} e^{-k^2}, \tag{2.4}$$

where k is the ratio of the peak height to the noise level. The three most significant periods identified are 42857, 39474 and 12825 years. The first two were related to the obliquity cycle (quasi-period of 41 ka), and the higher frequency was explained

as being approximately half of the precession quasi-periodicity (11615 years).

Kemp and Eger (1967) used the spectral techniques of Evans et al. (1965). They applied power spectrum analysis to the data on a depth scale, and then compared the power spectrum density with that for summer insolation variations at $65°N$. They assigned different ages to the bottom of their core until the peaks in the two power spectra visually matched. This gave an age for the core bottom of 360 ka bp, and an estimated (constant) sedimentation rate for the core. This can be seen as an early precursor to the "tuning" techniques now used to date palaeoclimate records. Also, Kemp and Eger (1967) were the first to speculate that the geologic record could aid in the development of more accurate estimates of the long term planetary motion.

In 1971 the ecological methods of core interpretation were much improved by Imbrie and Kipp (1971), using a statistical factor analysis. They were also the first to apply the power spectrum techniques of Blackman and Tukey (1958), a practise which was to become the standard throughout the next quarter century. Imbrie and Kipp used the hamming technique to smooth the Fourier transform of the autocorrelation function. They find some evidence for a 98 ka period, but no spectral peaks at the obliquity and precession frequencies, although this may partly be due to the location of the core (Caribbean). They also discuss the limitations of their constant sedimentation assumption, and analyse a synthetic data set with variable "sedimentation" and noise to indicate the potential distorting effect on the spectrum.

The first attempt at modelling the ice age variations as a function of insolation variations was by Calder (1974), who investigated the "Arithmetic of the ice ages". Calder took the summer insolation at $50°N$, assigned an arbitrary threshold of 17 langley per day (1 Langley = 1 calorie per cm^2) above the 1950 value of 847, and assumed that for values below this there was ice accumulation, and ice melting for higher values. A melting rate of unity and a freezing rate of 0.22 gave a realistic curve for the last 78 ka. This method is exceptionally simple, but still reproduced many features of past climate and indicated the potential of this type of input/output modelling.

2.3 Pacemaker of the Ice Ages

Hays et al. (1976) produced a continuous, statistically useful record of length 450 ka, and with a sedimentation rate high enough to resolve periods of well below

20 ka.

They made the assumption that the Earth is a time invariant, linear system, so that its response in the frequency domain is well understood: frequencies in the output will match those in the input, but with their amplitudes modulated by a series of gain functions (Jenkins and Watts 1968) . In an attempt to minimise the problem of chronology, in addition to looking for the obliquity and precession periods in their spectrum they looked also at the ratio of the two appropriate peaks, expected to be approximately $1.8(\approx 41/23)$.

The spectral theory of Blackman and Tukey (1958) was used, with some elaborations from Jenkins and Watts (1968). These techniques are the "classical" spectral techniques, and will be discussed in more detail in Section 2.5. The methodology of Hays et al. (1976) included detrending, prewhitening and smoothing with a Hamming lag window. Their sampling interval was 3000 years. As support for the existence of the spectral peaks which they had found an analysis using the Maximum Entropy Method (MEM), an alternative spectral technique (section 2.6.1), was also carried out, and this is claimed to have supported the conclusions, although no results are given.

To evaluate the significance of each peak Hays *et al* calculated a low resolution spectrum by initially prewhitening with a first difference filter. This gives a spectrum of similar overall shape but a lot smoother. Then a particular peak is judged significant if it extends above the low resolution spectrum by more than the appropriate one sided confidence interval (from discussions with Tukey).

Hays *et al* additionally used a Tukey bandpass filter to analyse each frequency component in the data. This removes the component in the data in a particular frequency range. Bandpass filtering has been a key technique in the confirmation of the Milankovitch theory, through the comparison of the input and output behaviour, and also in the exploitation of the tuning technique to date the palaeoclimatic time series (Section 1.4.4)

Spectral analysis revealed three main periodicities, namely 23, 42, and 100 ka, when the time series was dated using an extremely simple constant accumulation rate model. These frequencies closely match the Milankovitch frequencies. In addition, the bandpass filter analysis showed that all these frequencies are approximately in phase with the corresponding orbital variations. These phase analyses were then used to "tune" the data (the TUNE-UP timescale) to give superior phase results. This resulted in slight modification of the radiometrically calculated tie-points, but only within the error of the estimates.

Hays *et al* go on to conclude that changes in the Earth's orbital geometry are the fundamental causes of Quaternary climate changes, and therefore act as the "Pacemaker of the Ice Ages".

The main failure of Hays et al. (1976) is their inability to account for the 100 ka ice age cycle. They observe that this dominant periodicity occurs also in eccentricity variations, and that glaciations occur during periods of low eccentricity. However, they admit that whilst precession and obliquity have a linear effect on climate, an assumption of nonlinearity would be required for the 100 ka cycle to result from eccentricity variations. This may be through direct amplification of eccentricity forced insolation changes, eccentricity's modulation of the precession effect, or possibly inequalities in the growth/decay rates of the ice sheets.

Hays *et al* finally conclude that, excluding anthropogenic efects, the long term trend is for the climate to be cooling over the next 20 ka.

The techniques and general analytical viewpoint of this paper are still in extensive use today.

2.4 Post-1976

Since 1976, a large quantity of literature has appeared concerning the application of statistical techniques to palaeoclimatic data. We divide it into the following groups:

- Commonly used Spectral Analysis techniques;
- Other Spectral Analysis techniques;
- Modelling techniques.

We begin by describing the spectral techniques which are most commonly utilised to describe palaeoclimatic data, and then look at less prevalent (and generally more modern) frequency-domain analysis techniques. We then summarise statistical attempts to characterise the relationship between the orbital/ insolation inputs and climate.

2.5 Common Spectral Analysis Applications

Since Imbrie and Kipp (1971), the analysis of palaeoclimatic time series has lent heavily on the work of Blackman and Tukey (1958) and subsequent expansions

by Jenkins and Watts (1968). Some examples of such usage are in Hays et al. (1976), Imbrie et al. (1984), Shackleton et al. (1990), Imbrie et al. (1992), Imbrie et al. (1993). The main techniques used are Fourier spectral analysis, cross-spectral analysis, and band-pass filtering. These have been fundamental in the formulation of our understanding of long term climate change. An introduction to these techniques has been given in section 1.7.

Jenkins and Watts define the sample spectrum of X_t as

$$c_{xx}(\omega) = \frac{\Delta}{N}\{(\sum_{t=-n}^{n-1} x_t \cos 2\pi\omega t\Delta)^2 + (\sum_{t=-n}^{n-1} x_t \sin 2\pi\omega t\Delta)^2\} \tag{2.5}$$

where Δ is the time interval between samples.

The cross-spectrum is defined as (from Chatfield (1989))

$$f_{xy}(\omega) = \frac{1}{\pi}\left[\sum_{k=-\infty}^{\infty} \gamma_{xy}(k)e^{-i\omega k}\right]. \tag{2.6}$$

Thus it can be viewed as the natural extension of the cross-correlation function into the frequency domain, and is the Fourier transform of the cross-covariance function ($\gamma_{xy}(k)$), over the range $0 < \omega < \pi$.

This is complex valued, as $\gamma_{xy}(k)$ is not an even function. Therefore, let us define

$$f_{xy}(\omega) = c(\omega) - iq(\omega), \tag{2.7}$$

which can alternatively be written as

$$f_{xy}(\omega) = \alpha_{xy}(\omega)e^{i\phi_{xy}(\omega)} \tag{2.8}$$

for appropriate α and ϕ.

We then have that the (squared) coherency is

$$C(\omega) = \frac{[c^2(\omega) + q^2(\omega)]}{[f_x(\omega)f_y(\omega)]} = \frac{\alpha_{xy}^2(\omega)}{f_x(\omega)f_y(\omega)} \tag{2.9}$$

where $f_x(\omega), f_y(\omega)$ are the power spectra of X_t and Y_t.

It can be shown that $0 \leq C(\omega) \leq 1$, and the closer $C(\omega)$ is to unity, the more closely related are the two time series at frequency ω. In addition, the phase spectrum is defined as

$$\phi_{xy}(\omega) = \tan^{-1}[-q(\omega)/c(\omega)]. \tag{2.10}$$

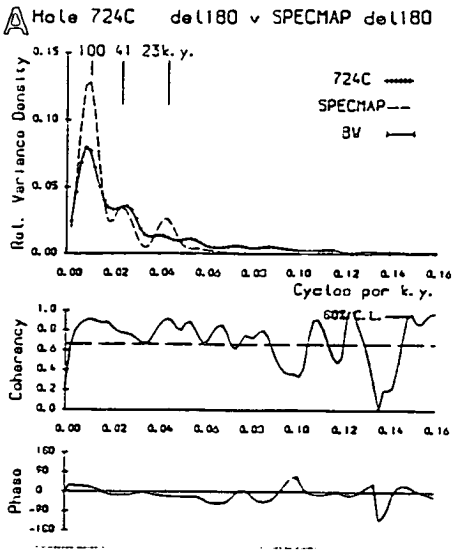

Figure 2.2. An example of Jenkins and Watts analysis, from Weedon and Shimmield (1991). The top shows the power spectrum of two time series (the oxygen isotope record of ODP core 724, and the SPECMAP oxygen isotope record). Middle plot is of the coherency, and the bottom plot is the phase spectrum estimate.

To illustrate the application of these techniques, Figure 2.2 shows a typical analysis between two climatic time series. The figure is from Weedon and Shimmield (1991) and is a comparison of the oxygen isotope record from ODP core 724 with the SPECMAP oxygen isotope record. There is the variance spectrum of each series, with some evidence for corresponding Milankovitch frequencies. Below this is the coherency, with the 80% confidence level shown. We observe that there is strong evidence for coherency over all the frequency range of interest. The bottom plot shows the corresponding phase estimate for all ω, although this is only relevant for values of ω where the coherency is statistically significant, and the phase information is very difficult to interpret so is not often used. Similar plots comparing orbital (or insolation) time series with palaeoclimatic records can provide support for the Milankovitch theory (through the variance spectrum and the coherency) and estimate the phase leads/lags between these time series.

Whilst these methods are still in extensive use they are of lower resolution than other methods now available (see section 2.6.2). However, Imbrie et al. (1992) consider the lower resolution work of Jenkins and Watts (1968) to be a useful buffer against the uncertainties in the dating of palaeoclimatic records. In addition, the spectral power at any frequency is proportional to the squared

amplitude of that oscillation. This means that periodogram analysis is poor at indicating periodicities of low amplitude, a problem bypassed by the Multi Taper Method (Yiou et al. 1991).

Following on from Hays et al. (1976), Moore et al. (1977) were the first to use the cross-spectral techniques of Jenkins and Watts (1968) to compare several climatic indicators. They additionally calculated the correlation coefficients between the time series to estimate any leads and lags. The cross-spectral analysis produced coherency peaks at approximately the obliquity and precession frequencies. Both periods also suggested that oxygen isotope changes preceeded carbonate changes by about 10000 years.

The work of Pisias et al. (1973) and Moore et al. (1977) was continued in Kominz et al. (1979), with the aim of using the orbital data to extend the geological time scale produced in Hays et al. (1976) back to the Brunhes-Matuyama magnetic boundary. They used the technique of Complex Demodulation (Bloomfield 1976, and chapter 4) to determine the phase of the $\delta^{18}O$ record and obliquity, and the phase lag (approximately 10000 years) between the two records kept constant. Cross spectral analysis and band pass filtering showed that the orbital and isotope records were significantly coherent at both the obliquity and precession (41,23 and 19 ka) frequencies. This new (TWEAQ) timescale gave the age of the Brunhes Matuyama boundary as 728 ka bp, an estimate that was to stand until 1990.

In Imbrie et al. (1984) (which produced the SPECMAP time series) the changes in both obliquity and precession were used to develop a new time scale. Using their resultant time scale, isotopic variations were phase locked ($\pm 15°$) and strongly coherent (> 0.9) not only at 19,23 and 41 ka, but also at the 100 ka periodicity. They assumed that the climate is a time invariant, single-exponential system, so that rate of response at any instant is proportional to the magnitude of the forcing. Once again, bandpass filters were used to extract frequency components, and match these curves to the phase shifted orbital curves. The time scale was developed by using a number of control points (around 70) and an iterative approach, adjusting 1 or more control points at each iteration. The SPECMAP record was then the stacked, smoothed combination of the 5 cores. Each core was normalised to zero mean and unit variance, interpolated to units of 1 ka, the curves were averaged and then smoothed with a 9-point Gaussian filter.

The resultant climate variations and time scale have become benchmarks in palaeoclimate analysis.

The methods employed in Imbrie et al. (1984) are still in prevalent use today, and have produced many important results. For example, Shackleton et al. (1990) used the usual Jenkins and Watts techniques, but with a higher resolution core, and were able, using tuning, to modify the radiometric dates for the Brunhes Matuyama boundary and earlier magnetic reversals, leading to ages that were $5 - 7\%$ older than previously thought.

2.6 Further Spectral Analysis techniques

Whilst most spectral analysis of palaeoclimatic records has focussed on the Fourier technique of Blackman and Tukey (1958) and Jenkins and Watts (1968), this method has certain disadvantages. The main ones are its low frequency resolution and the interdependence between amplitude and significance. As a result of this, a variety of other spectral analysis methods have been employed. Here we describe the two most prevalent, and their apparent advantages/disadvantages in comaprison with standard Fourier techniques.

2.6.1 Maximum Entropy Method

The Maximum Entropy Method (MEM) (Burg (1972), also referred to as Maximum Entropy Spectral Analysis, MESA) assumes that the time series can be estimated well by an AR process of some order M. If the time interval between observations is Δ, then, from Penland et al. (1991) we have that

$$x(t + M\Delta) = \sum_{k=1}^{M} a_k x[t + (M - k)\Delta] + \xi \tag{2.11}$$

where ξ is a white noise process. Then the Fourier spectral density of such an AR process is

$$P(\omega) = \frac{a_0}{\left|1 + \sum_{k=1}^{M} a_k e^{2\pi i k \omega \Delta}\right|^2} \tag{2.12}$$

The user then has to choose a suitable value of M. If M is too small then the spectral resolution will be too low to resolve close frequencies. If M is too large then spurious peaks will be introduced to the spectrum making correct diagnosis more difficult. This is a particular problem when the signal to noise ratio in the data is low.

Therefore, the MEM can be seen as a less conservative technique than Jenkins

et al, and it is recommended that it be used in conjunction with a lower resolution technique (Berger, Melice and Hinnov 1991).

Figure 2.3 is an example of the application of the MEM to a noisy time series.

2.6.2 Thomson's Multi Taper Spectral Method

The Multi Taper Method (MTM) (Thomson 1982, Thomson 1990b) is a high resolution spectral technique. It provides a statistical F-test for the validity of the location of each peak in the spectrum, and its amplitude. It therefore can detect low amplitude oscillations with a high degree of confidence. From the theoretical standpoint, this is an improvement on the standard Blackman-Tukey/ Jenkins and Watts techniques where the statistical significance of a peak is highly correlated with its amplitude (Berger, Melice and Hinnov 1991). The use of Thomson's MTM has grown recently e.g. Yiou et al. (1991), although for reasons outlined in Section 2.5 the theory of Jenkins and Watts is still more prevalent. However, the higher resolution available with the MTM has been exploited in Yiou et al. (1991), where they apply it to the Vostok ice core record for the last 160 ka. This core is inherently more suitable for high-resolution analysis as the data is at 100 year time intervals, whereas ocean sediment cores usually only yield data at 500-3000 year intervals. Table 2.6.2 shows the statistically significant frequencies obtained. The 133 ka period has no significance in a record of this length. However, they then find the expected obliquity (41.6 ka) and precession (24.1 and 18.3 ka) frequencies. They additionally find a large number of higher frequency oscillations which they describe as being combination tones of the three orbital frequencies. This would imply that the Milankovitch theory has an effect down to timescales of 2000 years.

MTM Theory

Assume that X_t is a sinusoidal signal of frequency $\hat{\omega}$ such that

$$x(t) = \mu e^{i\hat{\omega}t} \tag{2.13}$$

for $t = 0, ..., N-1$, and let W_t be a taper of length N. Then the discrete Fourier transform of the tapered signal $X \cdot W$ is

$$y(\omega) = \sum_{t=0}^{N-1} x(t)w(t)e^{-i\omega t} \tag{2.14}$$

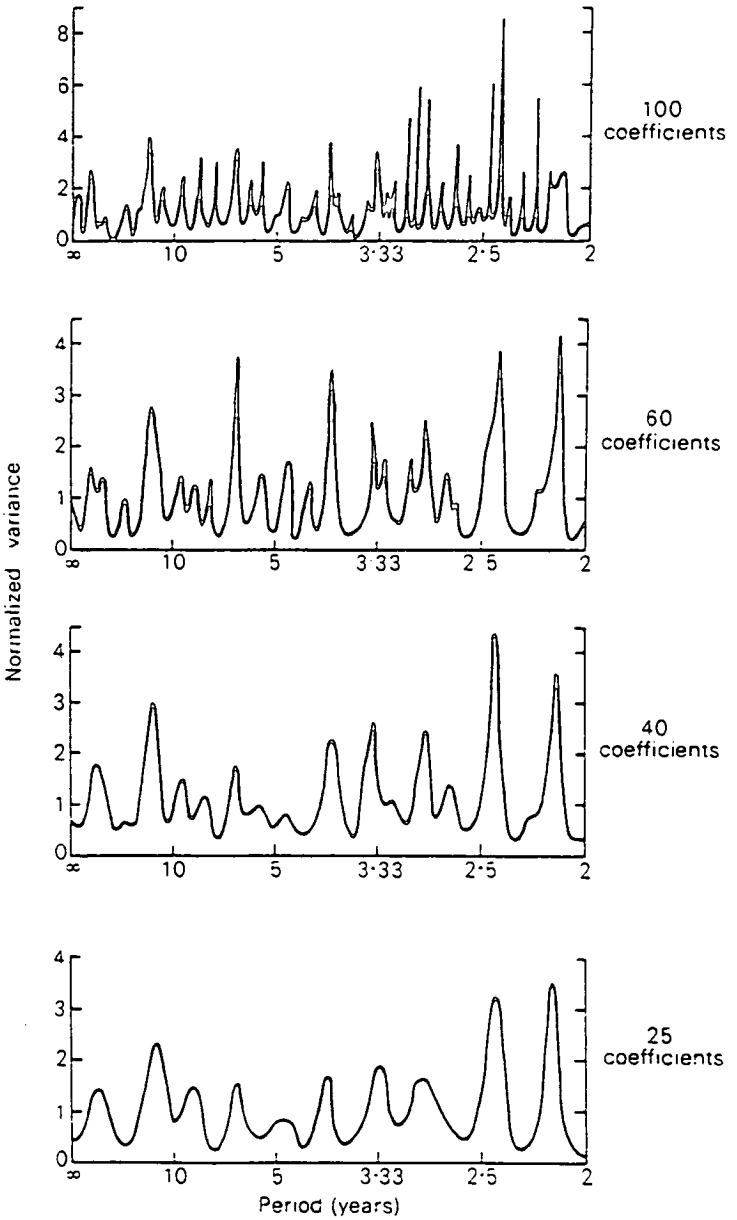

Figure 2.3. The repeated application of the MEM to the rainfall record from Kew, England, for the period 1697 to 1975. This is an example of how, as M increases, the resolution of the peaks increases, but the number of spurious peaks increases greatly. Original figure is from Tabony (1979)

Period (ka)	Significance (%)	Combination Tone	Order of Combination
133	1		
41.6	3	f_3	1
24.1	6	f_2	1
18.3	10	f_1	1
16.0	7	$2f_2 - f_3$	3
14.1	7	$f_2 + f_3$	2
11.1	1	$2f_2$	2
7.35	6	$2f_2 + 2f_3$	4
6.57	10		
5.43	7	$f_1 + 3f_2$	4
4.90	6	$3f_2 + 3f_3$	6
4.35	3	$3f_1 + 3f_3$	6
3.82	9	$5f_1$	5
3.65	2	$3f_1 + f_2 + 3f_3$	7
3.47	1	$3f_1 + 3f_2$	6
3.36	3	$4f_1 + 2f_2$	6
2.45	1		
2.38	6	$8f_1$	8

Table 2.1. The significant (at 10%) spectral peaks in the MTM analysis of the Vostok ice core. The peaks labelled f_1, f_2, f_3 represent the obliquity and two precession frequencies. Combination tones are then possible explanations of the higher frequencies as harmonic combinations of the main Milankovitch frequencies. This implies that the Milankovitch variations can effect climate down to a timescale of only several thousand years. From Yiou et al. (1991).

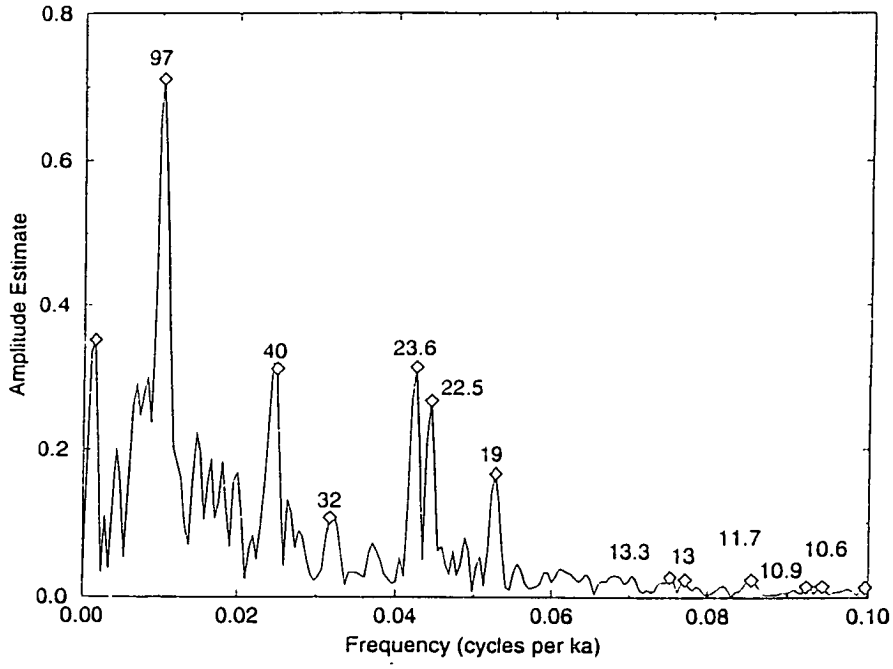

Figure 2.4. The multi-taper spectrum of the SPECMAP time series. Black diamonds represent frequencies that are detected as being significant at the 10% level. Comparison of this figure with the Blacman-Tukey equivalent in Figure 1.2 shows that we once again pick out the Milankovitch frequencies. However, we also have a significant peak at 32 ka, and this is possibly a secondary peak of obliquity (Mommersteeg et al. 1995). In addition, there are numerous higher frequency peaks which are statistically significant, and these may relate to the 14.1 and 11.1 ka periodicities in the Vostok analysis. This figure produced by the Spectra (Dettinger et al. 1995) software package.

where $\omega = k/N$, for k=0,...,P-1.

The principal behind the MTM is to chose the optimal tapers for any given time series to minimise the spectral leakage. See Yiou et al. (1991) or Berger, Melice and Hinnov (1991) for summary descriptions of the technique, or Thomson (1990b) for a full description.

MTM Example

Figure 2.4 is the output of a MTM analysis of the SPECMAP record, and we have chosen to highlight those frequencies which are significant at the 10% level. The results are very similar to those in Figure 1.2, but with the addition of a peak at 32 ka, and several higher frequencies.

The MTM technique is now becoming prevalent in the palaeoclimate literature, although its application is still best combined with the Blackman-Tukey

technique to ensure robustness.

2.7 Modelling

As explained in Section 2.2, Calder was the first to model long term climate changes as a function of the insolation input. Petersen and Larsen (1978) ignored the Milankovitch theory, and attempted to identify an Autoregresive Integrated Moving Average (ARIMA) model (Box and Jenkins 1976) that described past climate changes. This will be a stochastic model, with no inputs other than past values of the time series and noise estimates. The dominant period in the data used (length 700 ka, sampling interval 5000 years) was 90 ka, so an attempt to remove this was made by seasonally differencing the data using the ∇_{18} differencing operator, where

$$\nabla_{18} = (1 - B)^{18} \tag{2.15}$$

and B is the backshift operator. The final model chosen was the following ARIMA(5,18,18) model:

$$(1 - 1.69B + 1.28B^2 - 0.5B^3 - 0.02B^4 + 0.09B^5)\nabla_{18}x_t = (1 - 0.74B^{18})a_t. \tag{2.16}$$

This type of model is very restrictive as it only accounts for one period in the data, in this case the 90 ka period that was associated with the eccentricity variations. Several future predictions were made, and all signify a cooling over the next 5000 years. This agrees with many orbitally forced models, but subsequent behaviour seems overly restrained by the model chosen.

The method behind Imbrie and Imbrie (1980) can be viewed as an extension of Calder's work. They developed a time dependent differential model of the form

$$\frac{dy}{dx} = f(x, y) \tag{2.17}$$

where y is a measure of the climate state (taken to be total volume of land ice), x the orbital input, and f the system function. The input x is a function of the orbital parameters with two free parameters. The system function f is constructed to account for the tendency of ice sheets to diminish faster than they accumulate, leading to

$$\frac{dy}{dx} = \frac{1}{T_i}(x - y) \tag{2.18}$$

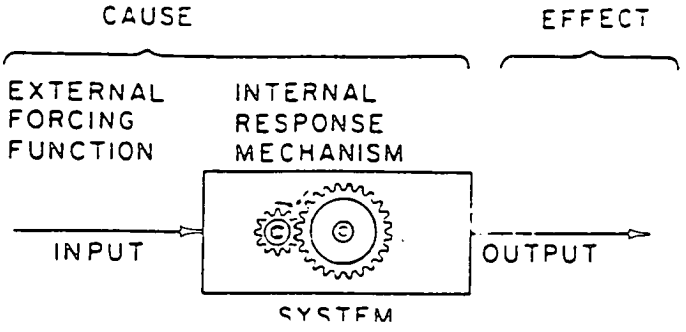

Figure 2.5. A schematic of a simple linear system. The input is in the form of orbital (or insolation) variations, and the output is a time series describing climatic variations. From Imbrie (1985)

where (dy/dt) is inversely proportional to a time constant which takes one of two values depending on whether the climate is warming (T_w) or cooling (T_c). Calibrating the model to the data from Hays et al. (1976) gives $T_w = 10600$ years, $T_c = 42500$ years, and x corresponding to the insolation curve for July at $65°N$. The model reproduces the features of the past 150 ka well, although it fails to capture the full scale of the ice melting corresponding to the last deglaciation (Figure 2.6).

With a large body of work, signifying coincident spectral peaks and high coherency between orbital and climatic spectra (Section 2.5) Imbrie (1985) took the next step of transforming these results into the time domain by using a gain-and-phase model (Figure 2.5). Once again the theory is from Jenkins and Watts (1968). The final model has terms at 123, 95, 59, 41, 23, and 19, each orbital curve multiplied by a suitable gain and shifted by an appropriate phase . The model appeared to change at 400 ka bp, so they looked at 782-400 ka bp and 400-0 ka bp.

1981 saw two papers on modelling. Kukla et al. (1981) produced an Astronomical Climate Index (ACLIN), and created a proxy climate indicator by combining pollen data, sea level estimates, and a $\delta^{18}O$ record. The ACLIN index is based on their assumption that relatively warm climate coincides with high obliquity, high eccentricity, and autumn perihelion. This lead to the following empirical formula for the climate index α:

$$\alpha = \left|\frac{\omega - 180}{90}\right| + \epsilon - 22 + \frac{10^3 e^2}{2} \tag{2.19}$$

where ω is the longitude of the perihelion, e is the eccentricity, and ϵ is the obliquity lagged 5-6000 years. This time lag is chosen due to the orbital configuration at the start of interglacials.

Also in that year, Berger et al. (1981) produced an autoregressive model with six monthly insolation terms, and a seventh term which is the climate of 3000 years before, to take into account the persistence of the system. The final model was (in standardised variables)

$$\begin{aligned} \delta^{18}O(t) &= 0.924\delta^{18}O(t-3) + 0.148J_{85} - 0.11D_{65} + 0.04M_{25} \\ &\quad +0.032S_{-15} - 0.036J_{-55} - 0.034D_{-75} \end{aligned} \tag{2.20}$$

where J represents June, D December, S September, M March, and the subscript is latitude (in degrees North).

Figure 2.6 shows a selection of time series model predictions for the next ice age cycle. There is a broad similarity in the behaviour, with a general cooling trend to a glacial maximum at around 60 ka ap.

2.8 Summary and Conclusions

In this chapter we have reviewed the early time series techniques used to analyse palaeoclimatic records. We then looked at the various spectral techniques used to analyse the periodic nature of palaeoclimatic data. There is a set suite of analyses which appear in many palaeoclimatic papers, based on the Fourier techniques of Blackman and Tukey (1958) and Jenkins and Watts (1968). These have been very succesful in the advancement of our understanding of the processes by which climate change occurs, and in the confirmation of the Milankovitch theory.

Finally, we have investigated past attempts to model the ice age variations. These have taken many different approaches, with varying degrees of success. We hope to build on these in later chapters by allowing our models to be non-linear.

We now go on to investigate the Complex Demodulation technique. All the spectral techniques discussed in this chapter can help identify the frequencies present in a time series. However, to gain any insight into the amplitude variations through time of that frequency, it would be necessary to carry out an evolutionary analysis by sliding a window along the data. This is not always possible, due to the length of the time series relative to the frequency of interest. Complex Demodulation enables us to retrieve this information on a time series which is lost

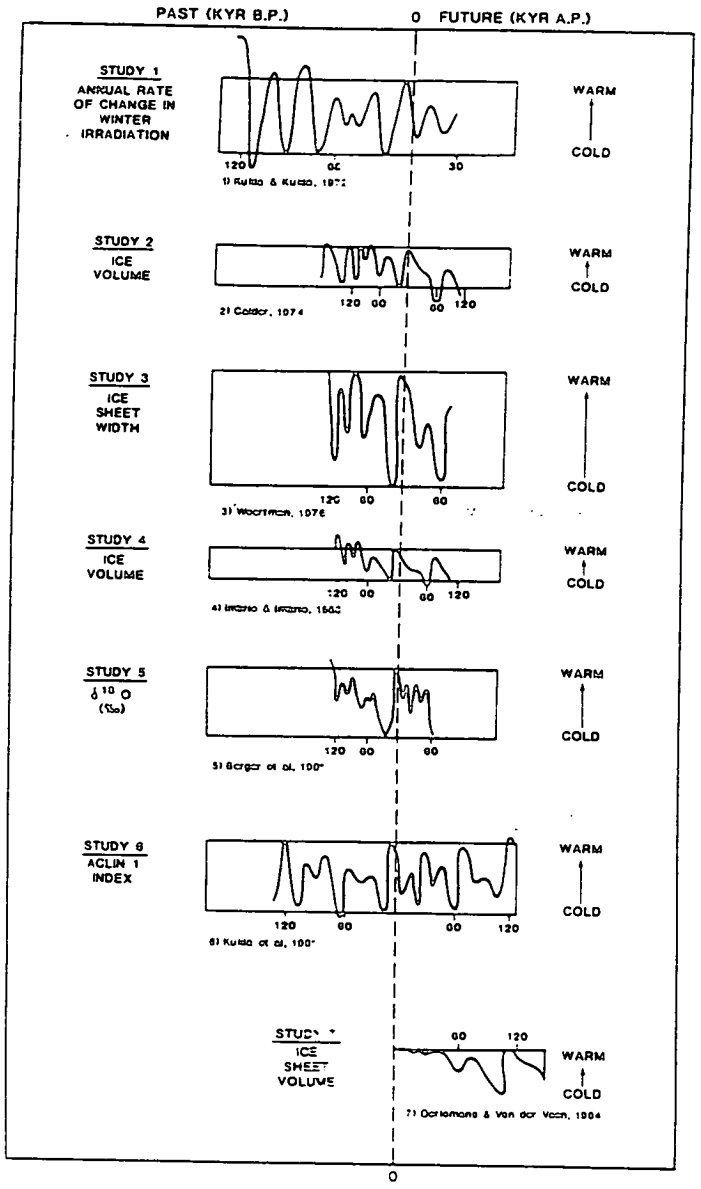

Figure 2.6. A selection of future climate predictions, inlcuding several of the models considered here. All models imply a long term cooling from the present day, culminating in a glacial maximum at around 60 ka ap. From Goodess and Palutikof (1991a).

in spectral analysis. In addition, Complex Demodulation allows us to investigate the phase variations in the frequency of interest.

Analysis such as this has obvious applications in comparing the amplitude and phase variations in palaeoclimatic and orbital/insolation time series, both to confirm the causal relationship between the two, and to investigate any variations in that relationship.

Chapter 3

Complex Demodulation

3.1 Introduction

Whilst the concept of the Milankovitch theory is now widely accepted there are still sceptics. With the advent of "tuning" (Section 1.4.4) accusations of using circular arguments to support the theory have been made. Particular objections include tuning and then using coincident spectral peaks as evidence of orbital forcing. However, if it could be shown that the amplitude variations at the orbital periods were correlated in the input and output then this would be evidence for orbital forcing which could not be ignored as a side-effect of the tuning procedure. Using Complex Demodulation (Tukey 1961, Bingham et al. 1967, Bloomfield 1976) will enable us to make this comparison. It will also provide information on the phase behaviour of the periods in the input (orbital variations) and output (palaeoclimate), and enable us to compare them.

The aims of this chapter are therefore as follows:

- To introduce the technique of Complex Demodulation;
- To document the application of Complex Demodulation, with particular reference to the statistical software package S-Plus;
- To apply Complex Demodulation to a range of palaeoclimatic datasets;
- To draw any possible conclusions about the forcing and behaviour of past climate;
- To investigate the overall suitability of Complex Demodulation for application to palaeoclimatic data, and any advantages it may have over the more

prevalent techniques.

3.2 Theory

Following Bloomfield (1976), assume that the data contain a periodic component

$$R_t \cos(\lambda t + \phi_t), \tag{3.1}$$

where R_t is a slowly changing amplitude and ϕ_t is a slowly changing phase. The aim of Complex Demodulation is to extract the series $\{R_t\}$ and $\{\phi_t\}$.

More generally, the data $\{x_t\}$ are of the form

$$x_t = R_t \cos(\lambda t + \phi_t) + z_t \tag{3.2}$$

where $\{z_t\}$ are the additional terms in the data, such as other harmonic terms (not at frequency λ), ARIMA components, noise etc.

Define $\{y_t\}$ by

$$\begin{aligned} y_t &= x_t \exp\{-i\lambda t\} && (3.3)\\ &= \frac{1}{2} R_t \exp\{-i\lambda t\} [\exp\{i(\lambda t + \phi_t)\} + \exp\{-i(\lambda t + \phi_t)\}] \\ &\quad + z_t \exp\{-i\lambda t\} && (3.4)\\ &= \frac{1}{2} R_t \exp\{i\phi_t\} + \frac{1}{2} R_t \exp\{-i(2\lambda t + \phi_t)\} + z_t \exp\{-i\lambda t\}. && (3.5) \end{aligned}$$

Then we say that $\{y_t\}$ is obtained from $\{x_t\}$ by Complex Demodulation. We are interested in extracting the first term, which must be smooth since R_t and ϕ_t are assumed smooth. The second term contains frequency 2λ. We are assuming that z_t has no power at frequency λ, so therefore the third term contains no frequency component at zero, i.e. it is not smooth. We wish to extract the smooth component of y_t, whence recovery of R_t and ϕ_t is simple. To achieve this we must apply a low-pass filter to the data. This has the desired effect of removing all frequencies above a certain value from the data, thereby leaving us with the required lower-frequency information, i.e. the smooth component.

3.3 Advantages of Complex Demodulation

The technique of spectral analysis (Jenkins and Watts 1968, Bloomfield 1976, Priestley 1981) gives information on the wavelengths present in a time series. However, it assumes stationarity, which implies that frequencies in the data are constant in amplitude and phase over the time-span of the data. Unfortunately, this assumption is often incorrect, particularly in palaeoclimatic data where there is strong modulation from the orbital variations. Moreover, any amplitude and phase variation within the data can make interpretation of the spectral analysis very difficult.

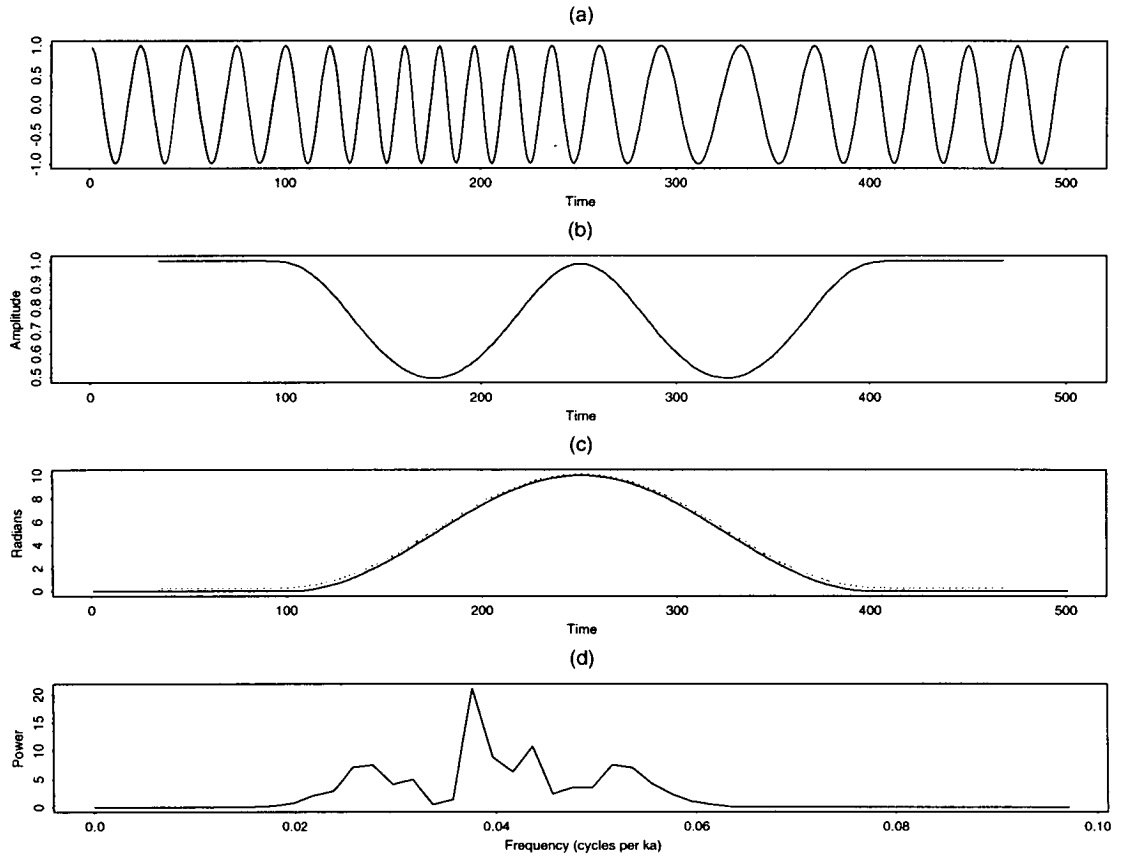

Figure 3.1. (a) A synthetic cosine based time series, wavelength 25 units, but with varying phase; (b) the Complex Demodulation amplitude estimate. During periods when the phase is changing the amplitude estimate is low as the frequency is not exactly 0.04; (c) the Complex Demodulation phase estimate (dashed line) and the real phase values. Complex Demodulation accurately extracts the phase behaviour; and, (d) the spectral analysis of the data showing the inconclusive periodogram, with a peak near (but not at) 0.04, and several other concentrations of power.

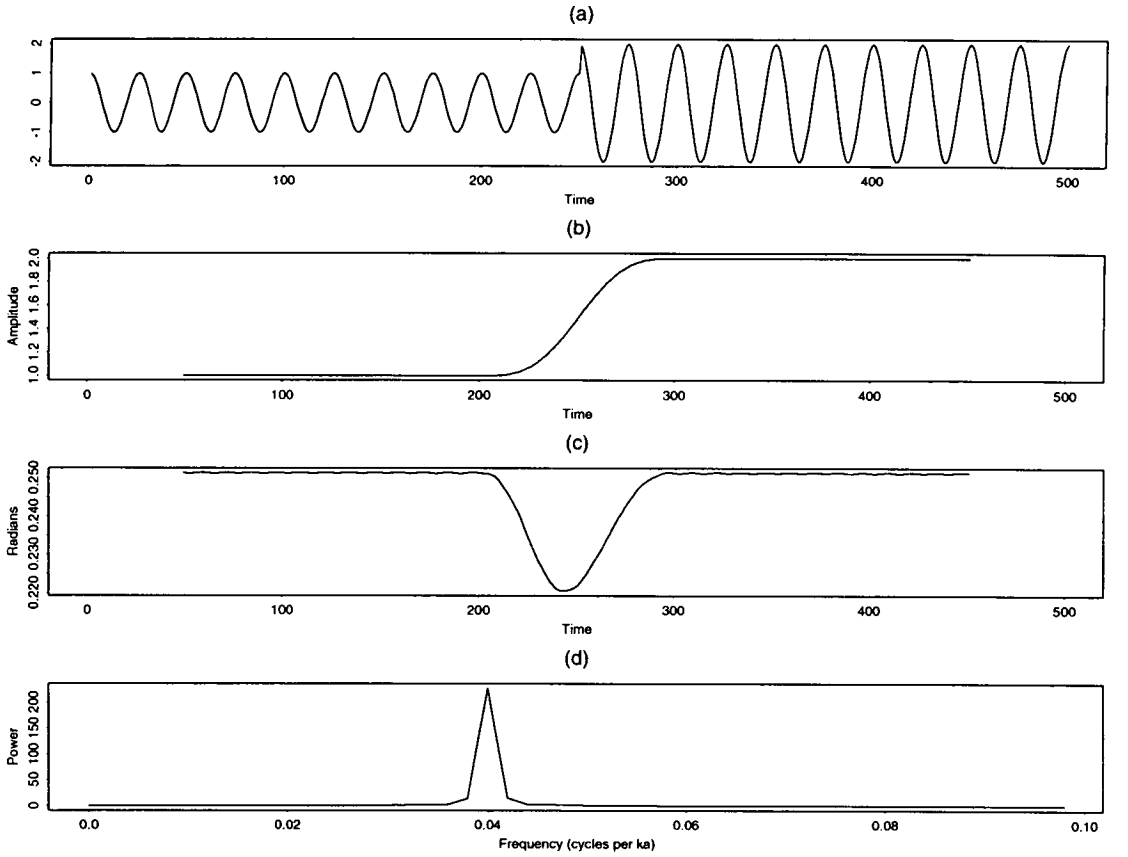

Figure 3.2. (a) A synthetic cosine based time series, wavelength 25 units, with a step change in the amplitude; (b) the Complex Demodulation amplitude estimate which correctly indicates the amplitude change but smooths out the transition period; (c) the Complex Demodulation phase estimate, indicating the interdependence of the amplitude and phase; and, (d) the spectral analysis of the data, indicating very clearly the 0.04 frequency, but giving no indication of the amplitude variation.

To illustrate this problem, Figure 3.1 shows a simple cosine wave with a smoothly varying phase. It is defined by

$$x_t = \cos(\frac{2\pi t}{25} + \phi_t) \tag{3.6}$$

where ϕ_t is 0 for $0 < t < 100$ and $400 < t < 500$. For the intermediate section, ϕ_t is defined to slowly rise and fall, as illustrated in Figure 3.1(c). While the phase is increasing the wavelength is reduced, and when the phase is decreasing the wavelength is increased. The Complex Demodulation analysis of Figure 3.1 shows that we correctly estimate the phase change, and the amplitude estimate signifies the sections when the 0.04 frequency is weakest. However, the Fourier spectral analysis shows a large concentration of power over a very wide frequency band. The spectral analysis has clearly not given an indication of the harmonic behaviour of the data. In the case of changing amplitude, Figure 3.2 shows a cosine wave, again of wavelength 25 time units, but this time with a step change in the amplitude. The Fourier spectral analysis correctly estimates the wavelength in the data, but gives no indication of the amplitude variation. In contrast, Complex Demodulation captures the amplitude change well.

Complex Demodulation can be seen as a quantitative extension of the band-pass filter technique (Blackman and Tukey 1958), a method which is part of the "stock" analysis regularly carried out on palaeoclimatic data e.g. Hays et al. (1976),Imbrie et al. (1984),Ruddiman et al. (1986). Thus Complex Demodulation has obvious applications to climate analysis on the $10^3 - 10^6$ years timescales, where we are interested in analysing the orbital periods present in the data.

3.4 Previous Applications

Complex Demodulation has been applied to a wide range of geophysical time series, including geomagnetic data (Banks 1975), century/decade scale climate change (Thompson 1994), and satellite altimeter data (Francis and Berge 1993). It has also been applied to palaeoclimatic data (Kominz et al. 1979, Pisias and Moore 1981, Pisias et al. 1990). In the first two of these papers Complex Demodulation was employed to extend the time scales for isotopic data sets. The phase estimates from obliquity and the prefiltered data were compared, and an estimate made of the lag between orbital variation and climate at the 41 ka frequency band. This single lag estimate was then assumed to be constant and the timescale set.

Pisias et al. (1990) used the amplitude estimates to estimate the response time of the Earth's climate system at the 41 and 23 ka frequency bands, assuming that the Earth is a simple linear system. This is a reasonable assumption as it is generally agreed that the Earth responds in a linear fashion to precession and obliquity variations e.g. Hays et al. (1976). Pisias et al. (1990) used the varying response time to update their chronology. This paper also indicates the added information available from Complex Demodulation in comparison with a bandpass filter. A bandpass filter was applied and then Complex Demodulation used to quantify the resultant amplitude and phase variations. However, the application of the bandpass filter was unnecessary as Complex Demodulation can retrieve this information directly from the original data.

3.5 Filtering

To extract the smooth component of Equation 3.5 we must remove all the frequencies which it contains. These are:

2λ : From the second term in Equation 3.5.

λ and 3λ : From Bloomfield (1976) we have that z_t contains a low-frequency term and the second harmonic of λ, so that the third term in Equation 3.5 will contain power at λ and 3λ.

Consequently, the filter we use to extract the smooth series must have zeros at λ, 2λ, and 3λ, and be near zero in regions surrounding these three frequencies.

Ideally we would like to use a low-pass filter to remove the above harmonic terms and therefore extract the smooth portion of Equation 3.5. An ideal low-pass filter will remove all frequencies in a time series above a certain frequency, thus leaving only the lower frequency, smooth portion of the data. This ideal low-pass filter would leave all frequencies less than some cut-off frequency f_c unchanged, but pass no others. Such a filter does not exist exactly, but can be approximated sufficiently well by designing a fixed length filter using the least squares approximation method (Bloomfield 1976).

3.5.1 Implementation on S-Plus

Using the demod function on S-Plus we are required to prescribe three parameters. These are:

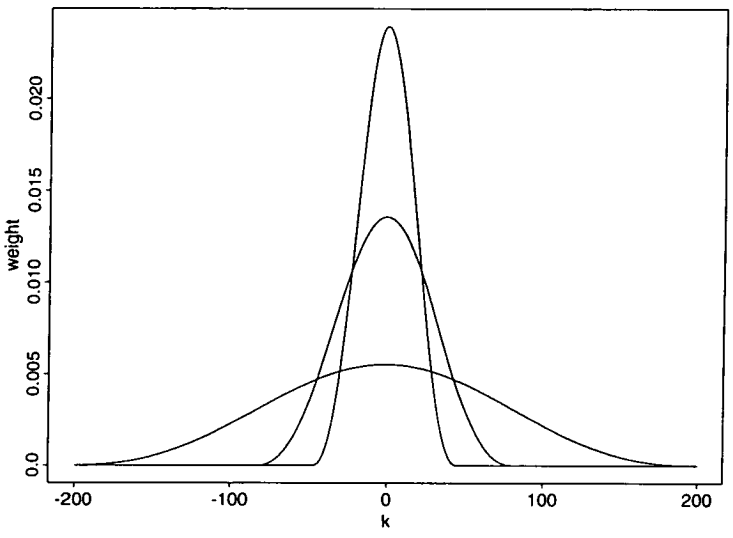

Figure 3.3. The weights of the three filters used for extracting the 100, 41, and 23 ka periodicities in the Complex Demodulation analysis

Centre frequency λ : The frequency in which we are interested;

Pass frequency f_p : All frequencies lower than f_p will be passed completely;

Stop frequency f_s : All frequencies higher than f_s will be blocked completely.

The cut-off frequency f_c is the average of the pass and stop frequencies, and can be seen as approximating the cut-off value in an ideal filter. The number of terms in the filter is then

$$n = \left\lfloor 2\, max\left\{2, \frac{1}{\Delta_t(f_s - f_p)}\right\} + 1 \right\rfloor \tag{3.7}$$

where Δ_t is the time interval between data points and $\lfloor x \rfloor$ is the largest integer smaller than x. By setting the pass frequency at zero and the stop frequency smaller than λ, we remove all the undesired frequencies, but we must be careful not to make f_s too small as we then lose detail in our amplitude and phase estimates. An additional concern when choosing the filter is that the total number of points lost in the filtering is $n - 1$, so the larger the filter the larger the loss of information at the data tails. Figure 3.3 shows the weights of the three filters used in extracting the 100, 41 and 23 ka periodicities in the palaeoclimate data.

To illustrate the effect of different filters, Figures 3.4 and 3.5 show analyses of the 41 ka cycle in the insolation data for three different filters. Figure 3.4 shows

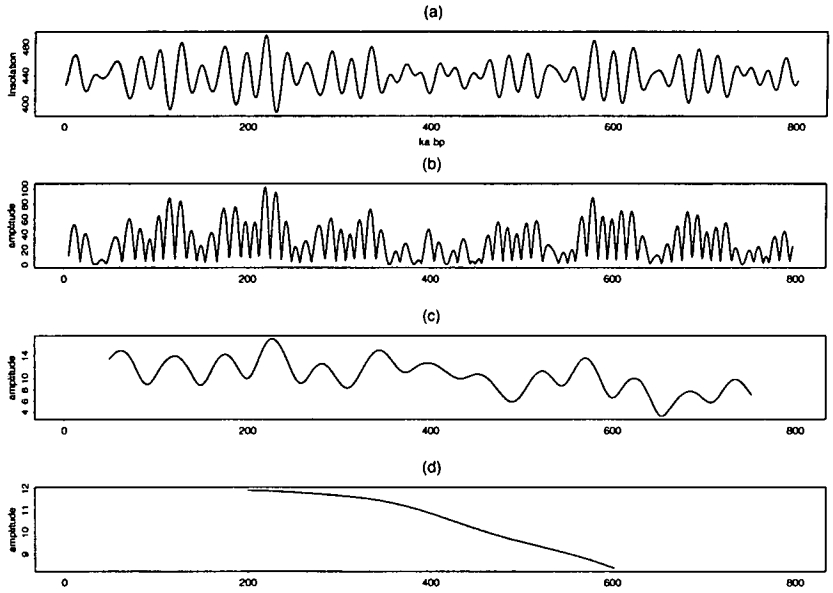

Figure 3.4. (a) An insolation time series and (b-d) three different estimates of the amplitude of the 41 ka wavelength, from three different filters. In (b) the filter has too low a cutoff, producing an amplitude estimate which includes unwanted, higher frequency information. In (d) the filter has too high a cutoff, and produces only the very long term trend in the amplitude. In (c) the filter balances the need to remove the higher frequency detail and the need to pass the lower frequency information relating to the amplitude variations.

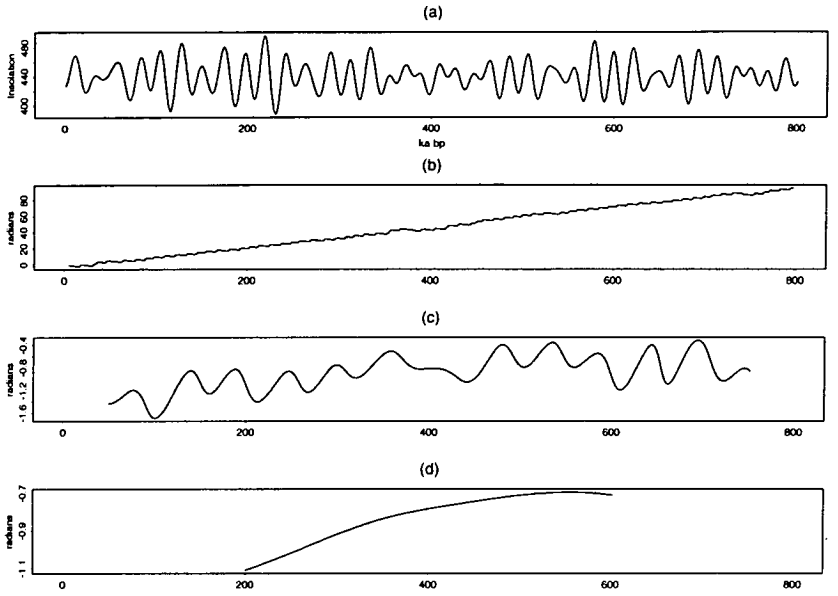

Figure 3.5. (a) An insolation time series and (b-d) three different estimates of the phase of the 41 ka wavelength, from three different filters. Details as for Figure 3.4.

the resultant amplitude estimates and Figure 3.5 the phase estimates. In the first amplitude analysis f_s is larger than λ so we do not remove that frequency and consequently our estimate contains unwanted, higher frequency information. In the third analysis f_s is too small, so we are removing nearly all the detail, and also we only obtain estimates for half of the data. However, the second analysis seems to balance the amount of information passed and the data loss very well. In the phase analysis we see that the first filter is passing λ, and therefore the reason for the linear increase in the phase is that it is detecting the λ frequency. As with the amplitude, the third filter is too narrow, and the second one gives the best results.

In general, a pass frequency of zero and a stop frequency of around $\lambda/2$ proved ideal, as this passed a suitable amount of detail, removed the unwanted frequencies, and did not give too large a data loss at the tails.

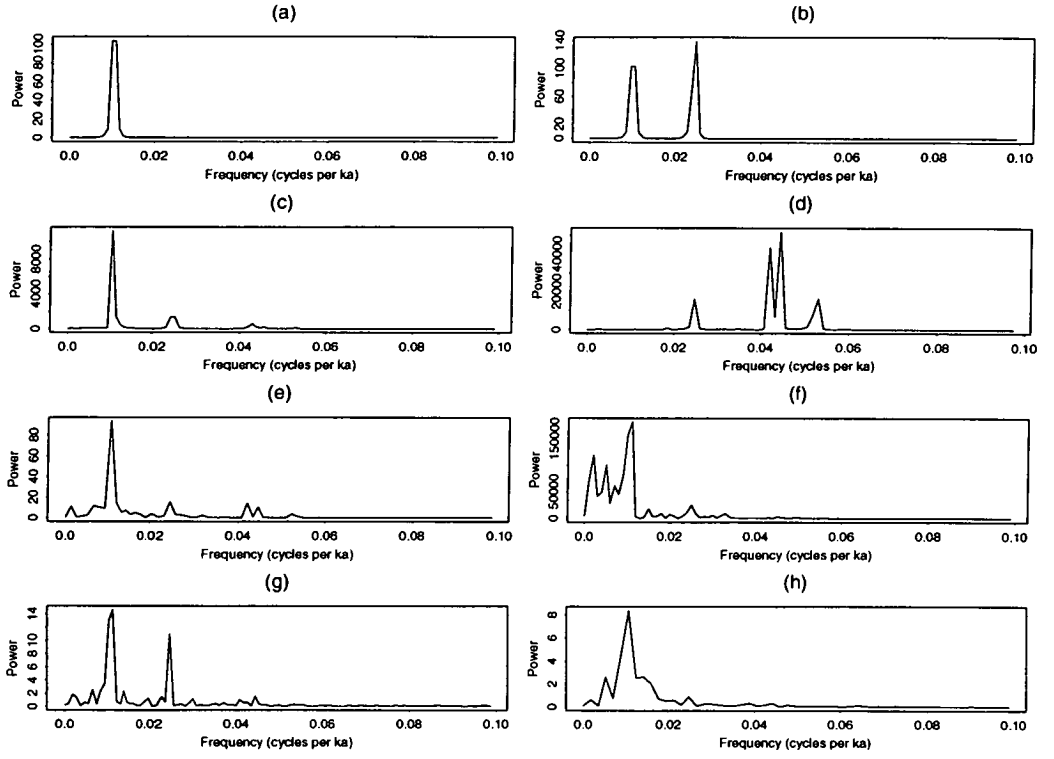

Figure 3.6. Fourier spectral analysis of the time series analysed in this chapter. (a) single cosine synthetic data, (b) double cosine synthetic data, (c) four cosine synthetic data, (d) July 65N insolation, (e) SPECMAP, (f) Loess, (g) ODP 677, (h) Devil's Hole.

3.6 Results

In order for us to compare Spectral Analysis and Complex Demodulation, the periodogram of each data set is shown in Figure 3.6. As will be seen later, there are cycles in the data which have negligible spectral peaks but upon closer analysis reveal good correlation with the corresponding orbital inputs.

3.6.1 Synthetic Data

Initial analysis on two simple, synthetic data sets is carried out. The first is a simple cosine with period 100. The second contains 2 cosines, one at period 100, and one at 41 (two of the periods we will be interested in extracting from palaeoclimatic data at 1000 year intervals). Each data set is 1024 points long. In both examples Complex Demodulation accurately removes the unit amplitudes

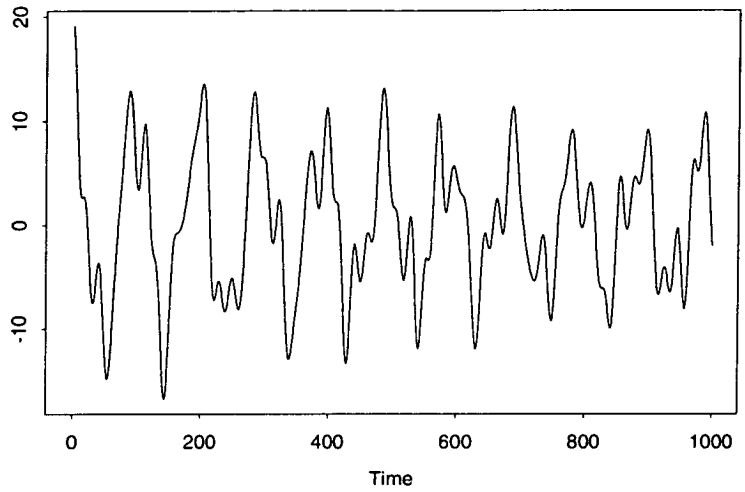

Figure 3.7. The synthetic time series $y(t)$ as described in Equation 3.8. This is constructed from four cosines of wavelength 100, 41, 23 and 19 units (the Milankovitch periods for data at 1 ka intervals) with smoothly varying amplitudes and phases.

and the constant phases for all three cosines.

A further, more complicated, synthetic data set (Figure 3.7) was constructed and analysed. This time series contains cosines at frequencies 100, 41, 23, and 19 (the 4 Milankovitch frequencies for data at 1000 year intervals), but this time with smoothly varying amplitudes and phases:

$$\begin{aligned} y(t) &= 3r_{t,100}\cos\left(\frac{2\pi t}{100}+p_{t,100}\right)+r_{t,41}\cos\left(\frac{2\pi t}{41}+p_{t,41}\right)+ \\ &\quad 0.5r_{t,23}\cos\left(\frac{2\pi t}{23}+p_{t,23}\right)+r_{t,19}\cos\left(\frac{2\pi t}{19}+p_{t,19}\right). \end{aligned} \tag{3.8}$$

The spectral analysis of $y(t)$ is shown in Figure 3.6. It correctly identifies the 100 periodicity, has another broader peak at 41.67/40, and also smaller peaks at 23.2, 21.74, and 18.87. This order of importance corresponds with the average amplitude of each period in the data. So, spectral analysis has identified the cosine waves in the data, but can give no information on whether they are constant through the time series. The varying amplitudes and phases ($r_{t,100}, p_{t,100}$ etc.) are shown in Figures 3.8 and 3.9, along with the estimates from Complex Demodulation.

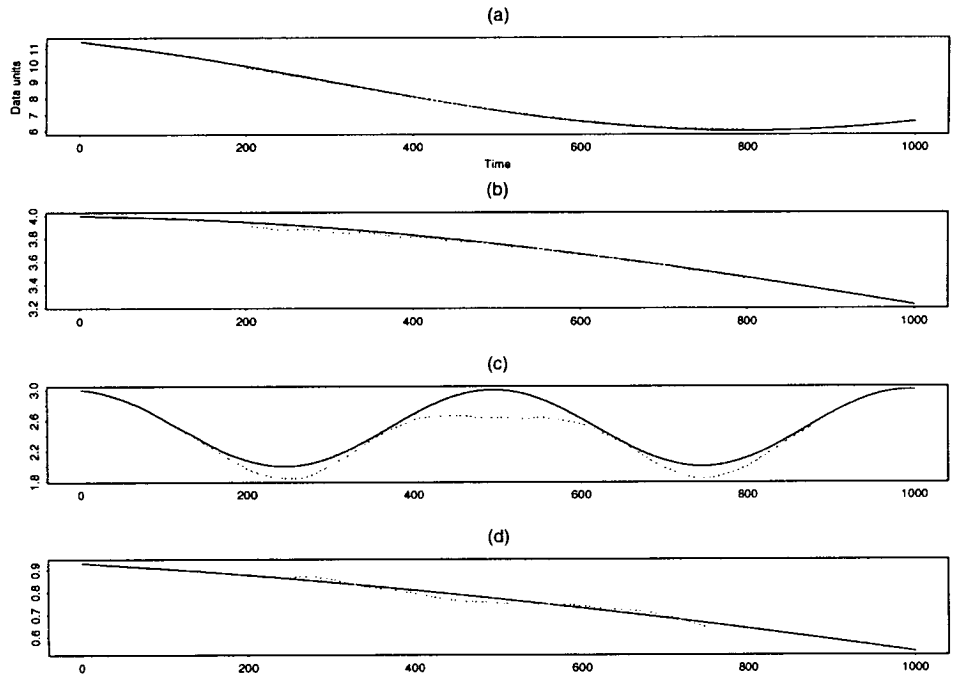

Figure 3.8. The Complex Demodulation estimates of (a) r_{100}, (b) r_{41}, (c) r_{23}, (d) r_{19}. Solid lines are actual values,dashed lines are estimates. In all cases, Complex Demodulation captures the amplitude variations very well. The poorest results are for the amplitude of the 23 unit frequency, but these are due to the simultaneous phase changes in the data c.f. Figure 3.2.

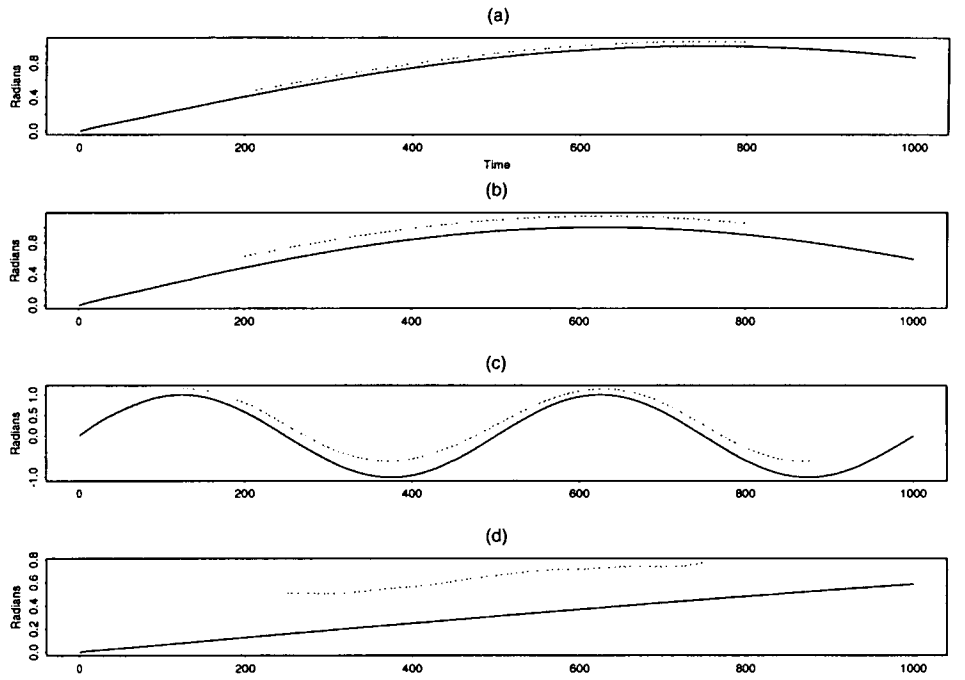

Figure 3.9. The Complex Demodulation estimates of (a) p_{100}, (b) p_{41}, (c) p_{23}, (d) p_{19}. Solid lines are actual values, dashed lines are estimates. Complex Demodulation extracts all the variations well. In some of the analyses, particularly (d), we observe that there is a phase lag between the actual values and our estimates. We will be predominantly interested in variations in phase, not absolute values, which wil be unaffected by this, but it must be borne in mind in all future analyses.

The results obtained are generally excellent, following the variations in amplitude and phase very closely. In particular, the results for the 23-unit wavelength are excellent given the complex variations in its amplitude and phase. The results for the 19-unit wavelength are the weakest, but still extract the long term behaviour (increasing phase, decreasing amplitude) This cycle is the least important in the data set (it has by far the smallest amplitude), so we are seeing evidence of the difficulty in extracting the minor periods in a dataset. However, in general we pick out the many of the features of the amplitude and phase changes, and this augurs well for analysis of real data.

The above analyses illustrate that much of the comparison between two amplitudes or phases must be qualitative, and that visual comparison of patterns in two records is very important.

3.6.2 Orbital Parameters and July 65N Insolation

These have been analysed for the last 800 ka to enable comparison with palaeoclimatic records such as SPECMAP and Devil's Hole. This analysis can also be looked on as useful test data as it is smooth and the "answer" is sometimes known. In particular, the amplitude of the precession variable is eccentricity.

Figure 3.6 shows the spectral analysis of the July 65N insolation record. This has 4 dominant periods: 40.5 ka, 23.8 ka, 22.5 ka, and 18.8 ka. These represent obliquity and the three precession terms. Note that there is no visible period in the 100 ka region (see Section 1.3.4 for discussion of this apparent anomaly).

Eccentricity and the 100 ka insolation cycle (Figure 3.10) The analysis is centred around the 100 ka periodicity, and picks out the amplitude well, and the step in the phase matches up with the shorter cycle centred at 400 ka bp. This phase change is 2.05 radians, equating to a change of 32.7 ka, so for this one cycle the ecccentricity period is approximately 67 ka. The insolation analysis corresponds well with the eccentricity analysis, showing the dip in amplitude at 400 ka bp and the corresponding step in the phase. It is a sign of the strength of the method that we can extract the eccentricity signal, given that the eccentricity component in insolation has very little spectral power (Section 1.1).

Obliquity and 41 ka insolation cycle (Figure 3.11) Centred on 41 ka, the

amplitude estimate is good, highlighting the cyclic reduction in overall amplitude. The gradual increase in phase signifies that the period is not precisely 41 ka. It is possible to use the slope in such cases to gain an improved estimate of the actual period. If the results show a general monotonic increase or decrease in the phase then this signifies that our estimate of λ is slightly out from the true value. Here, between 100 and 500 ka bp, the phase change is 0.744 radians, or 4.85 ka, which gives an estimate of the periodicity as 40.5 ka. The two dominant periods in the obliquity cycle are (from Berger and Loutre (1991)), 41 ka and 39.7 ka, so our estimate of 40.5 is reflecting the combination of these terms. Again, in the insolation analysis, we are able to extract the obliquity signal very well, with its decreasing amplitude and increasing phase.

Precession, $e \sin \omega$, and 23 ka insolation cycle (Figure 3.12) Analysis is centred on the 23 ka period. The amplitude estimate matches very well the eccentricity for the same period, and this is "correct" as precession is a sine wave modulated by the eccentricity. The phase results highlight the problems which arise when the amplitude is near 0. When the amplitude is very small the signal is very weak and estimation of the phase is less precise. Therefore, phase changes such as those around 400 and 750 ka bp must be treated with caution. The insolation analysis picks out the precession signal very well, capturing the variations in amplitude and the dip in phase.

These results show the strengths of Complex Demodulation, and we now go on to use these results in a comparison with palaeoclimatic data. Throughout this chapter we have focussed on the periodicities at 100, 41 and 23 ka. For some of the following data sets these are not the exact periods found in the data. However, to enable comparison between records all analysis is done using these periods. This is justifiable as our filtering methodology will pass a band of frequencies around the λ used, and also the spectral estimates are not exact due to the finite resolution of the periodogram.

3.6.3 SPECMAP

Spectral Analysis of the SPECMAP record is shown in Figure 3.6. The dominant period is 98 ka, with additional peaks at 41 ka, 23.7 ka, 22.4 ka and 19 ka. However, the presence of the Milankovitch frequencies is not necesarily evidence

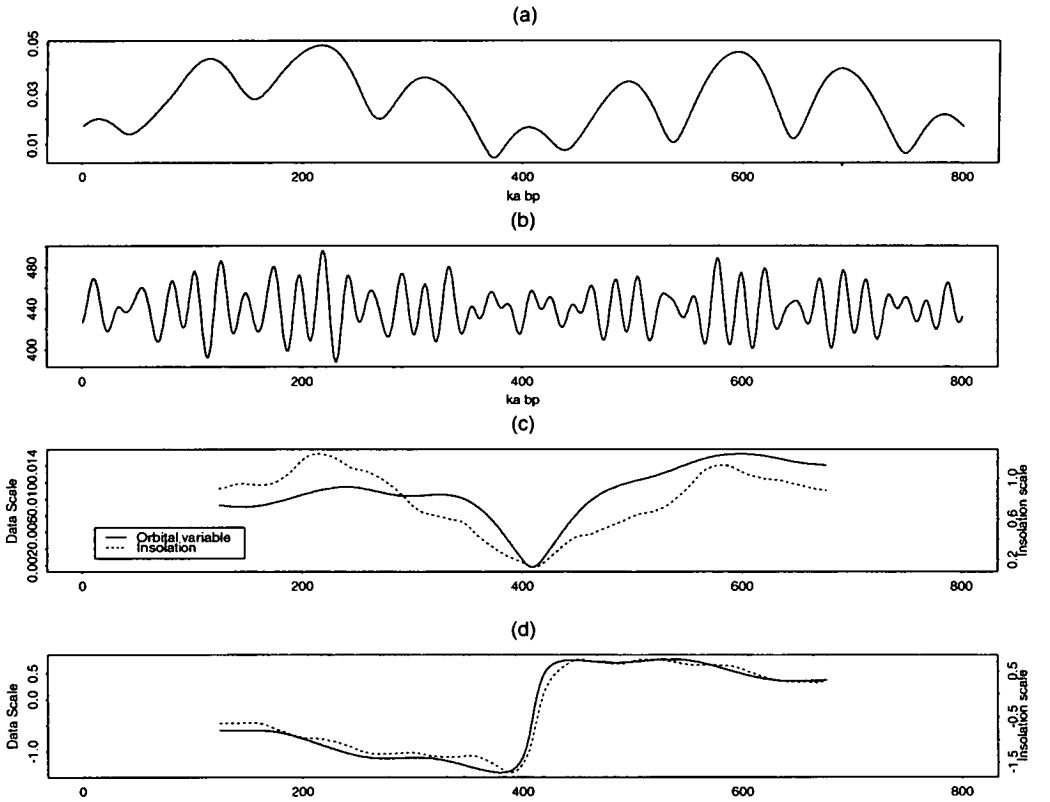

Figure 3.10. (a) Eccentricity and (b) July 65N for the last 800 ka, (c) amplitude estimates of the 100 ka wavelength in each, and (d) phase estimates. Unlike spectral anlaysis, Complex Demodulation confirms the similarities of the 100 ka variations in eccentricity and insolation data.

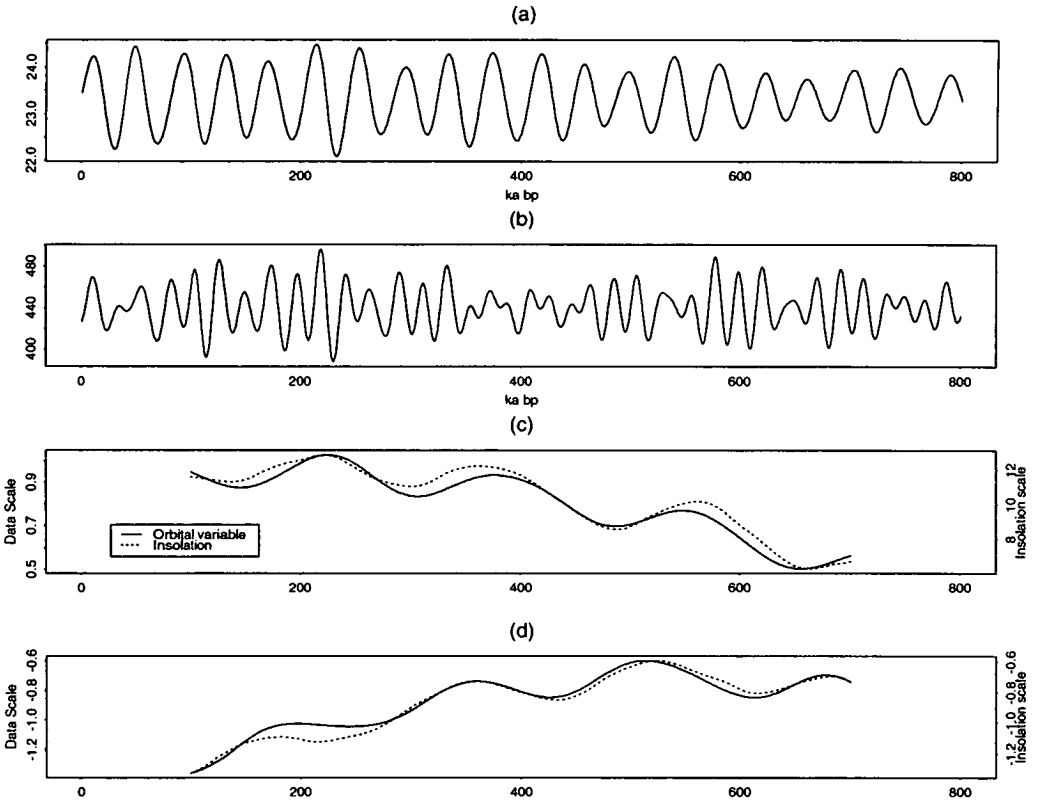

Figure 3.11. (a) Obliquity and (b) July 65N for the last 800 ka, (c) amplitude estimates of the 41 ka wavelength in each, and (d) phase estimates.

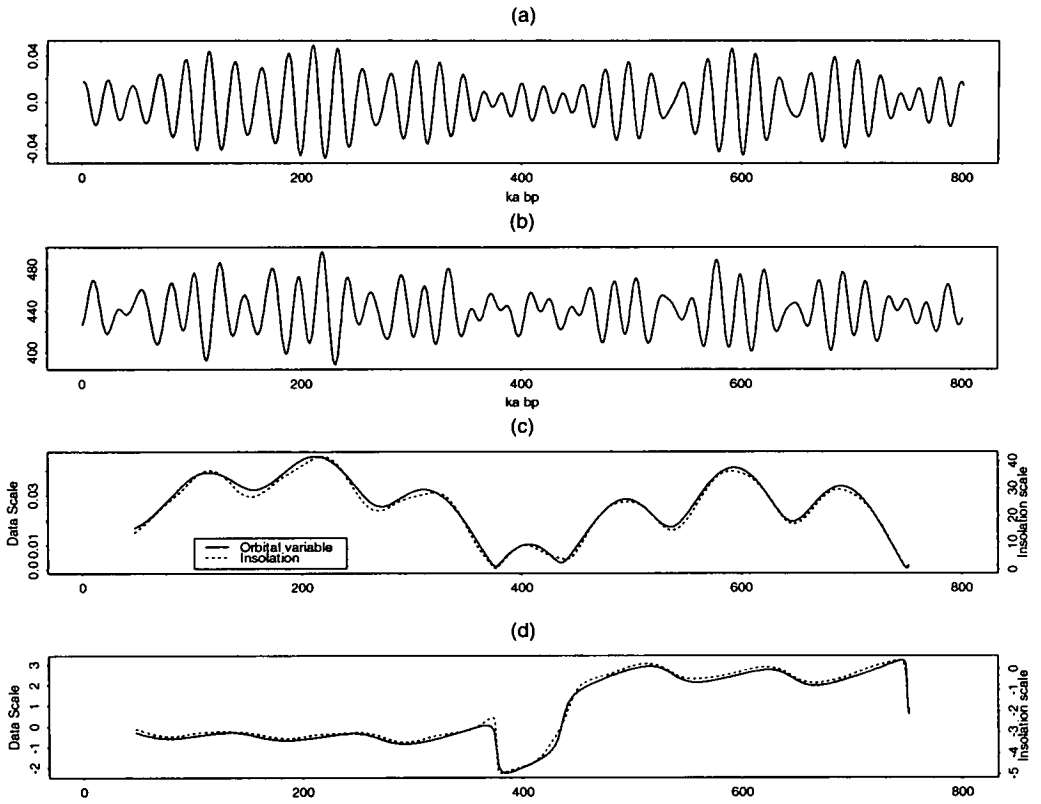

Figure 3.12. (a) Precession and (b) July 65N for the last 800 ka, (c) amplitude estimates of the 23 ka wavelength in each, and (d) phase estimates.

for orbital forcing as the record was dated by "tuning" to obliquity and precession, and thus could be expected to contain these periods (although the presence of both orbital periods around 23 ka is highly suggestive).

There is now considerable evidence for an error in the dating of the SPECMAP record at around 617 ka bp (Section 1.5.1) and it will be a good test of Complex Demodulation as to whether or not it captures this.

100 ka cycle (Figure 3.13) The amplitude result looks very good in that it follows the data well, but there is no obvious correlation betweeen these results and the eccentricity. For example at 400 ka bp, the eccentricity amplitude is very low but there is a strong 100 ka period in the climate of that period. Thus we see no clear evidence for eccentricity forcing of the amplitude of the 100 ka period in climate. However, there is some similarity in the phase behaviour, particularly from 350 ka bp. Since then, the phases have been increasing steadily. Prior to this the phase values were both higher.

41 ka cycle (Figure 3.14) The predominant feature of this analysis is the sudden change in the phase just before 600 ka bp. So, as hoped, this Complex Demodulation analysis is highlighting the timescale error. The dating mistake was in the tuning where an obliquity cycle was missed in the record. (Note that this is related to the debate about the timing of the Brunhes/Matuyama magnetic reversal boundary (Shackleton et al. 1990)). The amplitude signal appears to match the rough features of the insolation analysis with a cyclic decrease back in time. However, there are obvious differences at approximately 200 and 500-600 ka bp. Pisias et al. (1990) obtained similar results, with a relatively poor similarity in amplitude (they claimed due to the low coherency at this frequency). Similarly, we have that the times of high amplitude in the SPECMAP 41ka cycle correspond with periods of rapid deglaciation. This suggests a link between obliquity and the deglaciations, and therefore implies a role for obliquity in the 100 ka ice age cycle (see Chapter 5, and Imbrie et al. (1993))

23 ka cycle (Figure 3.15) These results show a good correspondence with the precession results. The amplitude value is low around 400 ka bp, as for the insolation, with higher values at other times. This result signifies the strongest evidence for the Milankovitch theory from the analysis of the

SPECMAP data. These similarities in the amplitude behaviour can not be considered to be artefacts of the dating procedure. However, closer examination shows that the timing of the peaks and troughs is such that the changes in amplitude in the data precede those in the insolation. This result is impossible to explain in the context of the Milankovitch theory. The phase behaviour is relatively constant for both records, apart from the large changes around 400 ka bp. During the constant periods there are small ripples in the phase and these correspond well with each other (in particular during 450-700 ka bp). The phase changes in the middle of the record do not correlate exactly, particularly the SPECMAP phase change at 450 ka bp, but the trough and rise between 400 and 350 ka bp are similar in timing and magnitude (1.8 radians, or 6.6 ka). However, as mentioned earlier, if the amplitude of interest is very low then estimation of the corresponding phase is less reliable. At 50 ka bp, the phase difference is 4 radians, implying a lag of 14.6 ka between the precession input and the corresponding cycle in the output. It is interesting that the phase behaviour does not reflect the dating error, as the SPECMAP tuning was done using both obliquity and precession, with the emphasis on precession. However, both here and in Thomson (1990a) no major change in the precession phase is found.

3.6.4 Loess

The Chinese Loess record (Kukla et al. 1990) is a measure of magnetic variations in terrestrial sediments. The sediment consists of soils during interglacials and loess (windblown dust) during the drier glacial periods (Section 1.5.2). Spectral analysis of the Loess record (Figure 3.6) shows that most of the variation is at low frequencies with a dominant 91 ka peak. There is also a small 40 ka peak.

100 ka cycle (Figure 3.16) The amplitude has a maximum at around 450 ka bp, just before the minimum in the eccentricity, so there is little correlation. The phase behaviour is generally constant in input and output, apart from the step changes when the amplitudes are near zero. Hence, again, no relationship can be deduced.

41 ka cycle (Figure 3.17) The amplitude plots here both show highest values for the 350-100 ka bp period, with lower values prior to this. The phase

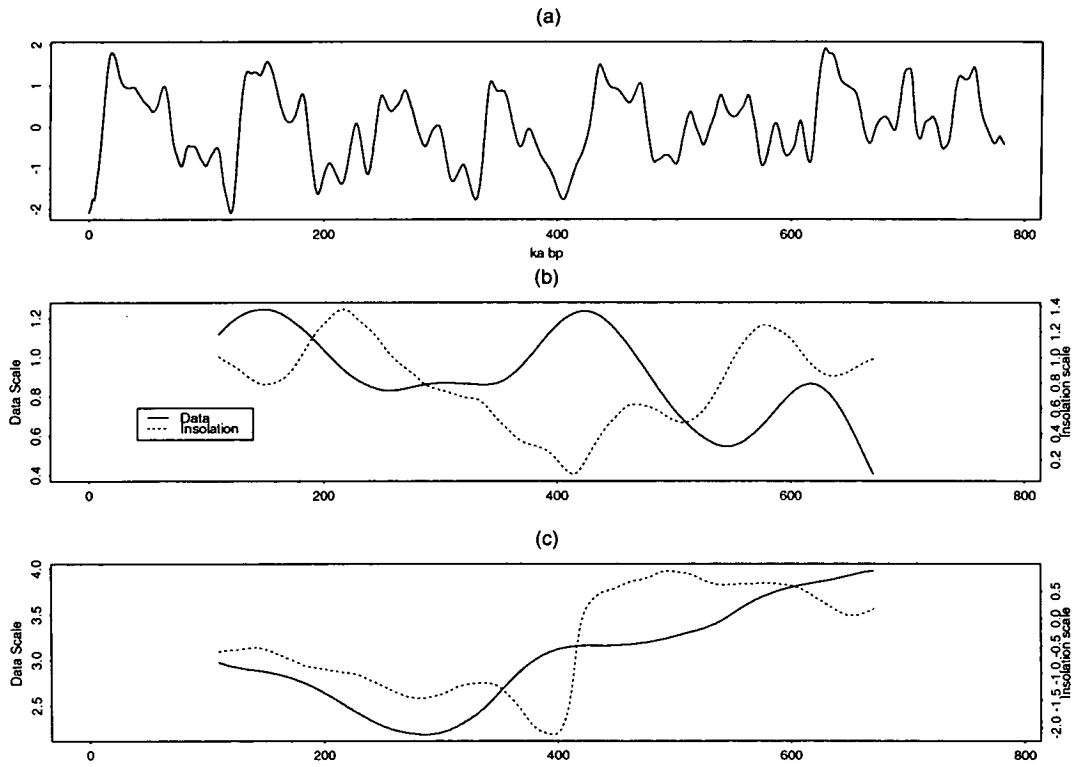

Figure 3.13. Complex Demodulation analysis of the 100 ka frequency in SPECMAP: (a) the data, (b) amplitude estimates and (c) phase estimates for the data and the insolation. There is no obvious correlation between the behaviour in the SPECMAP record and the eccentricity variations. See text for further details.

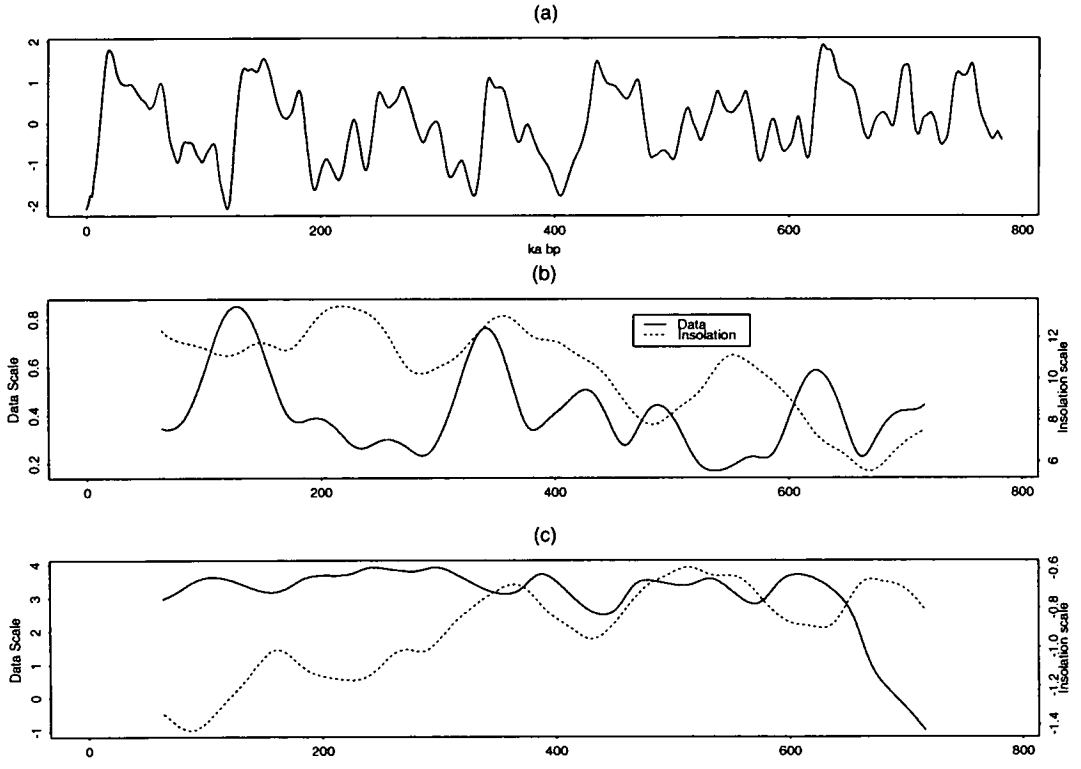

Figure 3.14. Complex Demodulation analysis of the 41 ka frequency in SPECMAP: (a) the data, (b) amplitude estimates and (c) phase estimates for the data and the insolation. The two main features are the correspondence between periods of high amplitude and deglaciations, and the apparent phase change in the older section of the record, confirming the dating error in the SPECMAP time series. See text for further details.

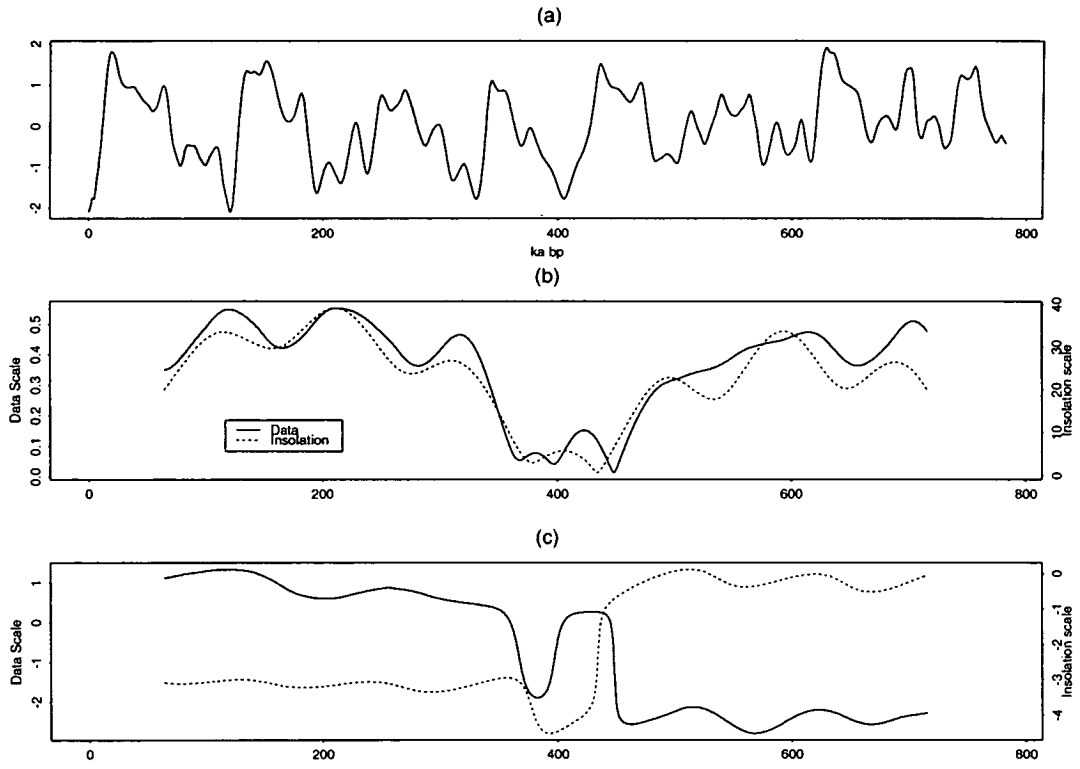

Figure 3.15. Complex Demodulation analysis of the 23 ka frequency in SPECMAP: (a) the data, (b) amplitude estimates and (c) phase estimates for the data and the insolation. The amplitude variations show that the eccentricity modulation of the precession effect is clearly visible in the climate record. The phase changes aswell are very similar, as the large step changes occur due to periods of near-zero amplitude and are therefore unreliable. See text for further details.

behaviour in the loess is constant back to 600 ka bp. In the period 900-600 ka bp we see a progressive increase in the phase, indicating that the wavelength has changed during that period. The phase change is 11 radians in 300 ka, implying that the wavelength of interest is actually 31.2 ka during this period. In Kukla et al. (1990), they carried out Evolutive Maximum Entropy Spectral Analysis of the data (back to 736 ka bp). This involves sliding a window along the data and analysing how the spectral features change temporally. This indicated a shift in the 41 ka wavelength to around 30 ka in the oldest window. This is the same property highlighted here by Complex Demodulation. This is a consequence of dating of the record using an incorrect estimate of the age of the Brunhes-Matuyama magnetic reversal Kukla et al. (1990).

23 ka cycle (Figure 3.18) Here, the amplitude plot has the characteristic minima around 400 and 800 ka bp, and maximum at around 200 ka bp. The signal around 600 ka bp is less conclusive, with a period of strong 23 ka periodicity input around 600 ka bp coinciding with a low point in the loess, and then a peak at 650 ka bp in the loess record. This may signify a dating problem in the Loess record around 600 ka, leading to a loss of the 23 ak signal. Therefore, as with the SPECMAP record, the strongest similarity between insolation and the data is in the amplitude of the 23 ka cycle. The phase behaviour for the loess is similar to that for the 41 ka analysis above. The phase is approximately constant back to 600 ka bp, but is changing linearly prior to this. Spectral analysis in Kukla et al. (1990) found no comparable drift in the 23 ka periodicity. Interpretation of the phase information here must be more cautious than that for the 41 ka wavelength as the amplitude is close to zero for large sections of this record.

3.6.5 ODP Site 677

This $\delta^{18}O$ record from Ocean Drilling Program core 677 is a marine record spanning the last 1.1 Ma ((Shackleton et al. 1990, and Section 1.5.1). It is felt to be of such high quality that it has been used in Shackleton et al. (1990) to recalibrate the magnetic reversal timescale by matching to orbital cycles. It should therefore represent an excellent data set for analysis by Complex Demodulation.

The spectral analysis of this data is shown in Figure 3.6. It has two main, strong periods at 100 ka and 41 ka, and a smaller peak around 23 ka.

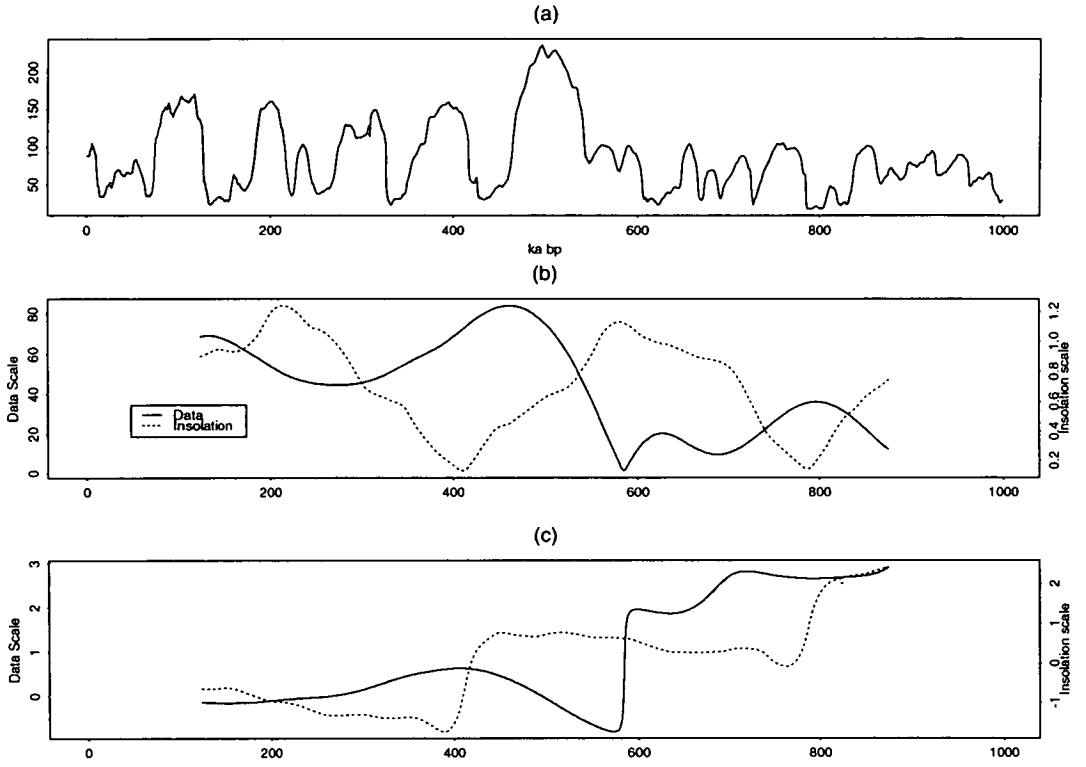

Figure 3.16. Complex Demodulation analysis of the 100 ka frequency in the Loess data: (a) the data; (b) amplitude estimates; and (c) phase estimates for the data and the insolation. There is no clear similarity between the Loess and insolation behaviour. See text for further details.

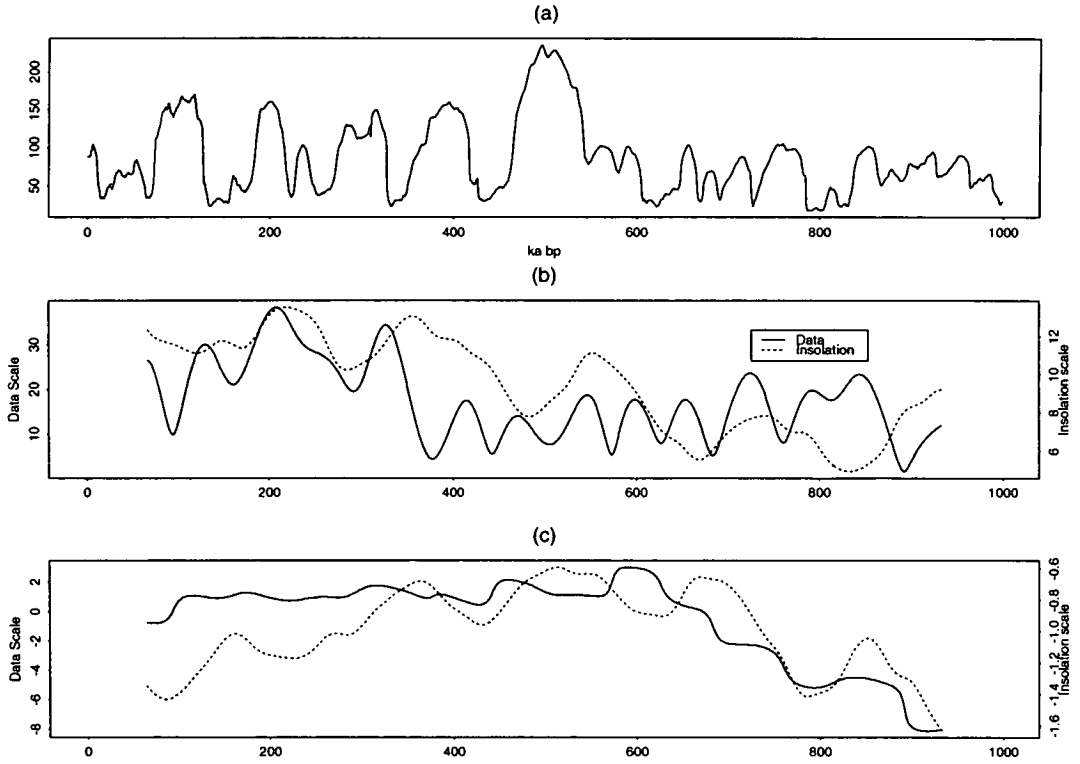

Figure 3.17. Complex Demodulation analysis of the 41 ka frequency in the Loess data: (a) the data; (b) amplitude estimates; and (c) phase estimates for the data and the insolation. The phase variations prior to 600 ka bp confirm the spectral character shown in Kukla et al. (1990). See text for further details.

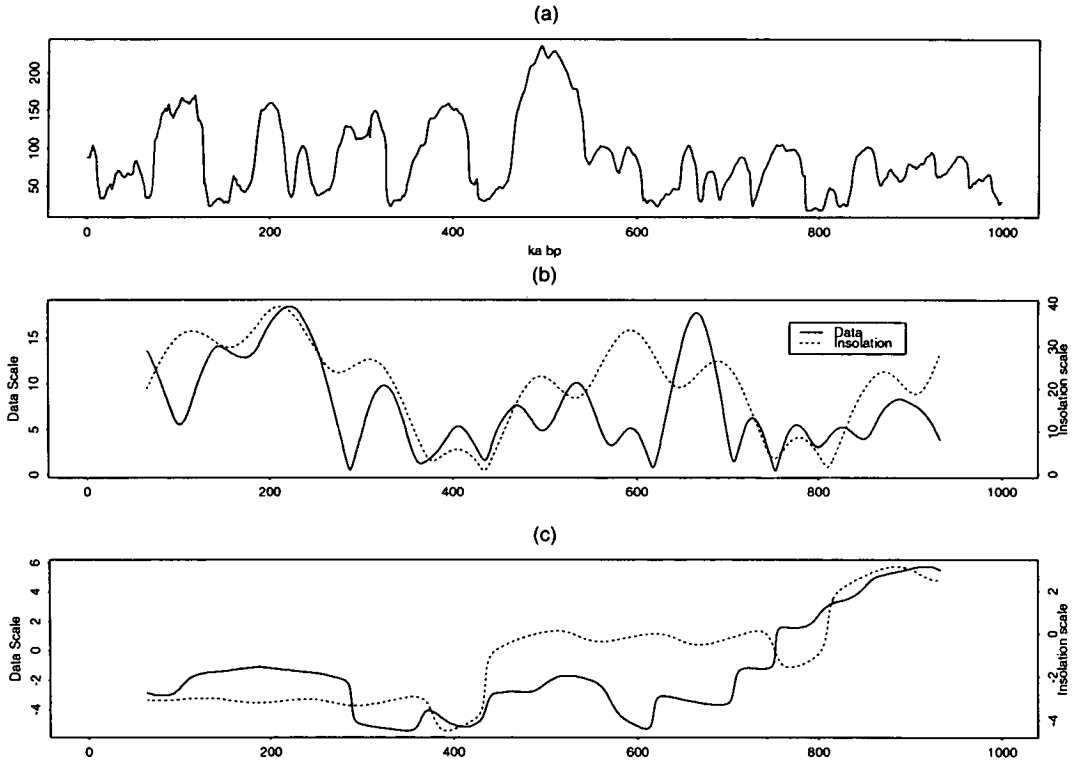

Figure 3.18. Complex Demodulation analysis of the 23 ka frequency in the Loess data: (a) the data; (b) amplitude estimates; and (c) phase estimates for the data and the insolation. There is a strong amplitude correspondence back to 500 ka bp. See text for further details.

100 ka cycle (Figure 3.19) As for the other time series, there is no obvious similarity between the isotope and the insolation analysis.

41 ka cycle (Figure 3.20) The amplitude behaviour shows no relationship between input and output, but again the periods of strong 41 ka signal in the data coincide with the deglaciations (around 130, 320, 420 and 620 ka bp). The phase behaviour matches well for the oldest section of the record (prior to 650 ka bp), and then there is a large step in the data phase, but the subsequent behaviour is still qualitatively similar.

23 ka cycle (Figure 3.21) Again the 23 ka cycle is at its weakest around 400 and 800 ka bp. However, beyond this the amplitude behaviour is not highly correlated. In addition, the phase result has no obvious structure.

These results are very disappointing, with little useful information from any of the analyses. Of the datasets analysed here, ODP 677 is the most detailed, containing more high-frequency information, but this has not benefited our analyses.

3.6.6 Devil's Hole Calcite Record

The Devil's Hole calcite record (Winograd et al. 1992) is an oxygen isotope record from Nevada, USA. It has been claimed that the timing of certain events in the Devil's Hole record, particularly the stage 5/6 and 7/8 deglaciations, contradict the Milankovitch hypothesis (Winograd et al. 1992, and Section 1.5.3). However, its overall similarity to the marine record is astounding given the different sources of the data. The spectral analysis in Figure 3.6 shows a dominant 100 ka period, a smaller 41 ka period, and no apparent peak at 23 or 19 ka.

100 ka cycle (Figure 3.22) The phase behaviour here is very similar to that for the SPECMAP record, and suggests a link between the 100 ka eccentricity cycle and that in the Devil's Hole record. However, note that the scale of the phase change in the input and output is different (6 radians in the data, 2.5 radians in the insolation).

41 ka cycle (Figure 3.23) There is some correspondence in the amplitudes between 150 and 370 ka bp, but the phase behaviour appears unrelated.

23 ka cycle (Figure 3.24) The amplitude variation would match the insolation well, were it not for the apparent disappearance of the 23 ka cycle

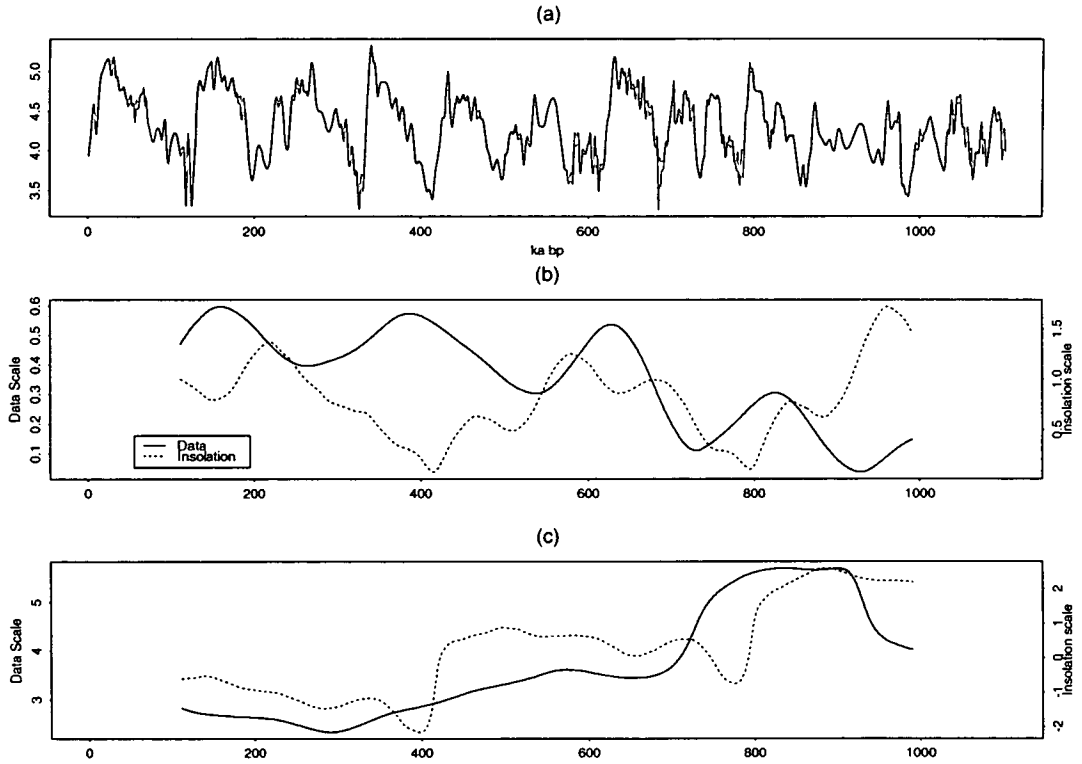

Figure 3.19. Complex Demodulation analysis of the 100 ka frequency in the ODP 677 data. (a) the data; (b) amplitude estimates; and (c) phase estimates for the data and the insolation. See text for further details.

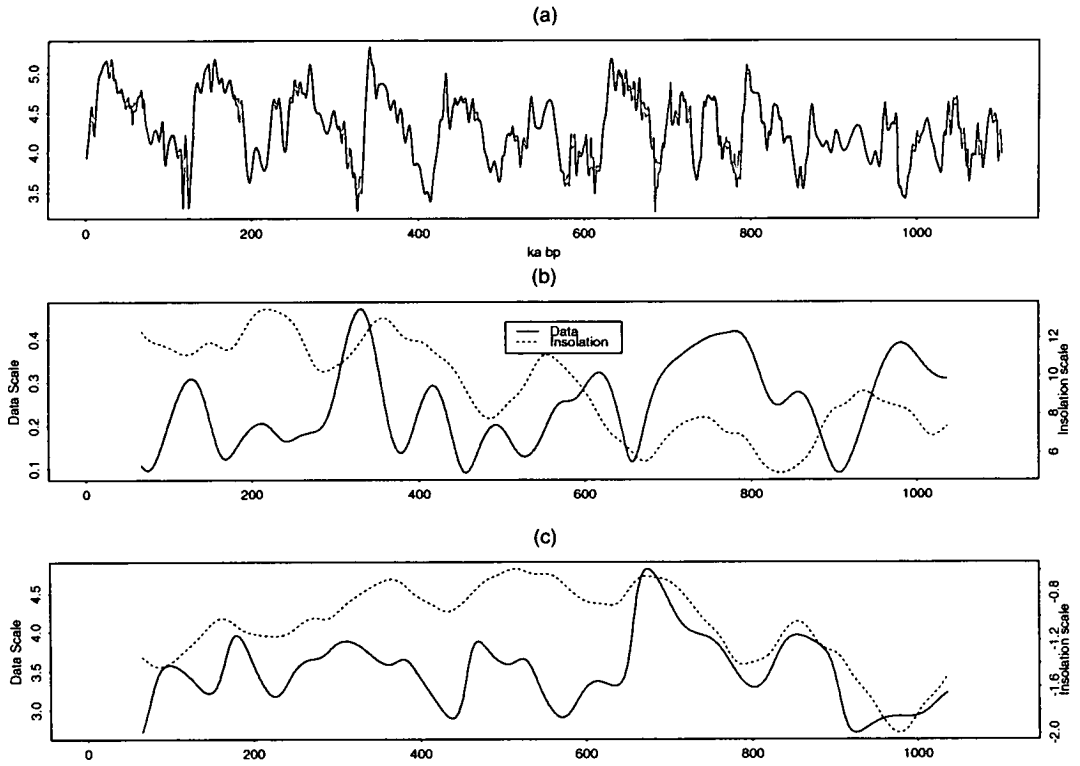

Figure 3.20. Complex Demodulation analysis of the 41 ka frequency in the ODP 677 data. (a) the data; (b) amplitude estimates; and (c) phase estimates for the data and the insolation. See text for further details.

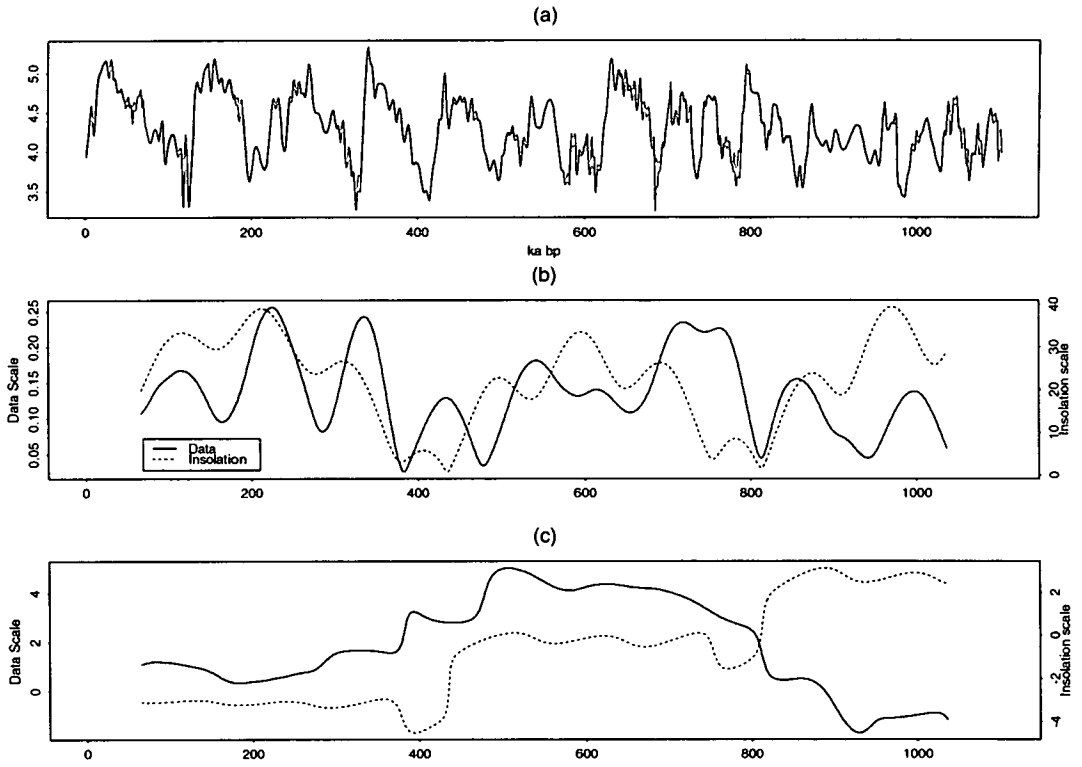

Figure 3.21. Complex Demodulation analysis of the 23 ka frequency in the ODP 677 data. (a) the data; (b) amplitude estimates; and (c) phase estimates for the data and the insolation. See text for further details.

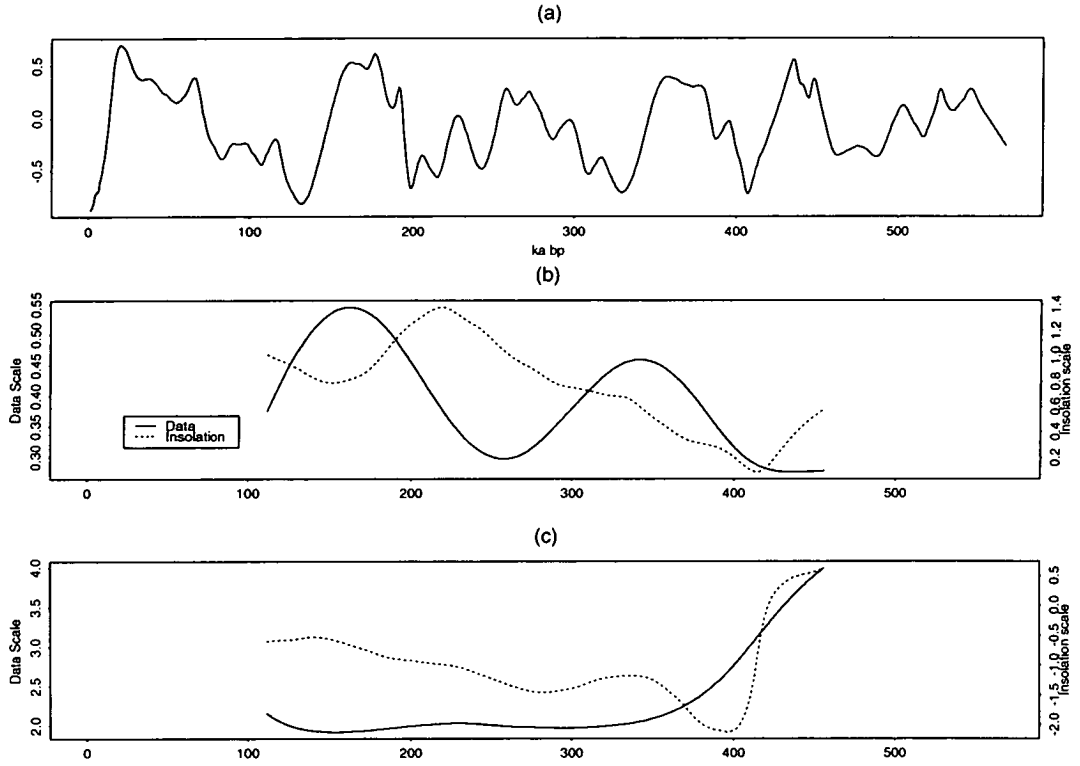

Figure 3.22. Complex Demodulation analysis of the 100 ka frequency in the Devil's Hole data. (a) the data; (b) amplitude estimates; and (c) phase estimates for the data and the insolation. See text for further details.

around about 150 ka bp. This coincides with an unusual peak in the phase plot. It should be noted that these anomalies occur at one of the contentious sections in the record, namely the transition from the glacial maximum into the Eemian interglacial. The peak in the phase may be due to the near disappearance of the cycle, or alternatively it could suggest an imperfection in the dating. The phase behaviour for the isotope record is fairly constant, apart from the spike and two step changes at 350 and 430 ka bp. It is interesting to note that these coincide with periods when the amplitude is low, and that that these also coincide with three major deglaciations.

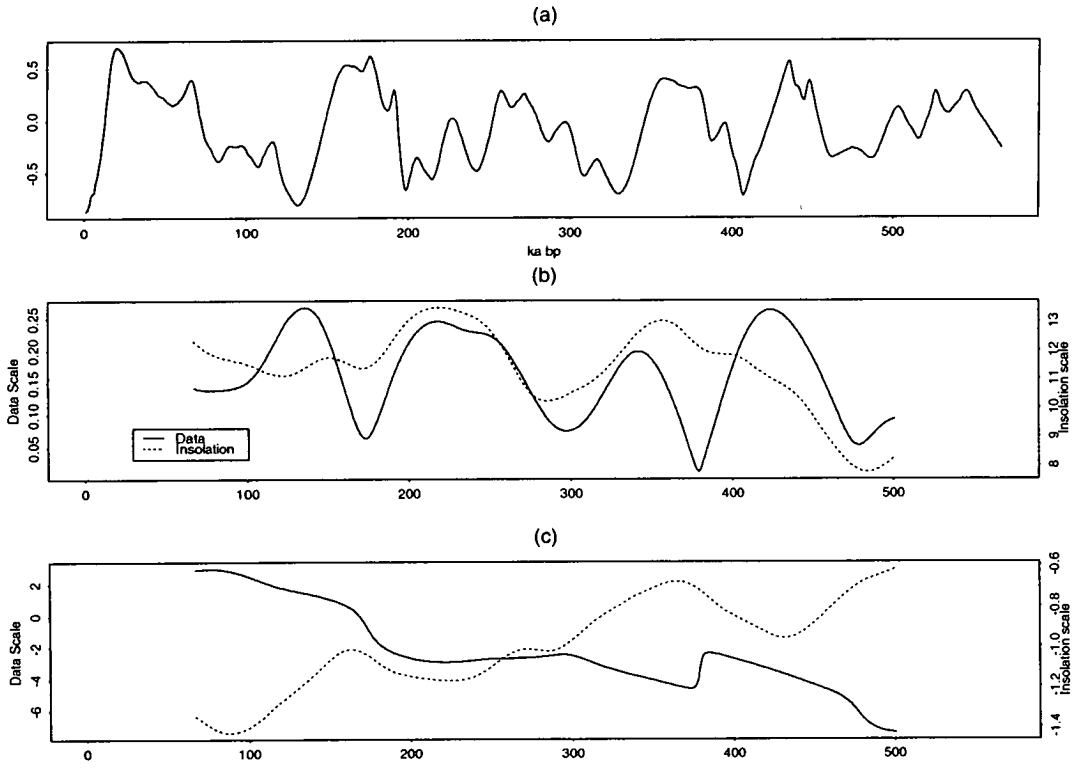

Figure 3.23. Complex Demodulation analysis of the 41 ka frequency in the Devil's Hole data. (a) the data; (b) amplitude estimates; and (c) phase estimates for the data and the insolation. See text for further details.

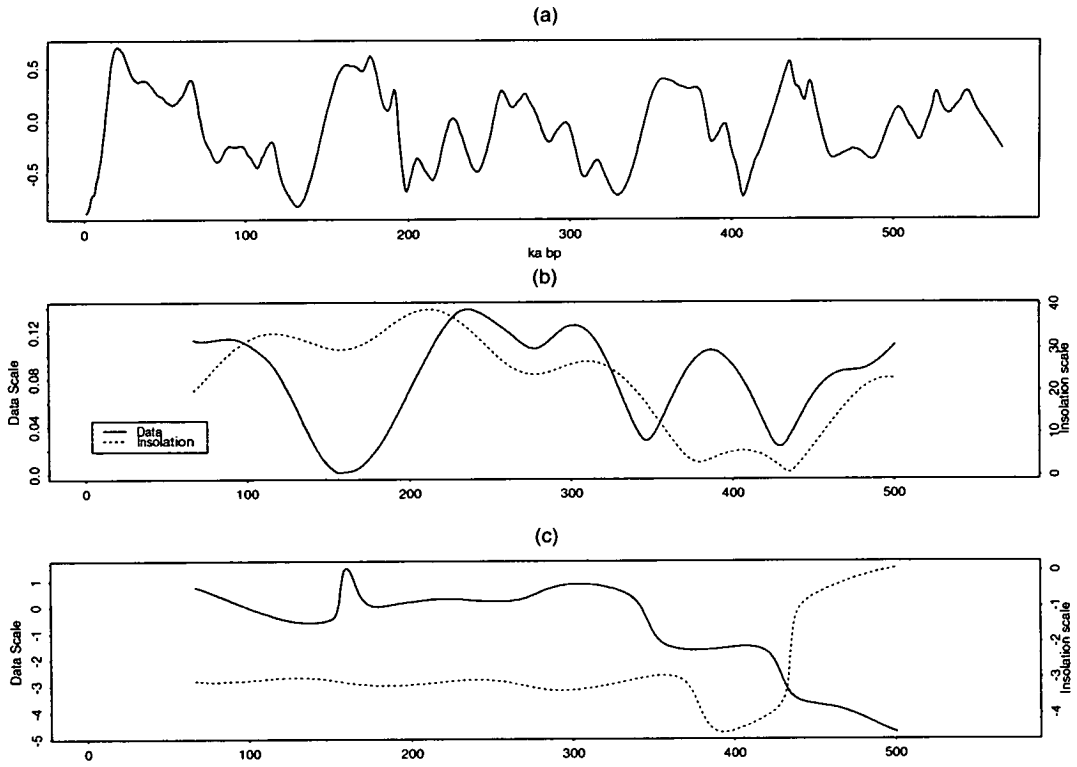

Figure 3.24. Complex Demodulation analysis of the 23 ka frequency in the Devil's Hole data. (a) the data; (b) amplitude estimates; and (c) phase estimates for the data and the insolation. See text for further details.

3.7 A Shorter Timescale Application

As a further illustration of the strength of Complex Demodulation, an analysis of a 70 year coral record (sampling interval 3 months) has been carried out. The data is an oxygen isotope record from Thailand (Tudhope et al. 1995). The initial aim of the analysis was to investigate the strengths of the quasi-biennial and El-Nino oscillations throughout the data. Figure 3.25 shows the data, and Figure 3.26 shows three different filter estimates of the amplitude of the annual cycle in the data. This graph contains all the information required. The coarsest filter shows a strong quasi-biennial oscillation in the early part of the record (1920-1942). The middle filter shows the strong El-Nino oscillation since 1950. The smoothest analysis shows an approximate 10-year cycle, and the correlation between this and the sunspot cycle is being investigated.

A benefit of having data with a strict annual component is that the phase behaviour of the annual cycle can yield useful information. In Figure 3.27 we see the phase of the annual cycle. The large change, beginning at 1939, sees a 2π change in phase over 2 years. This suggests a possible error in the dating at this point. The interpretation of the coral banding in this region is exceptionally difficult (A. Tudhope, *pers. comm.*), and Complex Demodulation has confirmed the need to re-analyse this segment of the coral.

3.8 Summary and Conclusions

Complex Demodulation is a simple and elegant method for extracting amplitude and phase information on the behaviour of apparent periods in a data set. It has been shown here to work well on both simple data and on more complex synthetic data. It has also proved fruitful in the analysis of real palaeoclimatic data. Complex Demodulation is ideal for this type of analysis, where we know the approximate frequencies present in the data (from spectral analysis and the orbital forcing assumption). In this situation we are therefore more concerned with the temporal variations in these periodicities. As further evidence for the potential of Complex Demodulation, Shackleton et al. (1995) have recently highlighted the limitations of cross-spectral analysis (specifically coherence) for analysing the amplitude modulation of the precession component in the climate record, a task which Complex Demodulation is extremely well suited to.

For the four long climatic records analysed the results raised some interesting

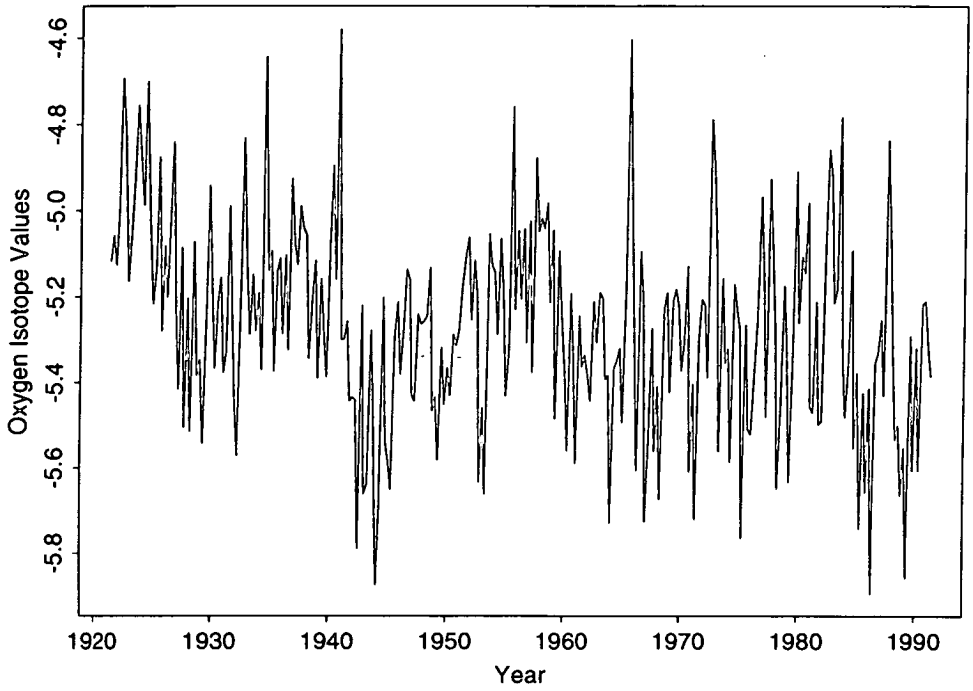

Figure 3.25. Coral oxygen isotope data from Thailand.

points.

Firstly, for the SPECMAP record analysis, there is some evidence for phase similarities between the 100 ka cycle in the data and that in the eccentricity variations. The amplitude variation of the 23 ka periodicity in both the insolation and the climatic data show similar variations. Unlike coincident spectral peaks, this could not be dismissed as a side effect of the "tuning" dating procedure, and therefore is supporting evidence for the Milankovitch Theory. Also, the phase behaviour of the SPECMAP 41 ka cycle is evidence of the error in applying the dating methodology.

The phase behaviour of the 100 ka cycle in the Loess data looks similar to that for eccentricity, apart from the step changes during periods of very low amplitude. As with SPECMAP, there is similarity in the amplitude of the 23 ka period. Analysis of the 41 ka cycle confirms the MEM spectral analysis results of Kukla et al. (1990), implying a change in the periodicity prior to 600 ka bp.

The ODP 677 data gave surprisingly poor results. The only real evidence to support the orbital theory is the times of strong 41 ka variation being associated with deglaciations.

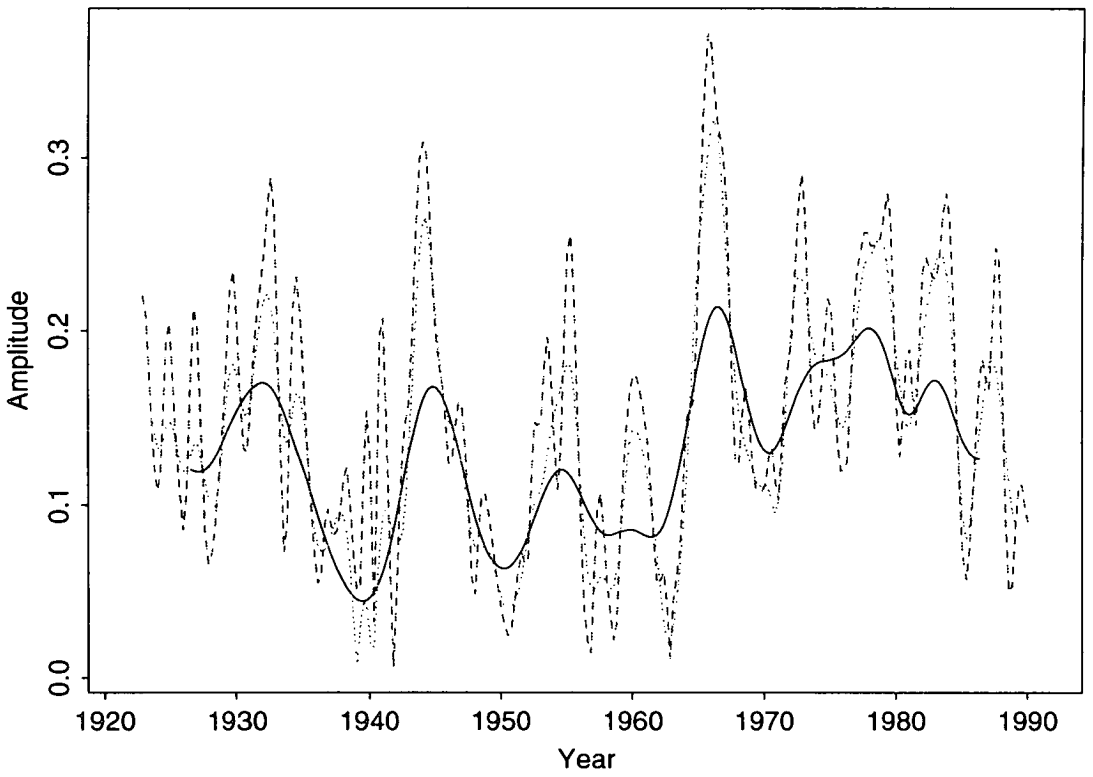

Figure 3.26. Three different filter estimates of the amplitude of the annual cycle in the coral data. These in turn illustrate the strong quasi-biennial oscillation in the early part of the record, the strong El-Nino oscillations sice 1950, and the smothest estimate displays an approximate 10 year cycle, and a possible correspondence with the 10 year sunspot cycles.

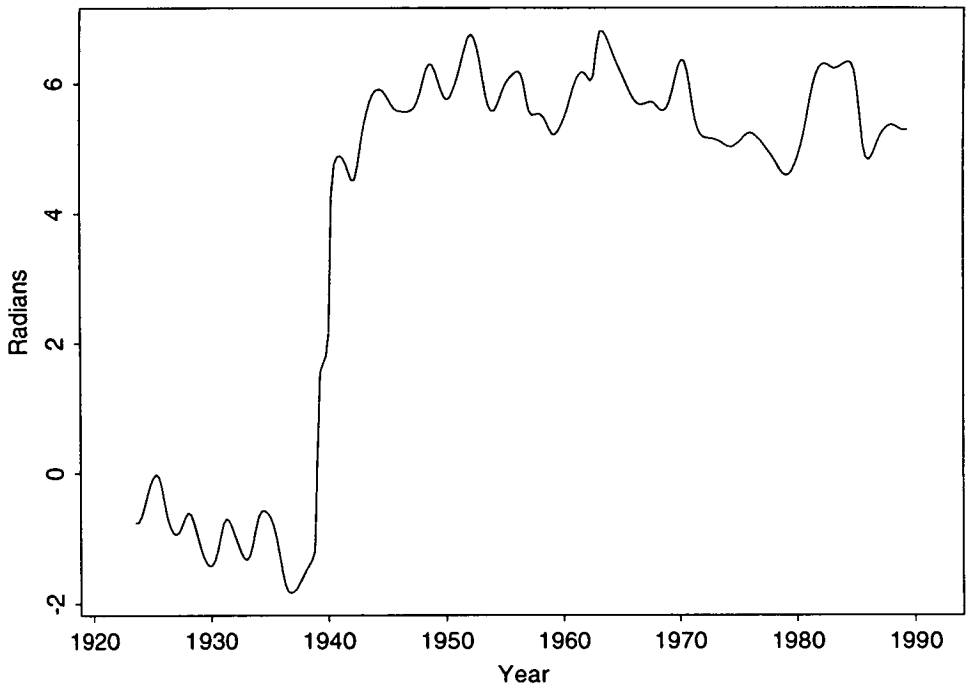

Figure 3.27. The estimated phase of the coral annual cycle, showing the phase change due to the dating error around 1940.

The Devil's Hole data, like SPECMAP, implied a connection between the eccentricity phase and the phase of the Earth's 100 ka period. Even more interesting are the results for the 23 ka cycle. These suggest that there may be a problem with the dating during deglaciations, particularly during the stage 6/5 transition. This may have important implications, as the earlier timing of this deglaciation has been interpreted as preceeding the insolation pulse, and therefore contrary to the Milankovitch theory.

In general, the amplitude behaviour is easier to interpret than the phase. Care must be taken with phase changes, and in particular their scale, as a phase change of 2π is not necessarily a real phase change. In addition the amplitude and phase results are often linked. This is particularly true when the amplitude is near zero, as this implies the disappearance of that particular frequency and the phase results have little meaning.

When applied to annual data, the phase results can help to illustrate deficencies in the time scale, highlighted by abnormalities in the phase behaviour of the annual cycle.

We have shown that Complex Demodulation is useful in its own right, and can also add further quantitative information to a bandpass filter analysis.

Chapter 4

Linear Modelling of Palaeoclimatic Data

4.1 Introduction

It is widely acknowledged that linear modelling of the climate will never fully characterise the features seen during the Quaternary. However, while the magnitudes of certain events are evidently the result of non-linear behaviour, the general shape and features can be very well modelled using the calculated orbital and insolation variations. Therefore, linear models are not only an essential first step, they also have strong individual merit. In addition, linear modelling is an essential first step test for nonlinearity, as succesful linear modelling is evidence against the process of interest being nonlinear.

Chapter 2 has described the previous attempts at linear modelling of past climates. In this chapter we explore for ourselves the benefits and limitations of such analysis. Some of the work here is extremely simple, yet is a useful foundation for subsequent chapters.

There are four main sections to this chapter:

- Linear regression modelling of the SPECMAP record with an additional autoregressive term;
- Linear regression modelling of temperature data from France, including use of the SPECMAP record as a regression variable to provide the backbone for hindcasting (extending the time series by extension backwards in time) the shorter French records;

- Linear transforms of the SPECMAP record and the French hindcasts to provide hindcasts of the climatic driving function of a North-West European Ice-sheet model;
- Linear transformation of the French temperature data as a means of constructing a surrogate NW England record.

4.2 SPECMAP Modelling

This section deals with attempts to model the SPECMAP curve as a combination of the orbital parameters, the insolation and an autoregressive term. This work was based on that in Kukla et al. (1981) (Astronomical Climate Index Model: ACLIN) and Berger et al. (1981) (Insolation Climate Index Model: INCLIN). These methods are both discussed in Section 2.7.

In Kukla et al. (1981) they utilise the fact that high obliquity, high eccentricity and autumn perihelion correlate with periods of warm climate. They therefore choose the following transformations of the three orbital parameters:

$$|\frac{\omega - 180}{90}| \qquad \epsilon - 22 \qquad e^2$$

where ω is the longitude of the perihelion, ϵ is the obliquity, and e is the eccentricity. They also lagged the obliquity term by 5000 to 6000 years, accounting for some of the memory in the process.

The INCLIN model of Berger et al. (1981) is a linear combination of six insolation series for different latitudes and seasons, with the addition of an autoregressive term of lag 3000 years. This was used to model past oxygen isotope variations.

The idea is to combine a regression model with an additional lagged term as an input. The lagged term will account for some of the memory in the climate system. Following on from Berger et al. (1981), we choose the SPECMAP value at lag 3000 years as the lagged term. Obviously, due to the smooth nature of the record, this term will then have a regression coefficient near to unity. It is hoped that the other regression variables will then impose on this the correct evolution of the climate system.

Linear regression was carried out with SPECMAP as the regression variable, and the following five explanatory variables:

	Constant	x_1	x_2	x_3	x_4	x_5
SE	0.25	0.022	17.08	0.019	0.00061	0.014
t-ratio	22.4	4.6	2.6	1.9	21.1	67.2

Table 4.1. Standard errors and t-ratio statistics of the regression formula in Equation 4.1.

- x_1: the modified precession variable from ACLIN
- x_2: the modified obliquity variable from ACLIN, lagged 6 ka
- x_3: the modified eccentricity variable from ACLIN
- x_4: the insolation for July at latitude 65° North.
- x_5: the SPECMAP value of 3000 years ago

This regression was carried out for various time intervals of the past record, and as expected reproduces the record well due to the autoregressive term (when the actual SPECMAP values are used). However, the test of this model is to predict a past timeslot for which SPECMAP is known, using the model's own predictions as the autoregressive component.

We discuss here the regression carried out for the time period 100-500 ka bp. The SPECMAP record is too long to attempt to model as a whole, particularly due to the different behaviour in the early part of the record (the less obvious glacial cycle, and smaller magnitude changes). We therefore chose this 400 ka period, and can use the last 100 ka to test the model. The regression model found is

$$y = 5.61 + 0.103x_1 - 0.035x_2 - 43.9x_3 - 0.0128x_4 + 0.934x_5 \qquad (4.1)$$

with an R^2 value of 94.5%. The standard errors and t-ratio statistics of each variable are shown in Table 4.2. All variables were significant when the backwards elimination technique was applied.

We are interested in the models ability to reproduce the last 100 ka, using the model's own estimate of the SPECMAP value at time $t-3$. Figure 4.1 shows three predictions of the last glacial cycle, using three different starting points: a glacial maximum; glacial to interglacial transition; and an interglacial. We observe that the starting point has little effect on the long term value of the prediction. Also, none of the models capture the full scale of the climatic variation. However, there is a strong similarity between the features in our prediction and the corresponding

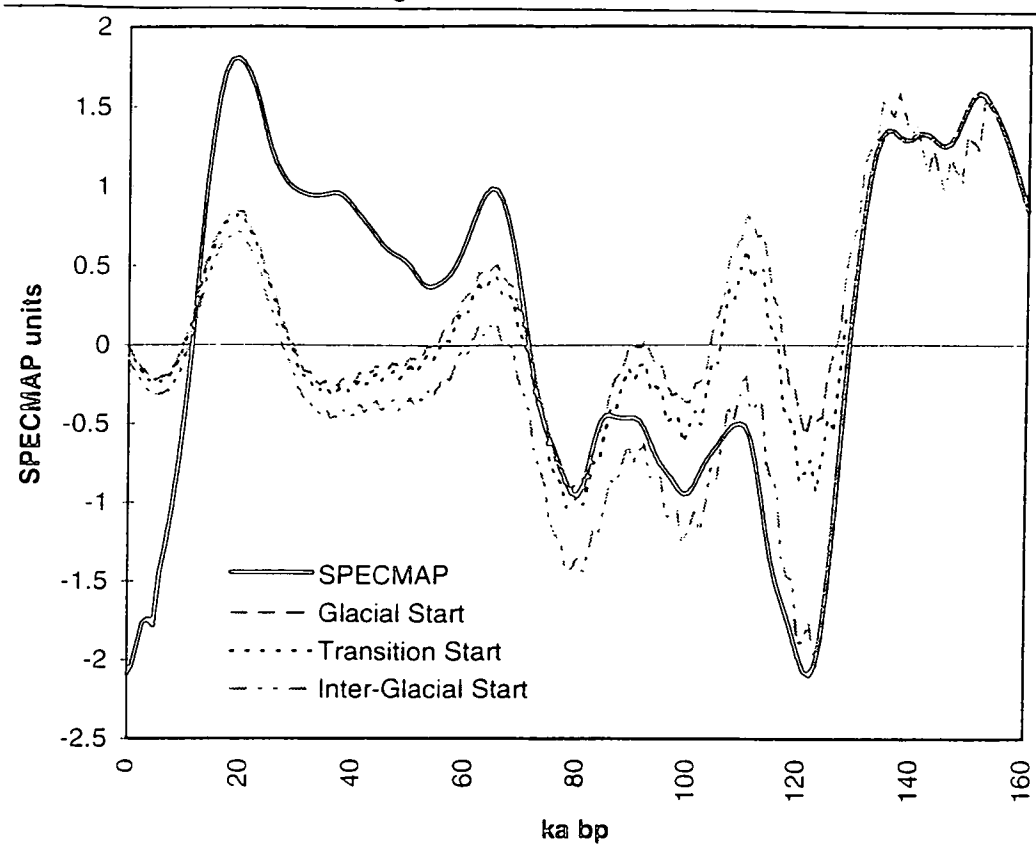

Figure 4.1. The three predictions of the SPECMAP record using Equation 4.1. Despite the three different starting points for the predictions (glacial, interglacial, and during the transition between these), none manage to capture the scale of variation in the SPECMAP record. However, they do predict the SPECMAP turning points well.

climatic behaviour. This is strong evidence for the dependence of the Earth's climate on the orbital and insolation variations, although there must be other components or relationships which account for the deficiencies in this model. In Chapter 5 we will go on to investigate some nonlinear regression techniques in an attempt to ascertain whether this "missing" element can be accounted for as a nonlinear response to the orbital forcing.

4.3 Hindcasting the French Temperature Records

Temperature data is available from three locations in France, namely Grand Pile, Lac du Bouchet (Plateau du Deves), and Les Echets (Section 1.5.4). Each record covers approximately present day back to 140 ka bp at 1000 year intervals. The temperature data is in 0.1 deg. C anomalies from present day. All three sites appear to have behaved similarly showing the Younger-Dryas, the last glaciation,

and the substages of the Eemian interglacial. The records stop at approximately the maximum of the preceeding ice age.

There are two main motivating factors behind this work. The first is to use the SPECMAP global record the extend the NW European continental record back to 600 ka bp. This can then be used as input to a Fennoscandian ice sheet model, and its output compared with the palaeoglacial evidence. Secondly, it is hoped to shed some light on the problem of the Holsteinian interglacial in Europe. In Europe the climate record is only fixed back to the Eemian interglacial, approx 120 ka bp. Many records show another major warm period prior to this, called the Holsteinian interglacial. However it is only known that this interglacial occured between approximately 200 and 400 ka bp (i.e. it is not known, in a global sense, if it corresponds to the 2nd, 3rd or 4th last interglacial). If a consistently stronger warm period was predicted by all three pollen record extrapolations then this could be used as evidence for the timing of the Holsteinian.

In addition to the three site specific records, we have constructed a composite French temperature record. The three records were normalised by removal of the mean and division by their standard deviation. These normalised records were then averaged to give a stacked French temperature record. All the records are shown in Figure 1.13.

We now have the benefit of being able to use the SPECMAP record amongst the following regression variables:

- x_1: the modified precession variable from ACLIN;
- x_2: the modified obliquity variable from ACLIN, lagged 6 ka;
- x_3: the modified eccentricity variable from ACLIN;
- x_4: the insolation for July at latitude 65° North;
- x_5: the SPECMAP value at time t;
- x_6: the SPECMAP value at time t-1;
- x_7: the SPECMAP value at time t-2.

We include the two lagged SPECMAP terms to account for any possible time lag between the records.

The t-ratio test was employed in backwards elimination to remove insignificant regression variables. This resulted in the parameter estimates shown in Table 4.3.

Regn. Variable	Grand Pile	Bouchet	Les Echets	Composite
Precession	2.29	26.6	14.8	0.258
Obliquity	-	14.2	-	0.125
Eccentricity	-5832	25247	9013	159
July 65N	-0.354	-0.551	-0.576	-0.00394
SPECMAP	-9.6	-124	-49.4	-0.589
SPEC lag 1	-36.6	113	-	-
SPEC lag 2	24.2	-	28.8	-
Constant	107	199	163	1.13
R^2	60.5	68.1	69	74.2

Table 4.2. Regression parameter estimates for the French temperature records.

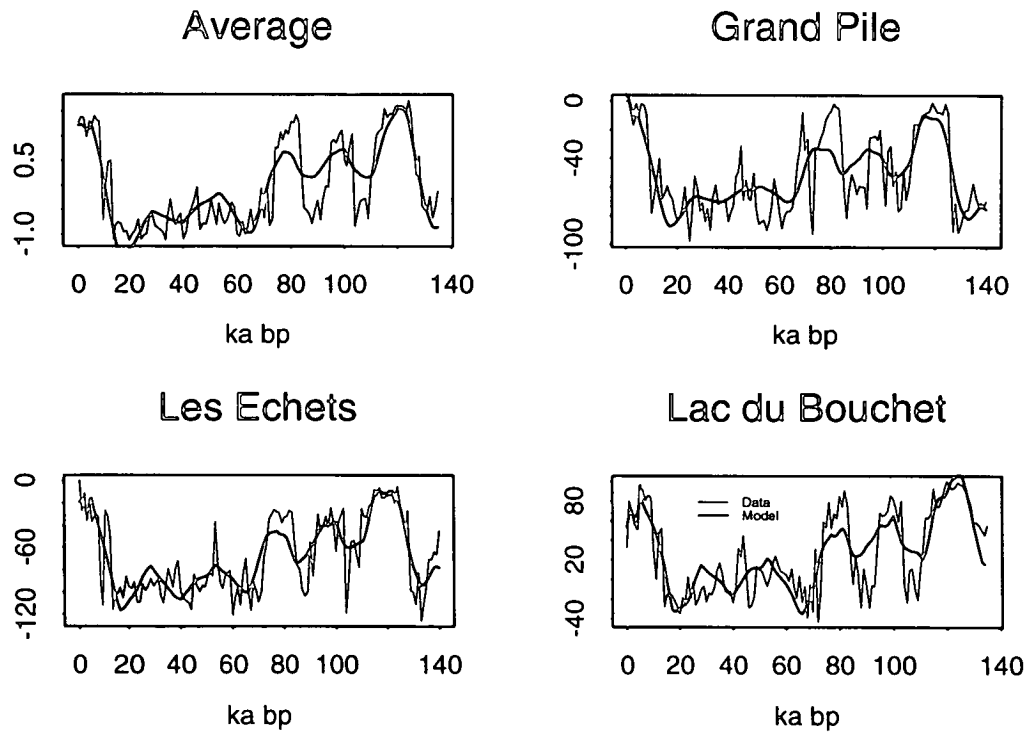

Figure 4.2. The fits of the four French temperature records. All the models work well, with the exception of during MIS 5a-5d, where the models cannot capture the full scale of the temperature variations.

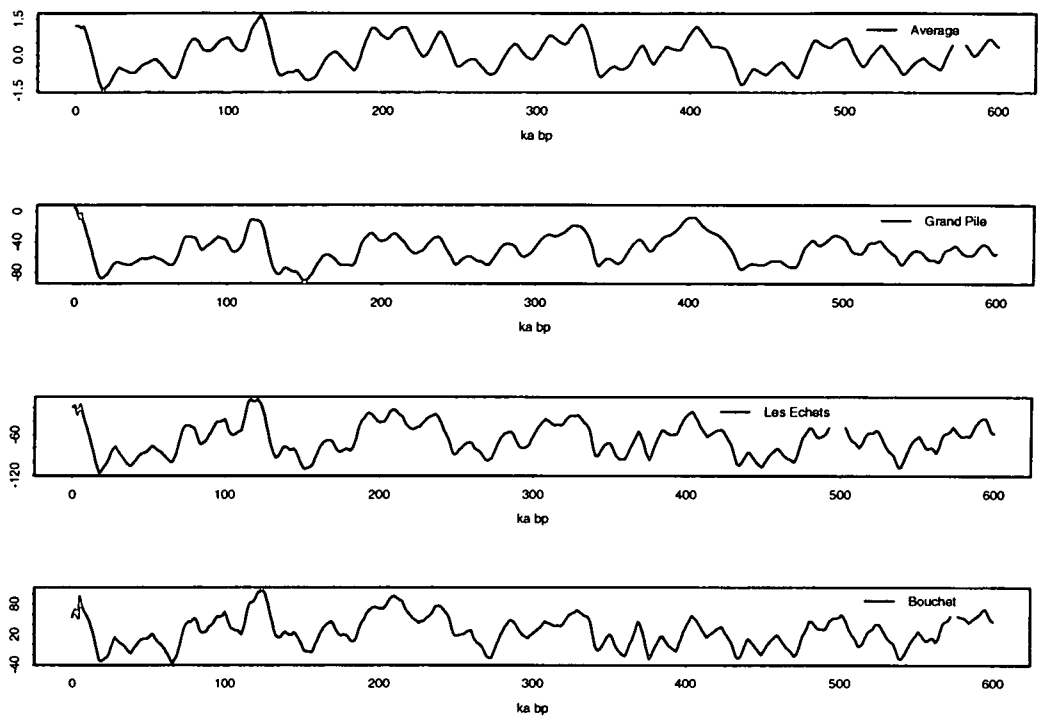

Figure 4.3. The hindcasts of the four temperature records back to 600 ka bp.

The model fits are shown in Figure 4.2. The model is dominated by the SPECMAP terms, unsurprising given the strong similarity between the records. The main problem arises in the period 70-110 ka bp (MIS 5a-5d). In this period the temperature data fluctuates between full glacial and inter-glacial values, whilst the SPECMAP record (and other global records in general) indicates a more restricted fluctuation in the climate. We are therefore unable to model the full scale of the temperature variations in this period, but we can reproduce the smooth component of the other features in the temperature data.

We can then use the regression equations to hindcast the four records back to 600 ka bp. These are shown in Figure 4.3. These are all broadly similar in behaviour. There is some evidence for the stronger effect of obliquity and precession in the Lac du Bouchet record, as suggested by the regression coefficients in Table 4.3. With regards to the Holsteinian, we can draw no postive conclusion: the Grand Pile record suggests that the interglacial at 400 ka bp was the strongest, Bouchet has the 200 ka bp interglacial as the strongest, and Les Echets has no strong individual period.

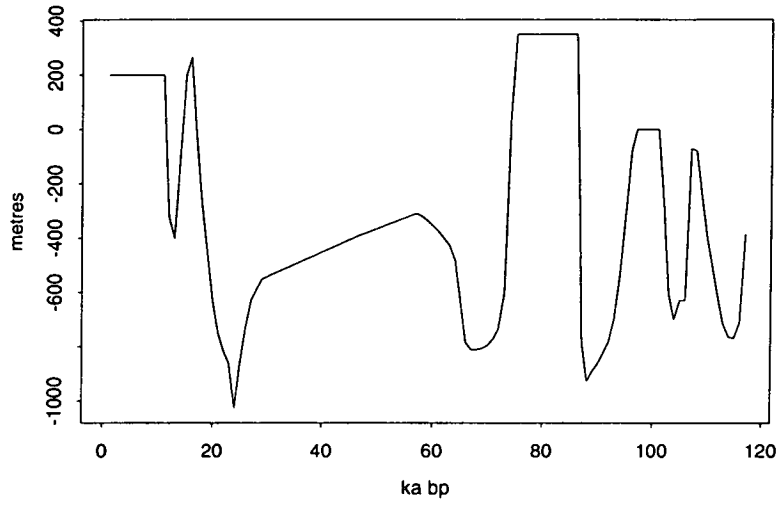

Figure 4.4. The ELA reconstruction for the last 120 ka (Boulton et al. 1995).

4.4 Hindcasting the Ice Sheet Driving Function

Glaciologists have constructed a computer model of the Fennoscandian ice sheet, covering the glaciated areas of NW Europe (Boulton and Payne 1994, Boulton et al. 1995, Boulton et al. 1996). This takes as input an estimate of the Equilibrium Line Altitude (ELA). The ELA is the altitude at which the mass balance of the ice sheet is zero i.e. at this altitude the summer snow melt equals the winter accumulation, and at higher altitudes there is net ice accumulation, at lower altitudes there is a net loss. The ELA is a method for encapsulating all the relevant climatic information in a single forcing time series.

A plot of the ELA reconstruction for the last 120 ka (Boulton et al. 1995) is shown in Figure 4.4. This has been constructed so that the resulting ice sheet output most closely matches the geological evidence. Like the French temperature data, the ELA has strong fluctuations during MIS 5. It also has a relatively strong MIS 3 (30-60 ka bp). We aim to model this curve via a simple transformation of the SPECMAP record.

The most problematic area is MIS 5a-5d, where we have strong fluctuations in the ELA record, but not in the SPECMAP record. During this time SPECMAP has an average value of -0.75. We therefore take this value as being the threshold value in the SPECMAP record. We therefore create a glacial/non-glacial indicator variable. This takes values of ± 2 according to whether SPECMAP is above

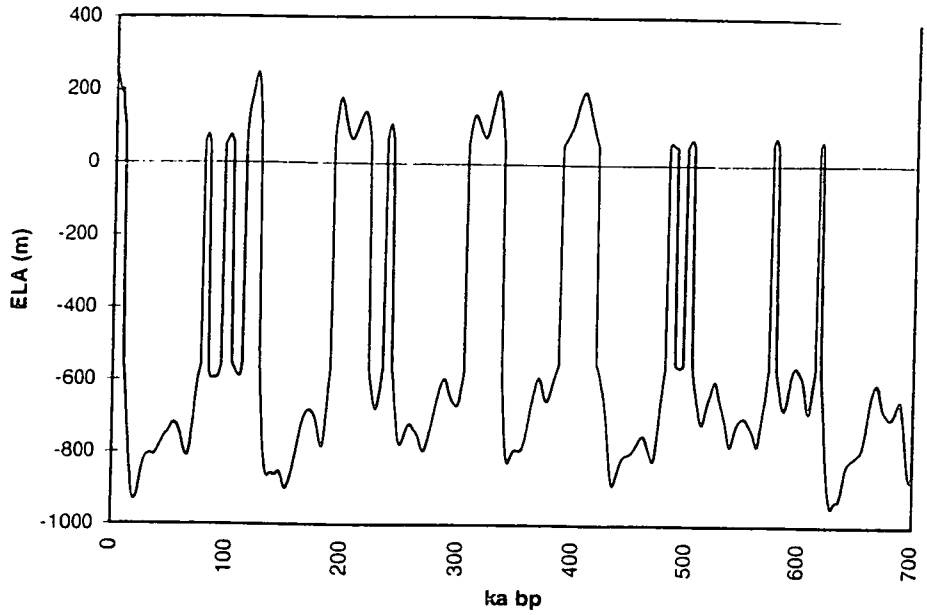

Figure 4.5. The hindcast of the ELA function for the last 700 ka, including the the rapid switches in ELA values during MIS 5 and older periods.

or below -0.75. We then averaged this binary time series with the SPECMAP record, thus increasing the variation during stage 5, but without changing the extreme values of the data. We then apply a linear transform to this series to assign a realistic y-axis scale.

Our final model is

$$ELA = -364.8 - 298.6 \times \begin{cases} Average(SPECMAP, 2) & : \quad SPECMAP > -0.75 \\ Average(SPECMAP, -2) & : \quad SPECMAP \leq -0.75 \end{cases} \tag{4.2}$$

The resultant ELA estimate is shown in Figure 4.5. This has the large, rapid fluctuations in stage 5 and realistic estimates for the glacial and interglacial altitudes. This ELA was then used as input to the ice sheet model, and produced the ice volume record shown in Figure 4.6. This reconstruction can now be compared with the available geological evidence in an attempt to verify its representation of ice sheet variations.

4.5 NW England Temperature Surrogate

As climate records from around the world grow longer and more accurate there is still a relative shortage of information available for mainland Britain. This is a consequence of the extensive glaciations that have occurred throughout a large

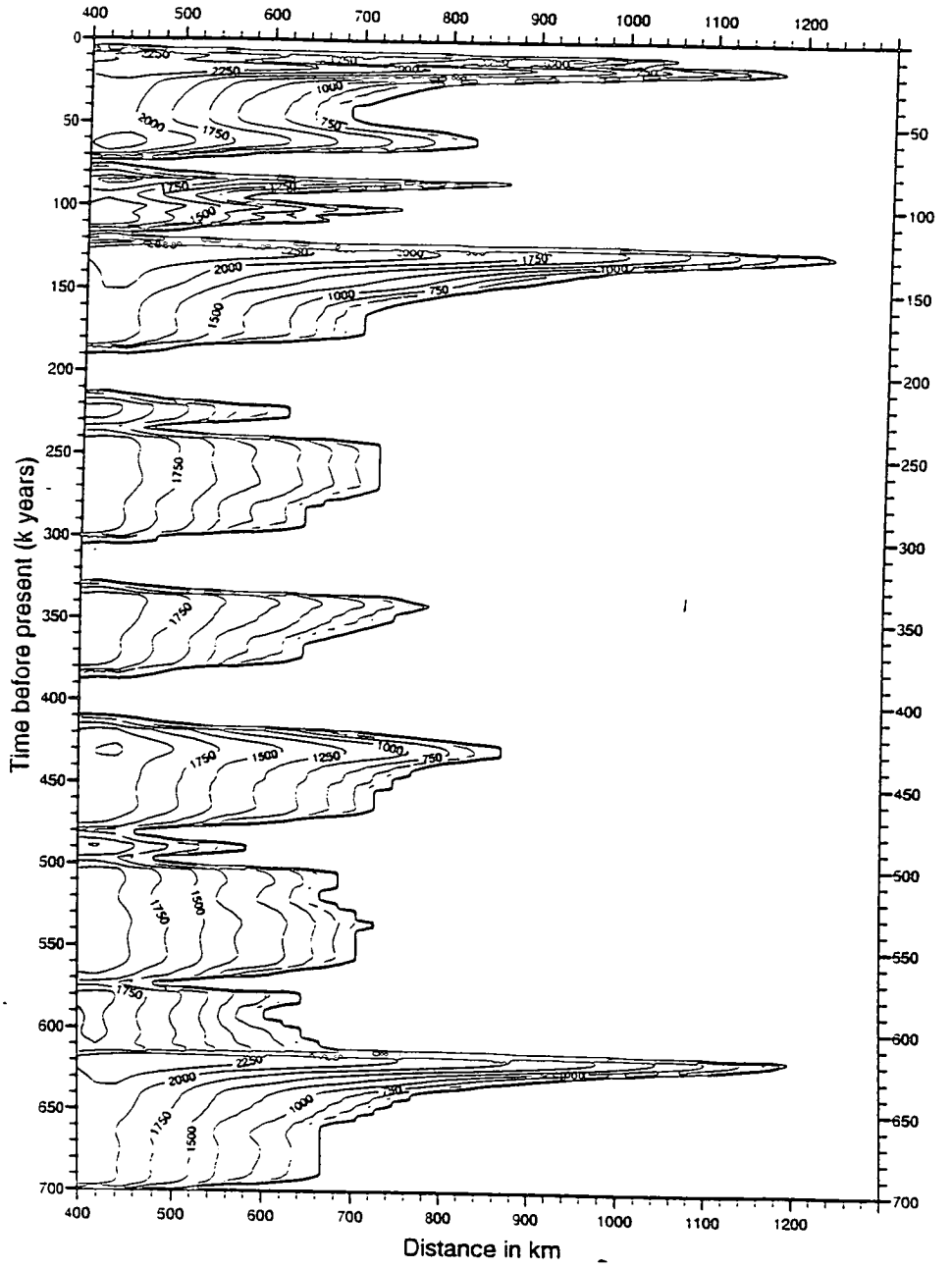

Figure 4.6. The output of the ice sheet model using the ELA estimate in Figure 4.5 as input.

portion of the country during the Quaternary period. Thus, it is impossible to use the usual terrestrial records, such as pollen in France or loess in China, to reconstruct the recent climate. In addition, the data which are available are often in the form of point estimates, not a continuous time series. There is therefore much to be gained from utilising this fragmentary data to produce a continuous record. In this section, we reconstruct the temperature fluctuations in N.W. England for the last 140 ka.

The most detailed information for Britain comes from the analysis of the geographical distribution of Coleoptera fossils (Coope 1977). However, this only gives a detailed record back to the Last Glacial Maximum (LGM) and then limited information back to 40 ka bp. Therefore, to construct a longer climate record it will be necessary to piece together the information available , whilst linking it to a longer climate record. We have used the closest, most detailed, terrestrial record available, which is the temperature data reconstructed from pollen assemblages at three locations in France (Section 1.5.4). In order to capture the regional as opposed to localised variations, we will use the composite record shown in Figure 1.13.

The assumption is made that the pattern and timing of climatic changes in N.W. England and France will be similar. The problem then is to deduce the differences in the scale of variation, and the absolute values in England. To achieve this it is necessary to compare the climatic behaviour through the recent past. This involves the progression through the LGM, the subsequent deglaciation, the Younger-Dryas cooling (YD), and the Holocene. We can then transform the French record to model the known behaviour in N.W. England. The information available is predominantly for maximum (July) and minimum (January) temperatures. We will therefore reconstruct the July and January records and then estimate the annual temperature as the average of these. This estimate of the annual temperature will be reasonable, although it may slightly overestimate the severity of the cold during glacial times. Table 4.5 shows the data available for the five main climatic events.

July (Max) For the French record, the temperature difference between the Holocene max. and YD min. is 7°, and with the LGM another 2° colder. This matches exactly with the Sellafield anomalies. Therefore, the scale of variation is the same, so we need only alter the absolute values. Thus, the July curve is the base record moved to match the present day temperature of 14.4°. The one discrepancy is at the pre YD maximum. In Britain

Event	January	Annual	July
Present Day	2.8^1	8.5^1	14.4^1
Holocene Max	3^2	-	15^3
YD Min	-15^2	$< 0^4$	8^3
Pre YD Max	-2^2	-	15^3
LGM Min	-25^2	$< 0^4$	6^2

Table 4.3. The available NW England temperature data, and references. References are (1) *Agricultural Climate of England and Wales* (1984) (2) Briffa et al. (n.d.) (3) Coope (1977) (4) Goodess et al. (1992).

this attained full Holocene temperature, but not in our composite French record.

January (Min) Winter temperatures are expected to show larger variation than summer or annual, so we therefore expect to have to scale the French record. In the Sellafield region the YD minimum was 18° cooler than present day, which is three times the magnitude of the change in France. We therefore scale the French data by a factor of three, and then subtract 21 to give the correct present day temperature. As a check, this gives a pre YD maximum of −2° and LGM of −21°, which compare very well with the known values of −2° and −25°.

Annual (Max and Min Average) The annual curve is then estimated as the average of the January and July curves. We can then compare this with the limited data available. The average gives the present day temperature as 8.8° which compares excellently with the true value of 8.5°. In addition, we know that the temperature during the YD and at the LGM were below zero, and this average has these properties.

The resulting curves are shown in Figure 4.7. Thus, by combining the fragmentary record from N.W. England with the continuous, terrestrial record from France, we have constructed an estimate of the temporal evolution of temperatures in the region over the last 140 ka.

4.6 Summary and Conclusions

All the techniques used in this chapter are extremely simple. However, there are several important conclusions which we can draw. Most importantly, Section 4.2

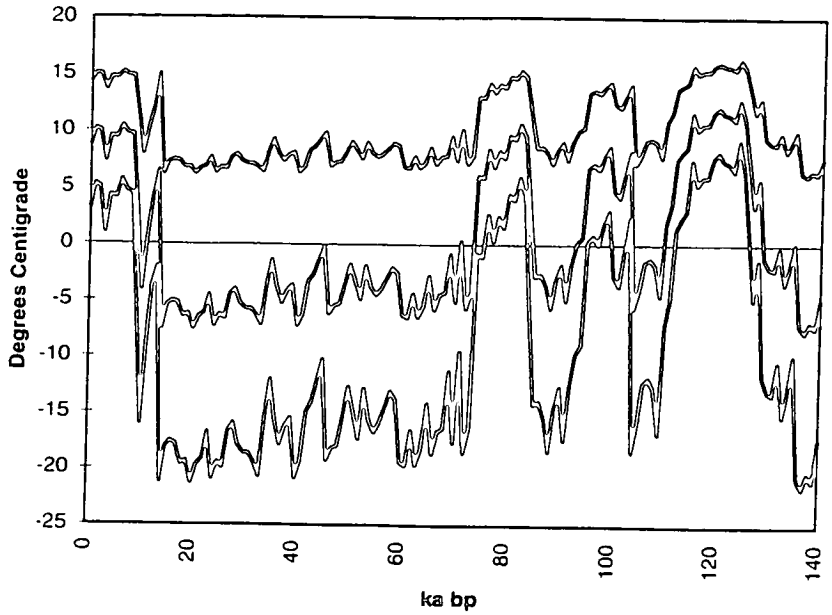

Figure 4.7. The three temperature time series for the North West of England, representing the January, July, and Average (Annual) variations.

has highlighted the relationship between orbital variations and climate through our ability to reproduce the general features of the SPECMAP record. We will go on in Chapter 5 to extend this in an attempt to capture the scale of the variations aswell as the features.

The hindcasting of the French temperature records was a useful exercise, though it could make no indication as to the temporal location of the European Holsteinian interglacial.

The threshold model of the SPECMAP data allowed us to produce a realistic ELA record back to 700 ka bp and to use this to repoduce the glacial history of NW Europe during this time. This model is technically nonlinear, but is included in this chapter due to its relative simplicity.

Comparison of the French temperatures with the fragmentary data for NW England has confirmed that the past behaviour has been very similar in these two regions, with a simple linear transformation sufficing for modification of the French data to represent the palaeotemperature variations in N.W. England during the last 140 ka.

Obviously, all these reconstructions must be continually compared with new geological evidence as it becomes available.

Chapter 5

Nonlinear Regression Modelling

5.1 Aim

Linear regression modelling (Chapter 4) has shown that it is possible, using only Milankovitch variations, to replicate the low frequency (periods $> 10^4$ ka) features of past climate, but not the scale of the climatic variation. This suggest possible non-linearity in the system's response to orbital forcing. There are regression techniques now available which can attempt to characterise this non-linearity by removing the restriction of a linear relationship between the inputs and the output. Here we study two of these methods, and determine their potential benefits for:

- gaining information on the influence of each orbital variable;
- modelling of the past climate and prediction of the future.

5.2 Introduction

Previous statistical attempts to model and predict climate on the Milankovitch timescale have been predominantly linear (Berger, Gallee and Melice 1991, and Chapter 4). They utilised the statistical techniques of Linear Regression and Autoregressive Integrated Moving Average (ARIMA) Models. As shown in Chapter 4, these can succesfully model the turning points of past climate, but their inability to reproduce the magnitude of warm and cold periods and the rapidity of the deglaciations, means that they are not capturing the climatic behaviour correctly. The techniques in this chapter will allow us to address these problems.

The causes of these rapid deglaciations are not fully understood. Theoretical explanations are diverse, and include (for example) ice sheet dynamic behaviour (Pollard 1982), self-sustained oscillations with forced/free Carbon Dioxide variations (Saltzman and Maasch 1990), and direct non-linear amplification of the eccentricity related insolation changes (Hays et al. 1976). More recently Imbrie et al. (1992) and Imbrie et al. (1993) investigated the linear and nonlinear response of the Earth's climate system to the insolation cycles. They concluded that the obliquity and precession variations in the Earth's orbit had important roles to play in the deglaciation mechanism.

Inherent in the models presented here is the assumption that orbital and insolation variations are in some way responsible for the timing and magnitude of all climatic variations in the $10^4 - 10^6$ ka frequency band. This assumption is well supported by the clear linear response to the precession and obliquity variations (Hays et al. 1976, Imbrie et al. 1992), but is more tentative with regards to lower frequency behaviour.

5.2.1 Scatterplot Smoothers

Both the methods discussed in this chapter will utilise scatterplot smoothers, so they are introduced here.

Scatterplot smoothers take a series of (x, y) values and draw a smooth curve against x. This provides a graphical representation of the dependence of the mean of the (response) variable, Y, on a (predictor) measurement X.

S-Plus uses the variable span smother called supersmoother. The $k/2$ data points on each side of x_i are used in a linear regression to predict x, and this is run for three values of k, namely $n/2$, $n/5$, and $n/20$. The span producing the smallest smooth, squared residual is then chosen. In regions where the curvature to variance ratio is high a small span is preferred, and where the curvature to variance ratio is low a large span. Further discussions of supersmoother and other scatterplot smoothers are available in Hastie and Tibshirani (1990) and the S-Plus reference manual (S-PLUS 1996).

An illustration of supersmoother is shown in Figure 5.1. This shows 100 data points from a (coral) dataset and the supersmoother estimate.

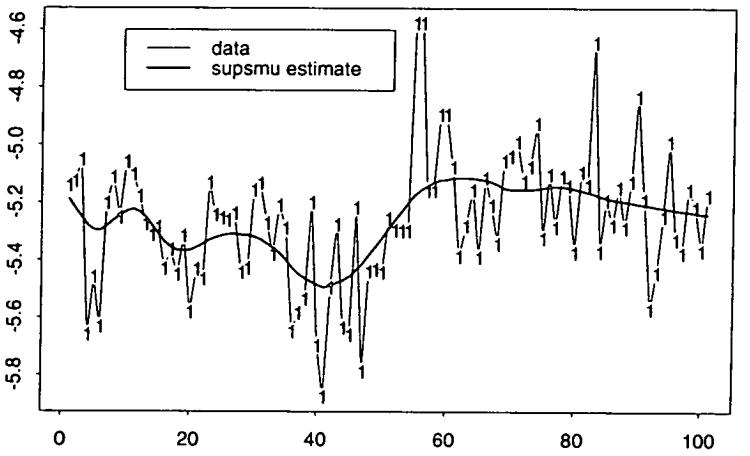

Figure 5.1. An example of a scatterplot smoother, in this case supersmoother, applied to a specimen data set. The variation in the span of the smoother means that the smoother copes well with the different types of behaviour in the data e.g. relatively smooth from points 10-20, large variation around a constant mean (35-45) and rapid step changes (50-55).

5.2.2 The Methods

Standard multiple linear regression has the form

$$y = \alpha + \beta_1 x_1 + \beta_2 x_2 + ... + \beta_m x_m + \epsilon \tag{5.1}$$

where y are the data values, $x_1, ..., x_m$ are the regression variables, $\alpha, \beta_1, ..., \beta_m$ are real valued parameters, and ϵ denotes a set of IID, zero mean, random variables. Its simple least squares basis and easy interpretability have made linear regression a mainstay of statistical analysis. However, this linear form, when coupled with the assumption that ϵ has constant variance, can be unduly restrictive. If the user has some indication of a particular nonlinear transformation which, when applied to a specific regression or response variable could lead to an improved model, then this transformed variable can be included in the model. However, this technique is highly subjective. There exists a large body of statistical work concerning the analysis of transformations for regression. In particular, the Box-Cox method (Box and Cox 1964) uses maximum likelihood estimation to produce a parameterised transformation of the response variable. See Breiman and Friedman (1985) and Tibshirani (1988) for further references.

During the second half of the 1980's two new regression techniques were developed. These attempt to find optimal transformations of the variables so as to maximise the correlation between the regression variables (inputs) and the response variable (output). These differ from standard regression in that we are now replacing the constants $\alpha, \beta_1, ..., \beta_m$ by real valued functions.

In 1985, Leo Breiman and Jerome Friedman developed the method known as Alternating Conditional Expectations (ACE) (Breiman and Friedman 1985), and then in 1987 Robert Tibshirani produced the Additivity and Variance Stabilisation (AVAS) technique (Tibshirani 1988). These methods are broadly similar in that they both assume an additive model and look for smooth transformations of each variable that will yield the "optimal" model. The difference between the methods arises in the definition of optimal. Here we investigate these methods, utilising the relevant functions in S-Plus.

5.3 Alternating Conditional Expectations (ACE)

For a response variable y and regression variables $x_1, x_2, ..., x_p$, ACE attempts to find non-linear transformations $\Theta(y), \phi_1(x_1), \phi_2(x_2), ..., \phi_p(x_p)$ such that the additive model

$$\Theta(y) = \phi_1(x_1) + \phi_2(x_2) + ... + \phi_p(x_p) + \epsilon \tag{5.2}$$

is a good approximation to the data $y_i, x_{i1}, x_{i2}, ..., x_{ip}$, $i = 1, .., n$, where ϵ is independent $N(0, \sigma^2)$. There is no need for a constant in (5.2) (corresponding to the α in linear regression) as it can be absorbed into the transformations.

The fraction of variance not explained by the regression of $\Theta(y)$ on $\sum_{i=1}^{p} \phi_i(x_i)$, also known as the goodness of fit measure, is

$$e^2(\Theta, \phi_1, \phi_2, ..., \phi_p) = \frac{E\left\{[\Theta(y) - \sum_{i=1}^{p} \phi_i(x_i)]^2\right\}}{E\Theta^2(y)}. \tag{5.3}$$

Optimal transformations are defined as functions $\Theta^*, \phi_1^*, ..., \phi_p^*$ that minimise (5.3).

The key property of ACE is that, if the true model is

$$\Theta^0(y) = \sum_{i=1}^{p} \phi_i^0(x_i) + \epsilon \tag{5.4}$$

where $\sum_{i=1}^{p} \phi_i^0(x_i)$ is multivariate Normal and ϵ is Normal , mean 0, and independent of the x_i, then ACE will converge to the correct solution. However, if these

independence and normality assumptions do not hold then ACE may produce theoretical solutions which are not close to the actual solutions.

5.3.1 The ACE algorithm

There follows a brief description of the ACE algorithm for the single predictor case. The algorithm is very similar to that for AVAS which will be discussed in more detail in the following section.

The data based version of Equation 5.3 is

$$\hat{e}^2 = \frac{\sum_{i=1}^{n}[\hat{\Theta}(y_i) - \hat{\phi}(x_i)]^2}{\sum_{i=1}^{n}\hat{\Theta}^2(y_i)} \tag{5.5}$$

where $\hat{\Theta}$ and $\hat{\phi}$, the estimates of Θ and ϕ, are standardised such that $\sum_{i=1}^{n}\hat{\Theta}(y_i) = 0$, $\sum_{i=1}^{n}\hat{\phi}(x_i) = 0$, and $Var(\hat{\Theta}^2(y_i)) = 1$.

It may be shown (Breiman and Friedman 1985) that Θ and ϕ must satisfy the simultaneous equations

$$\phi(x) = E[\Theta(y)|x], \tag{5.6}$$

$$\Theta(y) = E[\phi(x)|y]. \tag{5.7}$$

The theoretical solution of these is then the limit of the following iterated sequence of Alternating Conditional Expectations:

$$\phi^1(x) = E[y|x] \tag{5.8}$$

$$\Theta^1(y) = E[\phi^1(x)|y] \tag{5.9}$$

$$\phi^2(x) = E[\Theta^1(y)|x] \tag{5.10}$$

$$\vdots$$

$$\phi^j(x) = E[\Theta^{j-1}(y)|x] \tag{5.11}$$

$$\Theta^j(y) = E[\phi^j(x)|y] \tag{5.12}$$

$$\vdots$$

The data based algorithm uses a scatterplot smoother to replace the conditional expectations (Section 5.2.1).

5.4 Additivity and Variance Stabilising Transformations (AVAS)

Like ACE, AVAS attempts to find transformations $\Theta(y), \phi_1(x_1), \phi_2(x_2), ..., \phi_p(x_p)$ such that the additive model

$$\Theta(y) = \phi_1(x_1) + \phi_2(x_2) + ... + \phi_p(x_p) + \epsilon \tag{5.13}$$

is a good approximation to the data $y_i, x_{i1}, x_{i2}, ..., x_{ip}$, $(i = 1, .., n)$. The difference between ACE and AVAS is that AVAS chooses $\Theta(y)$ to achieve constant variance of the residuals. Thus, the goal of AVAS is to estimate the function forms of $\Theta, \phi_1, \phi_2, ..., \phi_p$ subject to the following properties:

$$E[\Theta(y)|x_1, ..., x_p] = \sum_{i=1}^{p} \phi_i(x_i) \tag{5.14}$$

and

$$Var[\Theta(y)|\sum_{i=1}^{p} \phi_i(x_i)] = Constant \tag{5.15}$$

where $E[Z|w]$ is the conditional expectation of Z given w.

AVAS requires only that the ϵ are independent of the $x_1, ..., x_p$ and have $Var(e) = constant$. It does not breakdown when normality of ϵ and the $\phi_i(x_i)$ fails to hold.

An important difference for regression and prediction is that AVAS always produces a $\Theta(y)$ which is strictly increasing, therefore guaranteeing the existence of Θ^{-1}. This makes it possible to utilise the transformed regression variables in the future, and use the inverse transform of Θ to predict future values of y, via $\hat{y} = \hat{\Theta}^{-1}[\sum_{i=1}^{p} \hat{\phi}_i(x_i)]$.

Tibshirani believes that ACE is more suited for correlation analysis than regression. There are several reasons for this, particularly that (at least for the bivariate case) ACE is essentially symmetric in X and Y, and this leads to transformations that maximise correlations but are not necessarily the model transformations. See Hastie and Tibshirani (1990) for a discussion of the theoretical advantages of AVAS over ACE (for regression).

5.4.1 The AVAS algorithm

Single Predictor Case

We continue with the same notation as for ACE.

For the single predictor case we have

$$\Theta^0(y) = \phi^0(x) + \epsilon \tag{5.16}$$

where Θ is strictly increasing and ϵ has mean zero and is independent of x.

For Θ known, the mean of $\Theta(y)$ as a function of x is

$$\phi(x) = E[(\Theta(y)|x]. \tag{5.17}$$

If

$$v(u) = Var[\hat{\Theta}(y)|\phi(x) = u] \tag{5.18}$$

then, from Box and Cox (1964), it is known that $Var[h(\hat{\Theta}_(y))|\phi(x) = u]$ will be constant if h is computed according to

$$h(t) = \int_c^t \frac{1}{\sqrt{v(u)}} du \tag{5.19}$$

for some constant, c. AVAS then uses this equation to update Θ given ϕ.

As with ACE, uniqueness is assured by assuming that $E(\Theta) = E(\phi) = 0$ and $Var(\Theta) = 1$. Then the AVAS procedure is to iterate these two steps, namely, finding the mean function given the response transformation, and approximating the variance stabilising transform given the mean.

Multi-Predictor Case

The data version of AVAS on S-Plus works as follows:

1: **Initialise:** Set $\hat{\Theta}(y) = (y - E(y))/\sqrt{Var(y)}$, and then backfit on $x_1, ..., x_p$ to get $\phi_1, ..., \phi_p$. The backfitting procedure computes estimates for ϕ_k one at a time by treating

$$\hat{\Theta}(y) - \sum_{k=1, k\neq i}^{p} \hat{\phi}_k(x_k)$$

as the response. This procedure is cycled through the $x_i's$ until convergence.

2: **Calculate new Θ:** This is achieved in three stages:

- We need to estimate the variance function

$$v(u) = Var[\hat{\Theta}(y)|\sum_{i=1}^{p}\hat{\phi}_i(x_i) = u].$$

This is achieved by applying a running straight lines smoother to a plot of $\log r_i^2 = \log[\hat{\Theta}_(y_i) - \sum_{j=1}^{p}\hat{\phi}_j(x_{ij})]^2$ versus $u_i = \sum_{j=1}^{p}\hat{\phi}_j(x_{ij})$. The result of this smoothing is then exponentiated, giving an estimate of $\hat{v}(u) \geq 0$, and truncated below at 10^{-10} to avoid division by zero in Equation 5.20.

- Then, the variance stabilising transformation is calculated from

$$h(t) = \int_c^t \frac{1}{\sqrt{v(u)}}du \tag{5.20}$$

using the Trapezoidal rule.

- Update Θ by setting $\hat{\Theta}(y) - h(\hat{\Theta}(y))$ and then standardise

$$\hat{\Theta}(y) - \frac{\hat{\Theta}(y) - E[\hat{\Theta}(y)]}{\sqrt{Var(\hat{\Theta}(y))}}$$

3: Calculate new $\hat{\phi}_i's$: Backfit $\hat{\Theta}(y)$ on $x_1, ..., x_p$ to obtain new estimates of $\hat{\phi}_1, ...\hat{\phi}_2$.

4: Iterate steps 2 and 3 until convergence: Convergence is reached when

$$R^2 = 1 - \hat{e}^2 = 1 - e[\hat{\Theta}(y) - \sum_{i=1}^{p}\hat{\phi}_i(x_i)]^2$$

does not change significantly.

In this algorithm all expectations are replaced by sample averages and conditional expectations by scatterplot smoother estimates.

5.5 ACE or AVAS?

In the previous sections we have dicussed the separate merits of ACE and AVAS. For theoretical reasons it would appear preferable to use AVAS, and the following examples illustrate this in practical situations. The first example will also be used to illustrate some of the forms which the transforms may take.

5.5.1 Synthetic Example

The AVAS technique is available as part of the statistical software package S-Plus. To illustrate the application of AVAS on S-Plus, the interpretation of the resultant transforms, and to give a direct comparison between AVAS and ACE, the following artificial data set was constructed. Consider the model

$$Y = \phi_1(X_1) + \phi_2(X_2) + \phi_3(X_3) + \phi_4(X_4) + \epsilon \tag{5.21}$$

where

$$\begin{aligned}
\phi_1(X_1) &= X_1^2 \\
\phi_2(X_2) &= 1 - X_2 \\
\phi_3(X_3) &= \log_{10}(X_3 + 1) \\
\phi_4(X_4) &= \begin{cases} 0 & : \quad X_4 \leq 0.5 \\ X_4 - 0.5 & : \quad X_4 > 0.5 \end{cases}
\end{aligned}$$

for $X_1, X_2, X_3 \sim U[0,1]$, $X_4 \sim U[0,1]$ and $\epsilon \sim U[0, 0.5]$. Here, $U[a,b]$ denotes the continuous uniform distribution on the interval $a \leq X \leq b$.

This process is additive, and is chosen to contain, respectively, quadratic, linear, logarithmic and piecewise linear terms. This allows us to illustrate a wide range of transformation types, and the differences between them and the smoothed estimates resulting from AVAS and ACE.

Figure 5.2 shows the resulting transformation estimates from AVAS and ACE along with the actual tranformations used in the construction of the dataset. Both methods have coped well with the variety of transforms, and they both reproduce Y well (not shown). However, the ACE transform has extraneous "wiggles" at low values of X_3 and low and high values of X_4. It is assumed that, as ACE and AVAS utulise the same smoothing function, that these deficincies are not due to insufficient smoothing. These aberations have a minimal effect, but their presence, together with the theoretical disadvantages of ACE, suggest that it is preferable to use AVAS here, especially since it involves no inherent loss of information. Subsequent data analysis in the following section supports this conclusion.

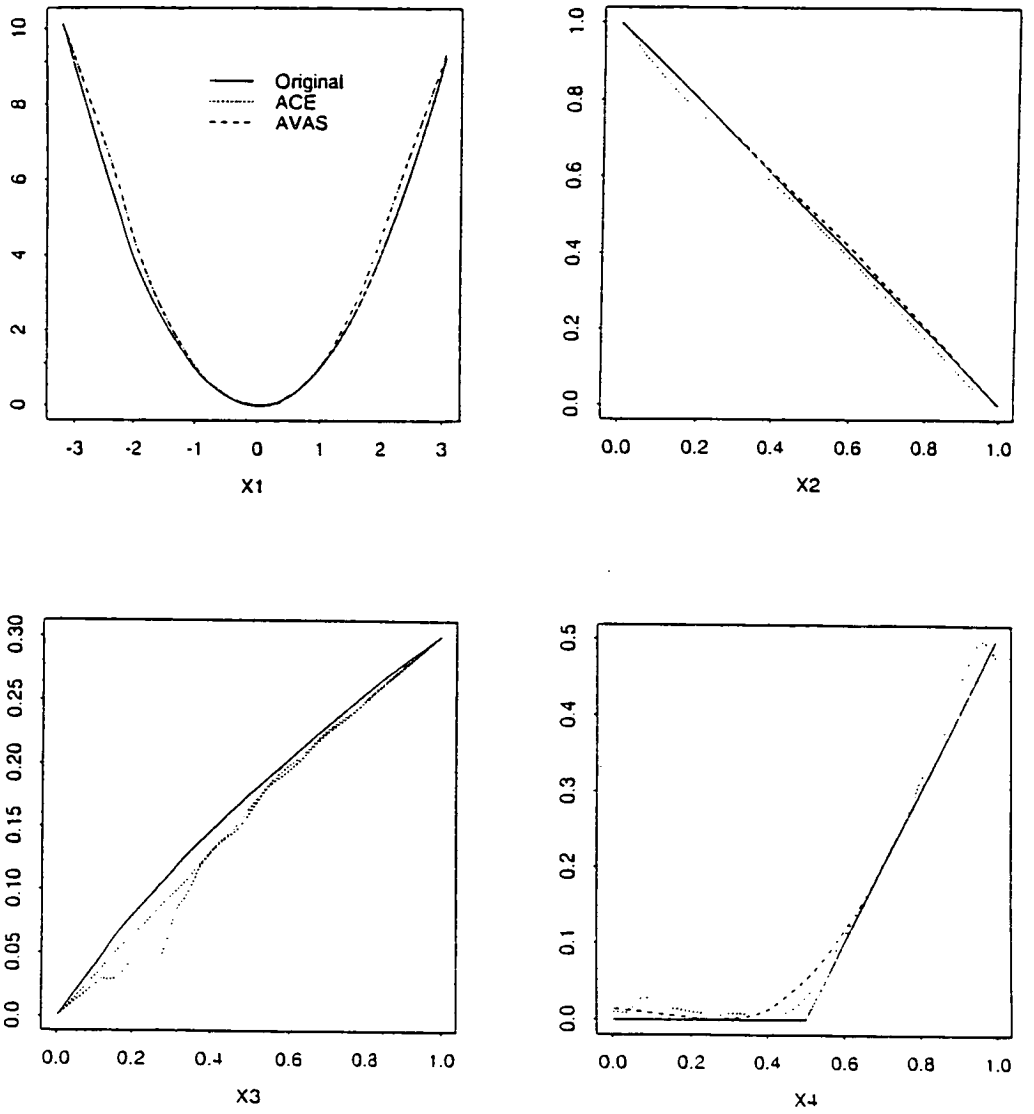

Figure 5.2. The transformation estimates for ACE and AVAS, and the actual transforms used. Both methods reproduce the original transforms well, although there is some erratic behaviour in the ACE transform for low values of X_3.

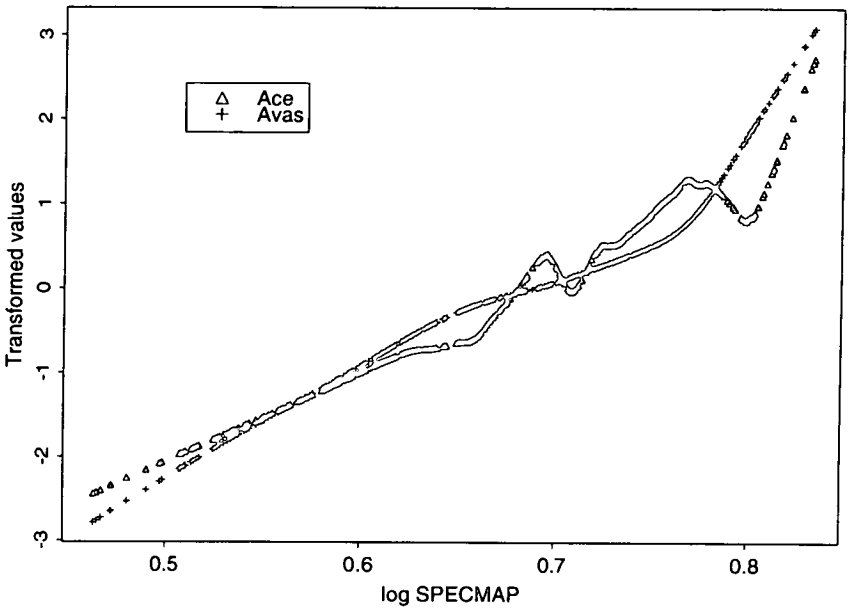

Figure 5.3. ACE and AVAS estimates of SPECMAP transform. Note the more complicated behaviour of the ACE transform

5.5.2 Further Comparison

As a further comparison, the two methods are applied to the problem of modelling the 600 ka SPECMAP record using 4 Milankovitch inputs. Figure 5.3 shows the Θ (SPECMAP) transformation for the ACE and AVAS analyses. Using ACE, Θ is clearly not monotonic and therefore is useless for future predictions. It is possible to enforce linearity on Θ in the ACE algorithm, and thus ensure monotonicity, but this would not always be desirable. Also, Figure 5.4 shows the transformations of the four regression variables using ACE and AVAS. Comparison between the two sets of transforms shows that the ACE analysis yields more complicated transformations, which are subsequently much more difficult to model. The complicated features of the ACE transforms (e.g. the oscillations for low values of precession) can be ignored as artefacts of the methodology, as shown to occur in the previous synthetic example. These transforms will be analysed in Section 5.7.2.

The conclusion is that it will be legitimate to focus our attention on AVAS as it captures all the information of ACE without the latters theoretical shortcomings and misleading transformations.

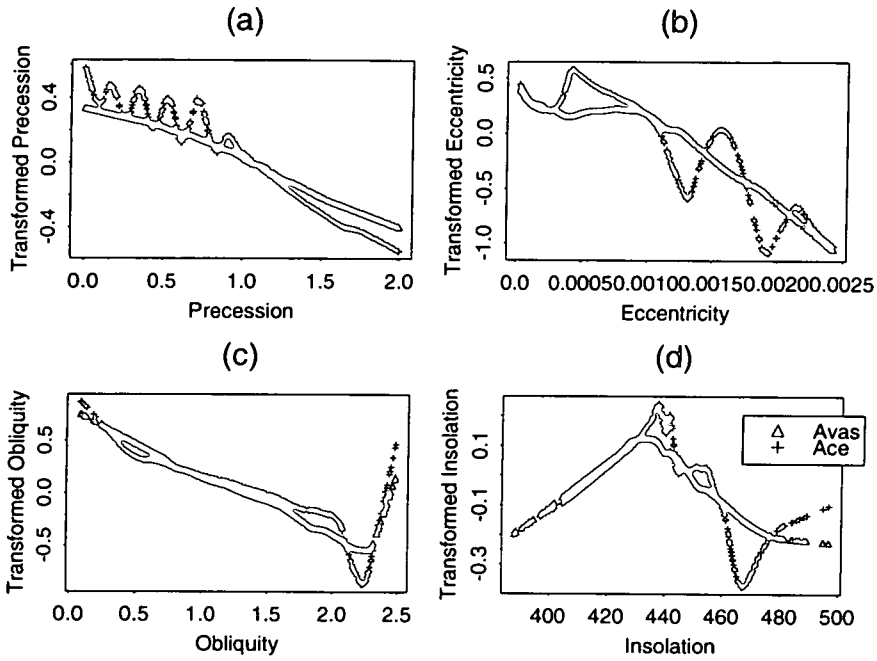

Figure 5.4. A comparison of the ACE and AVAS estimates of the four transforms for the 600ka SPECMAP record

5.6 Interpretation of Transformations

For each regression variable, a plot of the original data against their transformed values gives a graphical description of that input variable's contribution to the output. This is an extremely useful visual representation of the effect of each individual input. It can be used to identify input contributions, such as linearity, piecewise linearity (with thresholds), or non-linearity (logarithmic, squared etc.). The synthetic example in the previous section shows transforms for quadratic, linear, logarithmic and piecewise linear behaviour (Figure 5.2). The transformed values can also indicate the magnitude of the contribution of particular inputs, although there is no set theory for measuring this. Indeed, since our "prediction" is simply the sum of the transformed inputs, the magnitude of the standard deviation (S.D.) associated with each transform signifies an approximate measure of its importance to the final model (Breiman and Friedman 1985). However, caution must be exercised here, since (for example) a variable may have a negligible effect except at particular values where its effect may be very important. In this situation the variable's S.D. may under-estimate its relative importance.

In order to make predictions beyond the test period it is necessary to interpret the resulting plots, and to estimate a suitable function which characterises each

transformation. For example, if the smoothed scatterplot can be approximated by two straight lines, it means that we are fitting a non-linear threshold model, with the changepoint in the scatterplot indicating the threshold level. In more complicated instances it may be necessary to use polynomial, logarithmic or exponential approximations.

A weakness of the AVAS methodology in its present form is the lack of any confidence intervals on the transformations. This means that interpretation of the significance of individual transformations is difficult. It is therefore vital that the transforms are interpreted for physical credibility before being mathematically characterised.

As the model is additive we are able to analyse the individual contributions of each regression variable. Thus we are able to deduce which orbital parameters are responsible for each climatic event. This is particularly useful in investigating the cause of the deglaciations. By definition, the AVAS model has no interaction terms, but these could be included, if necessary, by explicitly defining particular variable combinations as inputs.

5.7 Results

5.7.1 Choice of Regression Variables

To carry out any regression, we must first choose our regression variables. We wish to investigate the influences on an observed climatic sequence of the three main solar orbital parameters: eccentricity; obliquity; and the precession of the equinoxes (Berger and Loutre 1991). Though eccentricity (e) and obliquity (ϵ) are simple to interpret, the choice of precession variable is less clear than the often quoted variable $e \sin \omega$ (where ω is the angle between the vernal equinox and perihelion) which represents a measure of the average Earth-Sun distance in summer. Given that we wish to analyse the direct precession effect through the relationship between the seasons and the perihelion, we are more interested in ω itself.

We may be interested in introducing time-lags in some or all of the regression variables. This would not only have an important effect on the contribution of any given variable, but it would also influence the value of any threshold in the transforms.

In addition, we shall specify the insolation values for July $65°N$ as a further regression variable. By explicitly including insolation we can observe the effect of particularly high or low solar forcing, and thereby include interactions between the orbital variables. July $65°N$ was chosen as summer insolation near this latitude is a logical forcing for ice sheet variations (Section 1.3.4).

As a general test procedure, different combinations of regression variables were applied to the last 200 ka of the SPECMAP data set. We are particularly interested in the models' ability to reproduce the two sequences of glacial/ deglaciation/ interglacial. As explained above, we cannot simply use goodness-of-fit to choose the best regression variables, and we must compromise between the quality of the fit and the physical plausibility of the transforms.

Initial analysis was carried out using the variables $e, \epsilon, e\sin\omega$ and insolation in July at $65°N$, but this failed to reproduce the last deglaciation. Attempts to model the SPECMAP record using these regression variable values, lagged several thousand years, also failed to model the last 200 ka. After further experimentation we ultimately chose the following regression variables:

- X_1 : precession variable $(|\omega - 180|/90)$;
- X_2 : squared eccentricity (e^2);
- X_3 : obliquity, lagged 6 ka $(\epsilon - 22)$;
- X_4 : insolation at 65°N during July.

The three orbital variables are those from the ACLIN model of Kukla et al. (1981). These enable us to reproduce the past 200 ka very well, in particular the magnitude of the glacials and interglacials and the rapidity of the deglaciations. The independence of the precession variable from eccentricity allows us to extract its individual contribution to climate change more clearly.

5.7.2 SPECMAP

Due to the dating error at around 617 ka bp (Section 1.5.1) we only analyse the time series back to 600 ka bp.

Initial analysis of the 600 ka record, using the regression variables described above, gave poor results. In particular, Θ was steeper for high and low SPECMAP values, and therefore stretched the extremes of the model output, thus decreasing the apparent correlation between the model output and the data. This problem

is indicative of a possible deficiency in the AVAS algorithm, and again highlights the need to review the sensibility of any transformations obtained. This problem was common to all analyses, and two steps were taken to counteract it. First, a log-transform was applied to the climatic time series to reduce the variation within the data. Second, Θ was constrained to be linear. AVAS has options to enforce linearity on any of the transforms, and by ensuring that Θ is linear we reduce the problem of extreme values.

These two steps of taking a log-transform and constraining Θ to be linear are present in all the analyses presented in this chapter. Constraining Θ to be linear will not be overly restrictive as the ϕ_i still have full nonlinear freedom, and will infact have the added benefit of simplifying the transformation characterisation procedure.

Modelling the Last 600ka of SPECMAP

Using AVAS with the 4 Milankovitch inputs, log transformed SPECMAP for the last 600 ka, and linear Θ, we obtained the transformations in Figure 5.4. The precession result suggests that its effect is linear, which would correlate well with general theory, with values of ω near 0/360 giving warmer climate. This equates to the perihelion coinciding with the vernal equinox, and contrasts with the findings of Kukla et al. (1981) who found that warm climates coincided with periods of perihelion near the autumnal equinox. No obvious explanation can be found for this disagreement. However, in Kukla et al. (1981) they state that the present interglacial peak, at 6000 years bp, coincides with September perihelion. However, Berger and Loutre (1991) demonstrated that at 6000 years bp, ω (the longitude of the perihelion from the vernal equinox) was 359.99°, which supports our intepretation.

Obliquity is also felt to have a linear effect on climate, and this is observed in the transformation, up to approximately 2.28 (which equates to a tilt of 24.28°), with higher values of obliquity being associated with warmer climate. Then, for values above this, the influence is decreased, even partially opposite (i.e. high obliquity implying cooler climate). Subsequent analyses imply that this behaviour at high obliquity values is anomolous.

The eccentricity transform is non-linear, and could be approximated by a horizontal line from 0 to 0.001, and then a line of negative slope for higher values. This implies that the eccentricity has constant influence up to 0.001 (an eccentricity value of $e = 0.0316$) and then an approximately linear input for higher

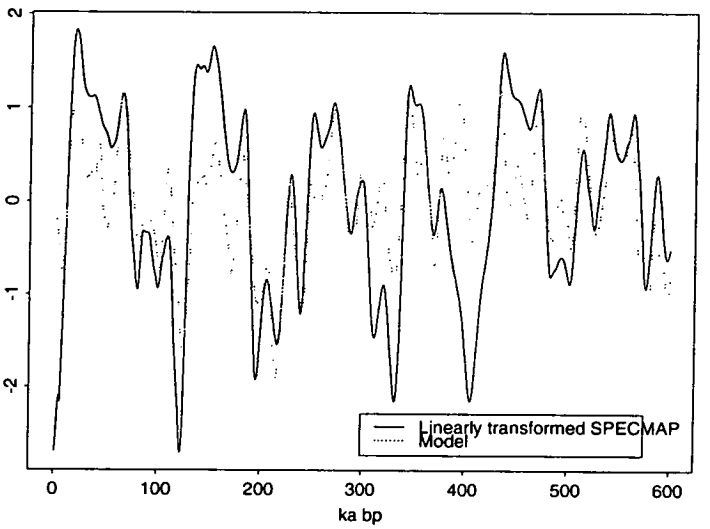

Figure 5.5. The model estimate for the last 600ka of SPECMAP. The model works well for the older section of the record when the ice age cycle had smaller amplitude, but does not reproduce the scale of variation in the remaining sections.

values, with the climate warming as eccentricity increases. This is the correct physical result, as higher eccentricity means that the average Earth-Sun distance is decreased and the Earth is receiving more energy from the Sun. The magnitude of the transform, for high values of eccentricity, is large (approaching 1 in modulus), giving it considerable influence when compared to the other variables.

The most curious result is that for the insolation term. Its quadratic appearance suggests that both high and low levels of insolation correlate with warm periods, and that less extreme values correlate with colder periods. This has interesting physical implications, if correct. However, it should be noted that its overall contribution is small, with modulus mainly less than 0.2 and a relatively low S.D., and therefore its transformation can be seen as less reliable.

Figure 5.5 shows the resulting model fit. It is reasonable, but not visibly better than the original linear fit, so we must investigate further. Throughout the last 600 ka the climate behaviour (as signified by the SPECMAP record) has changed. From 600-400 ka bp, the mean value was higher than at present, and the amplitude of variations has increased to the present day. This may signify a changing relationship between the orbital variations and the climate, which would lead to confusion when looking at the entire dataset. We investigate these variations by looking at a sliding data window.

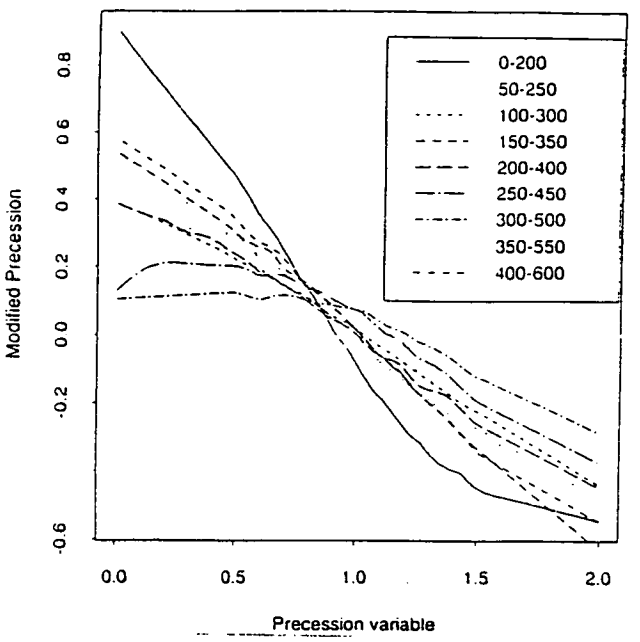

Figure 5.6. The window estimates of the precession transform, showing consistent linearity, and confirming its dependence upon eccentricity by the slope (and therefore significance) of the transform varying in line with eccentricity variations.

Sliding a 200 ka Window Along SPECMAP

A window length of 200ka was chosen. This ensures that all the input variables cover at least 2 cycles. Any shorter than this and our window would cover only one whole eccentricity cycle, and AVAS would be unrestrained in transforming the unique eccentricity values. Consequently, the transformations could be made to fit the data, but would not yield interpretable results.

Figures 5.6, 5.7, 5.8, and 5.9 show the transformations, and figure 5.10 the model fits, for each of the nine windows. In general the predictions are very good, with perhaps some loss in performance for the older time periods. This is signified by the decreasing value of R^2 in Table 5.7.2. The transformations are reasssuringly consistent through time.

We look first at the variation through time of each transformation.

Precession (Figure 5.6) The precession transform constantly suggests linearity, as expected from previous orbital studies. However, the relative importance of the precession input is seen to change through time as the slope of the transform varies (the steeper the transform the larger the contribution to the model). We see that the slope decreases as we go back in time to

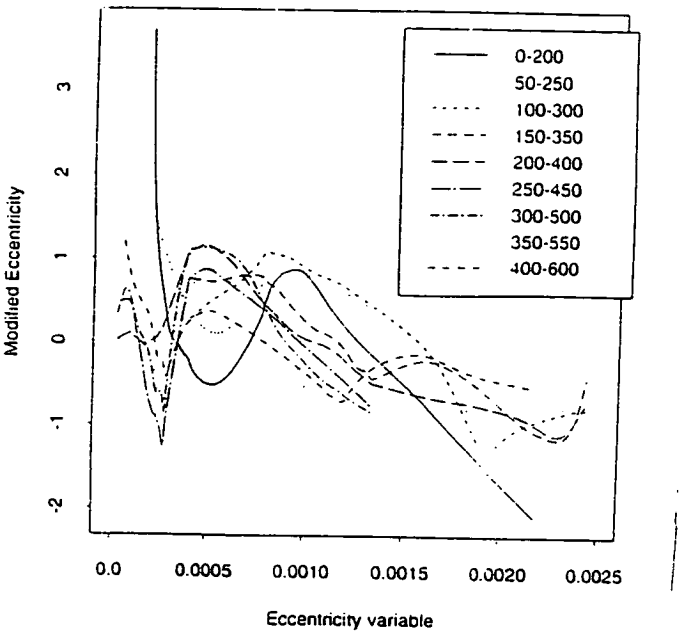

Figure 5.7. The window estimates of the eccentricity transform, indicating the correspondence between high obliquity and warm climate.

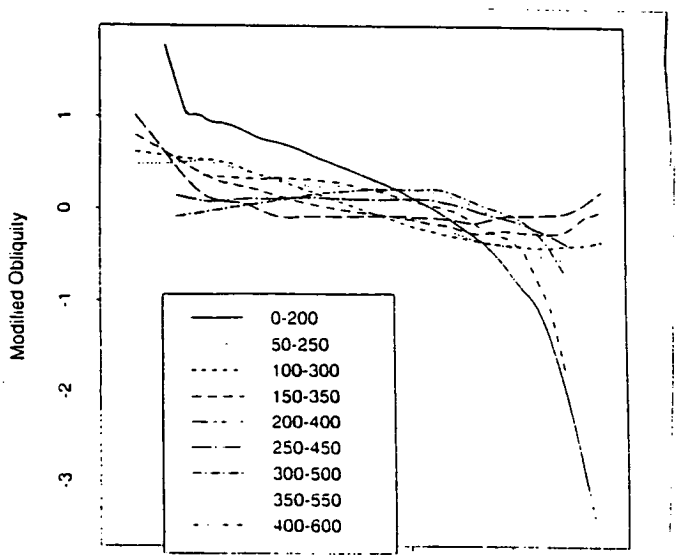

Figure 5.8. The window estimates of the obliquity transform, which are generally linear, with a steeper linear model for high values.

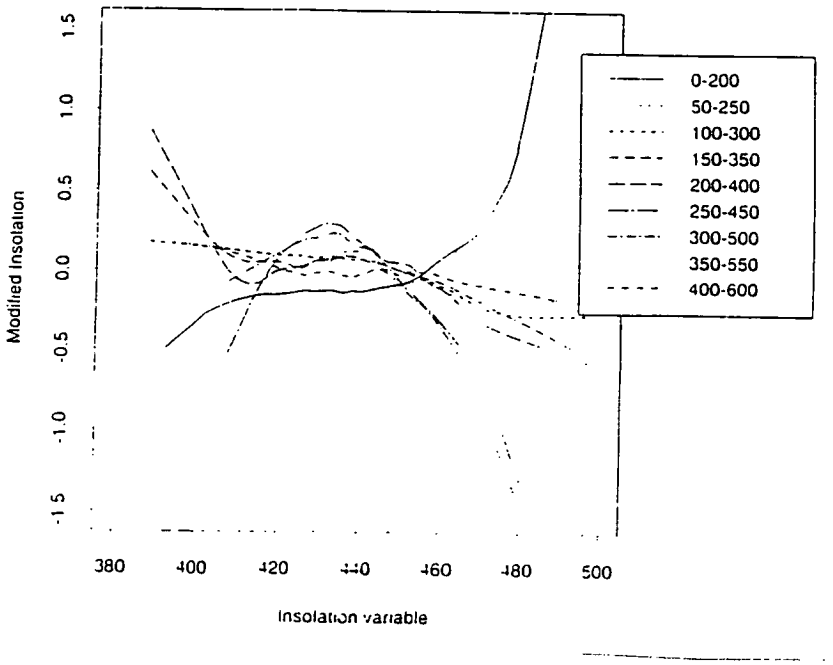

Figure 5.9. The window estimates of the insolation transform, displaying no consistent signal.

Window (ka)	R squared	Prec'n S.D.	Ecc'y S.D.	Obl'y S.D.	Ins'n S.D.
0-200	0.8166	0.468	1.104	1.04	0.311
50-250	0.828	0.310	0.773	0.389	0.122
100-300	0.891	0.252	0.841	0.374	0.144
150-350	0.660	0.348	0.641	0.259	0.162
200-400	0.611	0.260	0.666	0.199	0.201
250-450	0.704	0.198	0.636	0.149	0.307
300-500	0.705	0.134	0.622	0.228	0.299
350-550	0.546	0.289	0.555	0.259	0.180
400-600	0.633	0.355	0.507	0.428	0.052

Table 5.1. R-squared values, and Standard Deviations of inputs, for SPECMAP windows

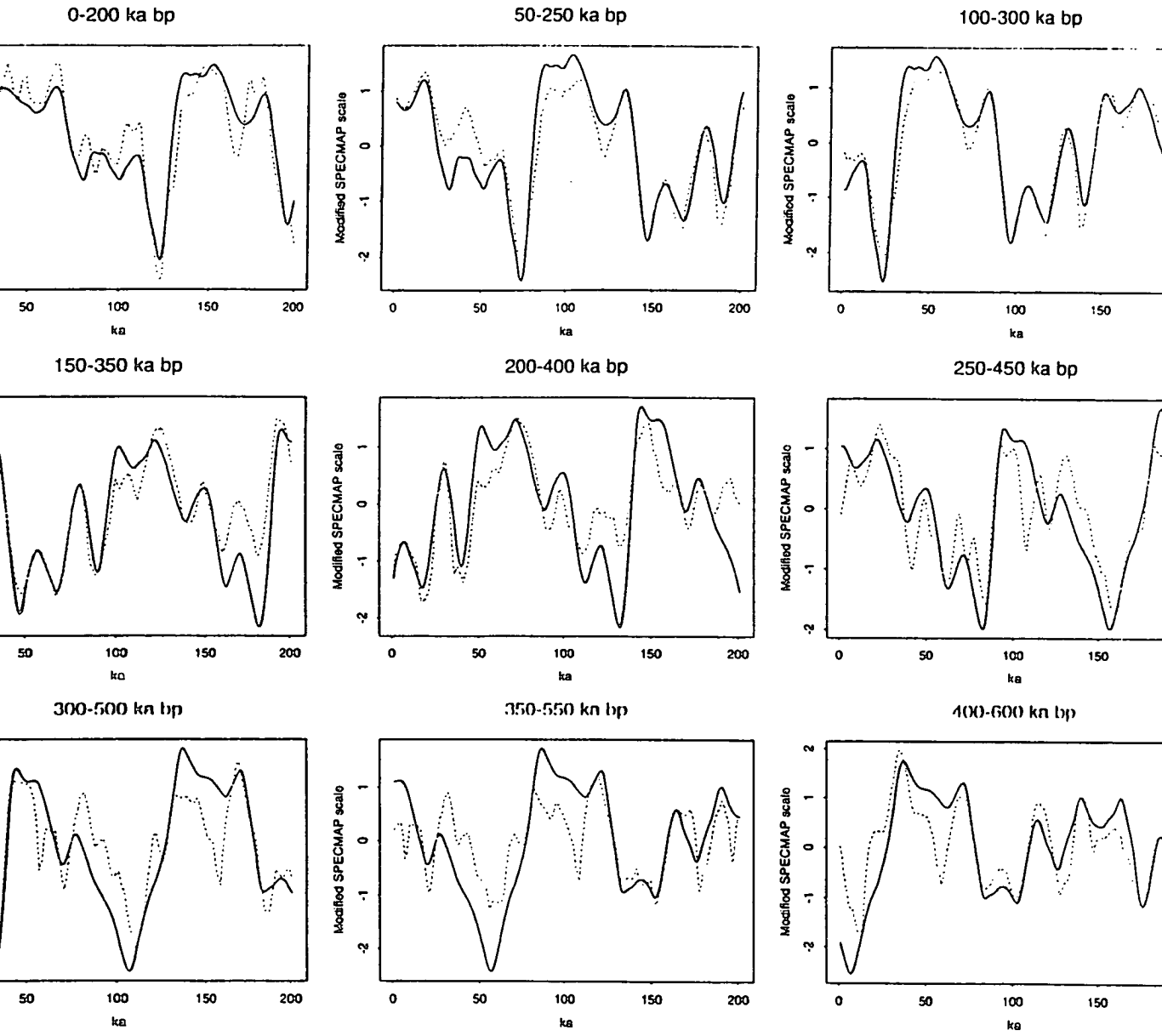

Figure 5.10. The model fits for the window analysis of SPECMAP. The solid line is the SPECMAP record, and the dashed line is the model estimate based on the transformations for that 200 ka time slice. The fit is generally very good as we capture the timing and scale of most climatic variations.

a minimum in the 300-500 ka bp window. Similarly, the S.D. decreases back to a minimum at 300-500 ka bp, and then increases again. This is an excellent result, as the precession variable used here is the absolute value of $(\omega - 180)/90$, where ω is the angle between the moving vernal equinox and the perihelion. A much superior variable (with regards to correlation with climate records) is $e \sin \omega$, where e is the eccentricity, and this has a low value (due to low eccentricity) around 400 ka bp. So AVAS is confirming this by varying the importance of ω in accordance with the variations in eccentricity. The one discrepancy is for the 0-200 ka bp window. This has the steepest slope and the highest S.D. of all the time slices, but eccentricity is relatively low for the last 100 ka. This is due to the the increase in the magnitude of climate change towards the present day, and is signified in Table 5.7.2 where the most recent window has the largest S.D. values for every input variable.

Obliquity (Figure 5.7) Again the transforms suggest predominantly linear behaviour, but with perhaps non-linear behaviour at high and low values. Half of the windows suggest that low obliquity values have a slightly stronger cooling effect, particularly 0-200 and 200-400 ka bp, with threshold values of around 0.3-0.4. For high values (high tilt) we see four curves suggesting a small increase (colder) for high obliquity, and four suggesting a stronger warming for high values. Higher obliquity values are associated with warmer climate due to the subsequent Northern Hemisphere warming. Consequently, the deduction about obliquity's effect is that it is linear, warming as obliquity increases, to a threshold value around 24.1° where a steeper linear model takes over. This suggests that high obliquity values correlate with warmer climate.

Eccentricity (Figure 5.8) The behaviour here is more difficult to explain, both for individual windows and for overall behaviour. The most consistent feature is that high values of eccentricity are associated with warmer climate, with an approximately linear relationship for $e^2 > 0.01$. Below this we see a general reduction in transform values, and then an increase again for very small values ($e^2 < 0.0003$). Between the two thresholds the behaviour is widely varying, although the general behaviour of decrease, turning point, increase, turning point, decrease as eccentricity increases suggests some similarity. That this similar behaviour is blurred may be a result of the 400

ka cycle in eccentricity. Note also that the S.D. increases as we go forward in time, highlighting the gradual increase in the amplitude of the ice age cycle towards the present day.

July 65N Insolation (Figure 5.9) The behaviour here is extremely variable, but the most important point to note is that the S.D. of the transforms are consistently small (of the 4 variables, insolation has the lowest S.D. for the 4 most recent windows). This suggests that its importance is small and therefore its results may be less significant. The majority of the transformed points lie between $+/-0.5$, thus contributing little to the model. The 0-200 ka window shows high values of the transform for high values of insolation. This must be anomalous (high energy corresponding to cold climate?), and a closer examination of the last 200 ka revealed that this spike in the insolation transform is simply the method using the high insolation values at one point to give improved fit. The general deduction is that insolation has a constant (therefore essentially negligible) input, with perhaps a slight warming input for higher ($> 450 Wm^{-2}$) values.

We now look at the fit of the model for each window, shown in Figure 5.10.

0-200 ka bp The fit of this model is excellent. It manages to fully capture the two deglaciations and the overall scale of the variations. The only point of concern is at the present day, where there is a large discrepancy for the last 3 ka. The model wants the Earth's climate to have started cooling 3000 years ago. This cooling has actually happened (though not to the extent indicated in the model), but is not reflected in the SPECMAP as it represents ice volume, which lags the climate changes by several thousand years.

Older time periods The quality of the fit for the older periods is good, still capturing most of the features. The possible exception is 350-550 ka bp where the fit is poorest, signified by the low value of R^2. This may be a consequence of the low eccentricity values at this time.

What Triggers the Deglaciations?

The cause of deglaciations is one of the most important outstanding questions in relation to Quaternary climate change. Figure 5.11 shows the contribution of

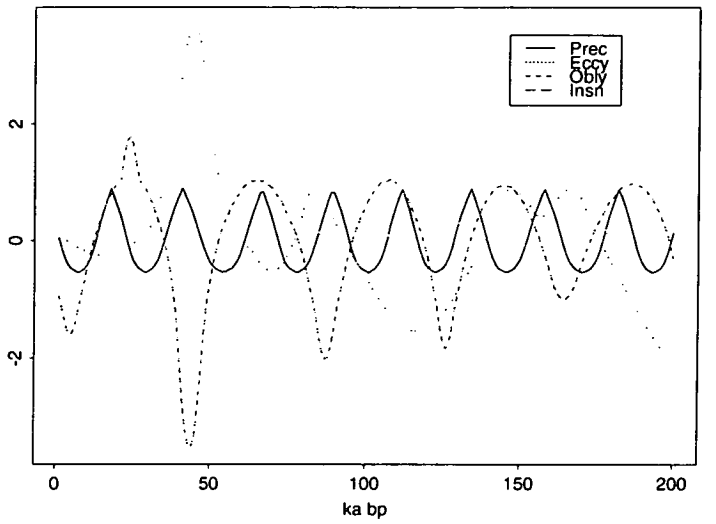

Figure 5.11. The contributions of each variable to the 200 ka SPECMAP model

each parameter to the model for the last 200 ka. The last glacial maximum ($\sim$20 ka bp) coincides with a maximum in both transformed obliquity and precession, and the subsequent deglaciation follows a decrease in these two parameters. The stability of the eccentricity transform during the last 30 ka suggests that this has little effect in driving deglaciation. The deglaciation at the end of the penultimate glacial cycle, and leading into the Eemian interglacial ($\sim$130 ka bp), commences with a similar obliquity transform high, and shortly followed by a precession high. Warming again coincides with decreasing obliquity and precession transforms. Further obliquity transform highs at $\sim$90 and $\sim$45 ka bp, followed by decreases, do not coincide with the precession changes and do not produce rapid warming. We therefore conclude that the deglaciations are caused by the combination of increasing obliquity and perihelion approaching the vernal equinox.

5.7.3 Loess

We use the same regression variables as in Section 5.7.2, apply a log transformation to the data, and then constrain Θ to be linear, as for SPECMAP.

Last 600 ka

The fit of this model (Figure 5.12) is poor, with no replication of the ice age variation (100 ka cycle) for the oldest 300 ka period.

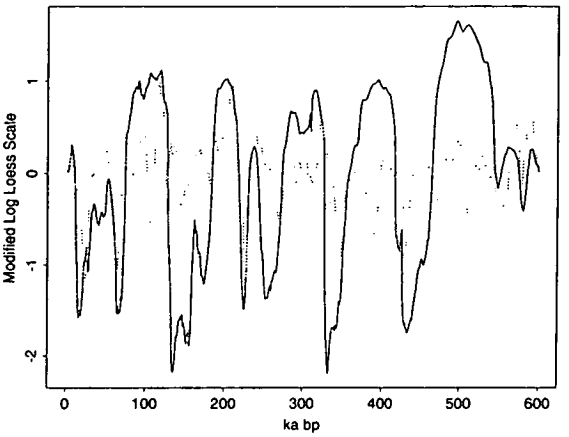

Figure 5.12. Loess fit for the last 600ka

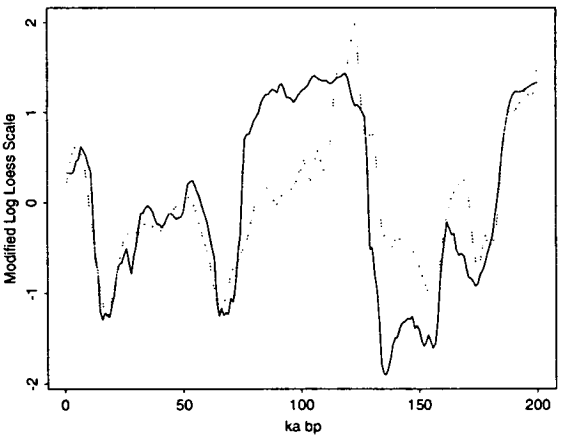

Figure 5.13. Loess fit for the last 200ka, showing an excellent fit, except for during stages 5a-5d where the model more closely resembles the oceanic records.

Last 200 ka

The model is more succesful at reproducing the data for this shorter time period, and reproduces the scale and timing of most climatic changes. The one problem is for the period corresponding to oxygen isotope stage 5, where the loess record is fairly constant in value for nearly 50 ka. Our prediction more closely resembles other climatic indicators (e.g. marine records) with a pronounced warm period (stage 5e) followed by a more temperate period (Figure 5.13).

Given that the fit is much better for this shorter interval, the transforms (Figure 5.14) are still very similar to those for the 0-600 ka analysis, with the exception of the sign of the curvature of the obliquity transform. As with SPECMAP, the

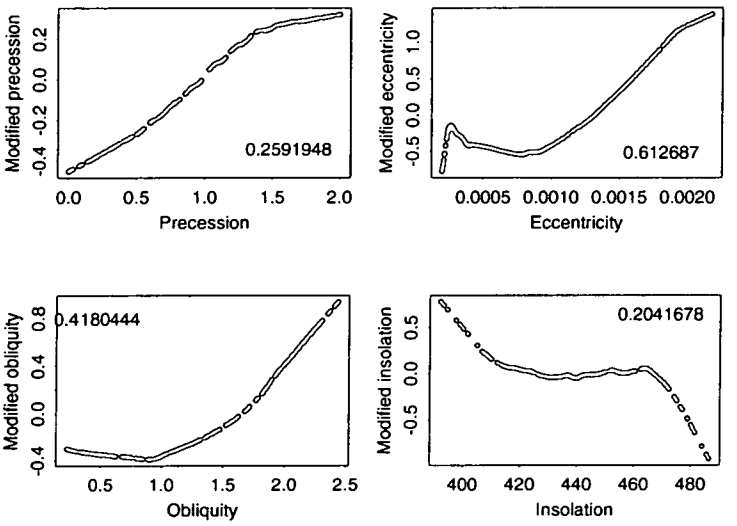

Figure 5.14. Transforms for the 200ka Loess analysis and the SD of each variable.

precession term is linear, with values of ω near 0 corresponding with warmer climate (note that the loess record is the reverse of the SPECMAP record, with high values corresponding with warmer climate). Eccentricity has high values correlating with warmer climate, and a linear relationship for values above 0.001 ($e > 0.032$). Obliquity suggests an approximately constant effect up to 1, and then a linear relationship above that threshold, with increasing obliquity corresponding with warmer climate. The insolation term is 'upside down' with high insolation coinciding with cooler climate. It is the least significant variable in this analysis. If we look closely at the role of the transformed insolation we see that the high and low values are each one lone spike in the last 200 ka. We therefore argue that we can ignore this term (intermediate values are approximately zero).

5.7.4 ODP Site 677

Once again we use a log transform and constrain Θ to be linear.

Last 600 ka

Figure 5.15 shows the fit for the last 600ka. This model works well, particularly back to 350 ka bp. The nature of the transformations (Figure 5.16) are very similar to the corresponding ones for SPECMAP. Precession is linear with values of ω near 0 correlating with warmer climate. The broad behaviour of the

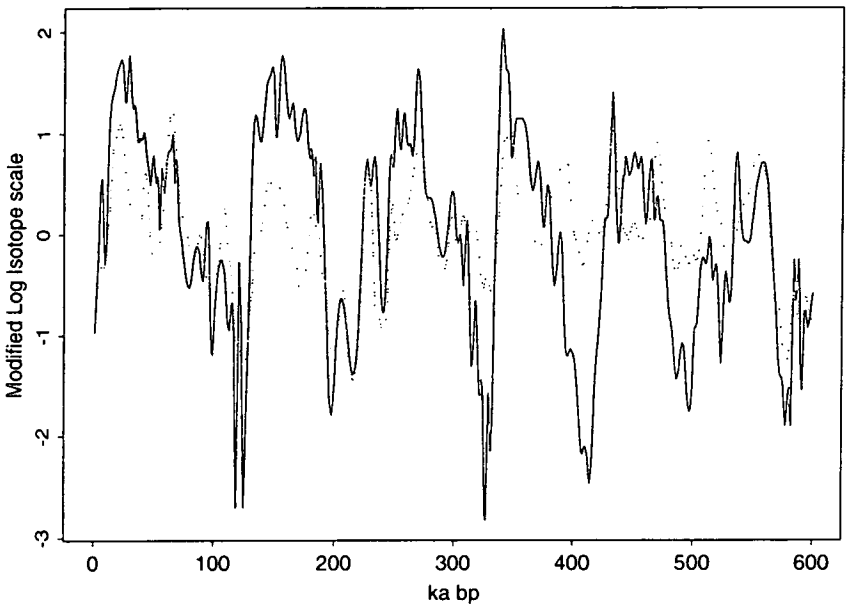

Figure 5.15. Model fit for last 600 ka of the ODP 677 record

eccentricity is approximately constant up to 0.0011, and then linearly increasing. High values of obliquity give warmer climate, except for the highest values (see SPECMAP analysis for discussion of this behaviour). The insolation term is the least significant. The positive effect of its lowest values can be ignored (they correspond to one cycle only), so we are left with the same unusual behaviour as for SPECMAP: high and low insolation values corresponding with warmer climate.

Last 200 ka

Once again the transforms (Figure 5.17) are very similar to those for the corresponding SPECMAP analysis, with the exception of precession which is linear up to a threshold at 1.4. The last 2 glacial cycles are reproduced well (Figure 5.18), particularly the large deglaciation preceeding the Eemian. This comes from the combination of eccentricity, obliquity and precession, whilst the smaller transition into the Holocene is from obliquity and precession only (Figure 5.18).

5.7.5 Devil's Hole Calcite Record

Again the data is transformed using a log transform, and Θ is constrained to be linear.

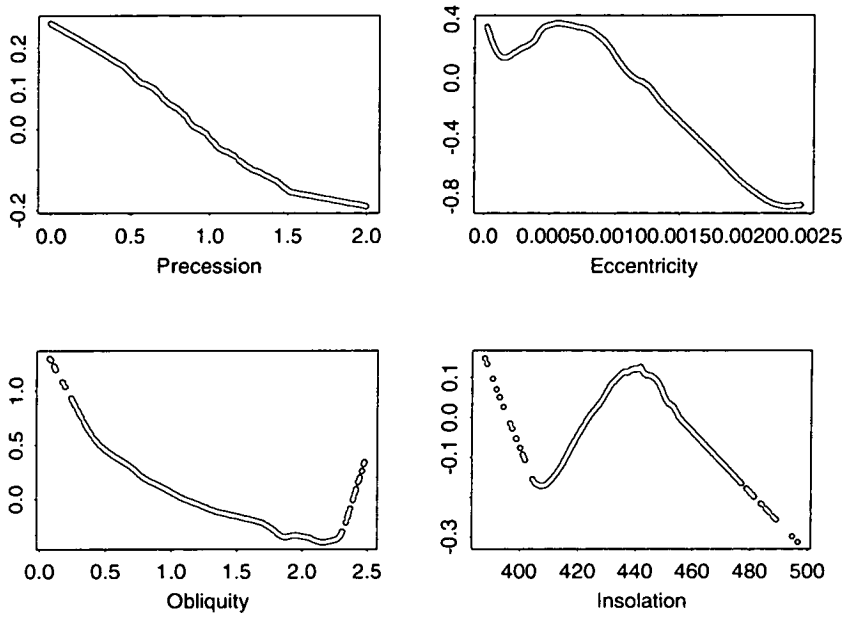

Figure 5.16. Model transforms for last 600 ka of the ODP 677 record and the SD of each variable

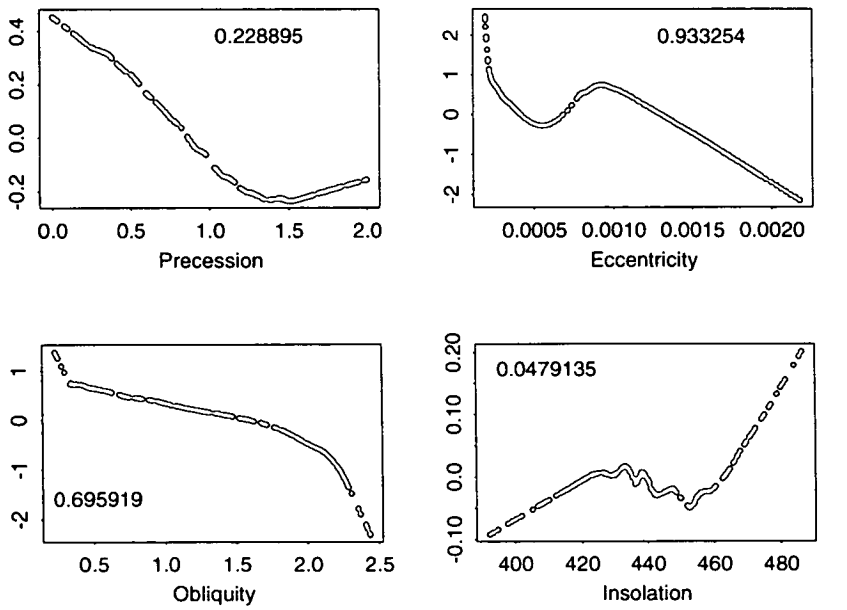

Figure 5.17. Model transforms for last 200 ka of the ODP 677 record.

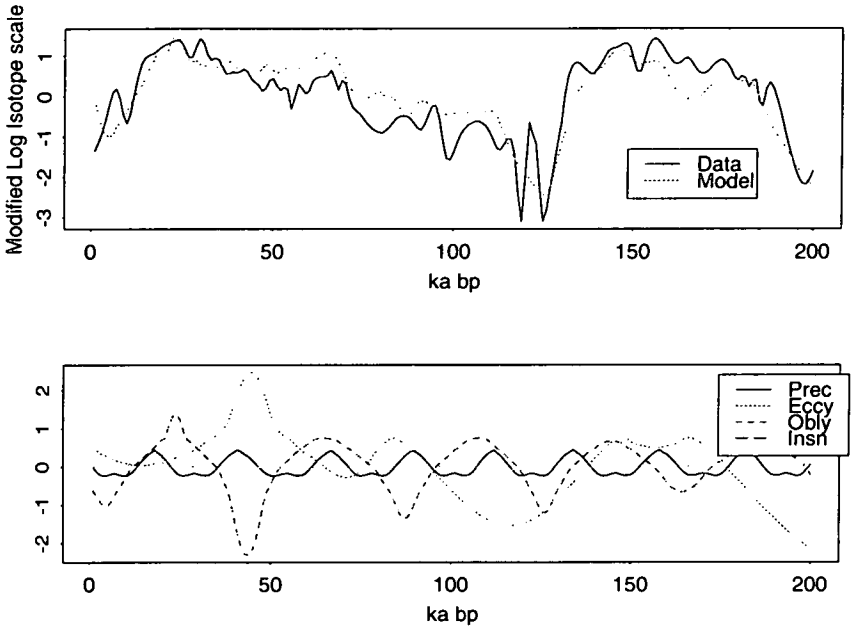

Figure 5.18. Model fit for last 200 ka of the ODP 677 record and the contribution of each variable to the additive model.

Last 600 ka

Qualitatively this model is satisfactory, but quantitatively it fails to reproduce the scale of the variations (Figure 5.19). The last deglaciation is not large enough, and isotope stage 6 is not reproduced. It still has precession and obliquity as linear, and the eccentricity term is monotonic (Figure 5.20). The insolation term is the least significant and is negligible.

Last 200 ka

The predominant feature here is that the model works well for the last 100 ka (Figure 5.21), but prior to this there is a phase lag between sections of the data and the model. The model wants the deglaciation to take place later than it actually does. Once again, this is the orbital theory conflicting with the Devil's Hole time scale. We observe (Figure 5.21) that the pre-Emian deglaciation is produced by obliquity and eccentricity, but the pre-Holocene deglaciation is from obliquity alone. Figure 5.22 shows the transforms obtained. They are very similar to those for SPECMAP as would be expected given the similarity between the records.

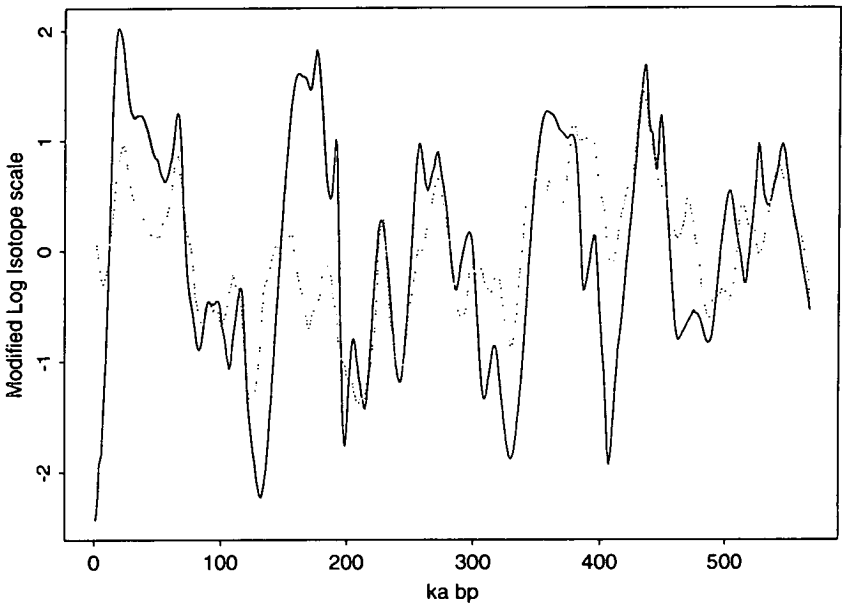

Figure 5.19. Model fit for Devil's Hole

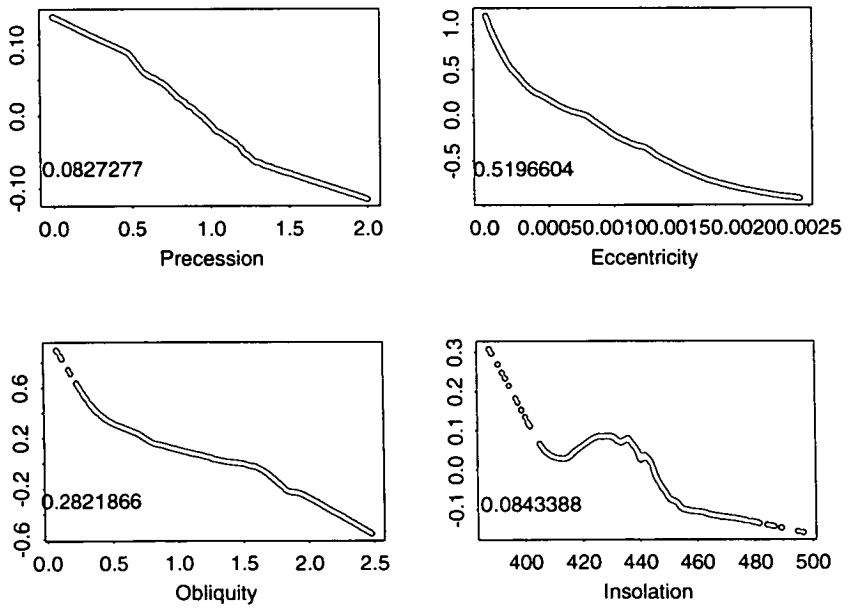

Figure 5.20. Transforms for 600 ka Devil's Hole analysis

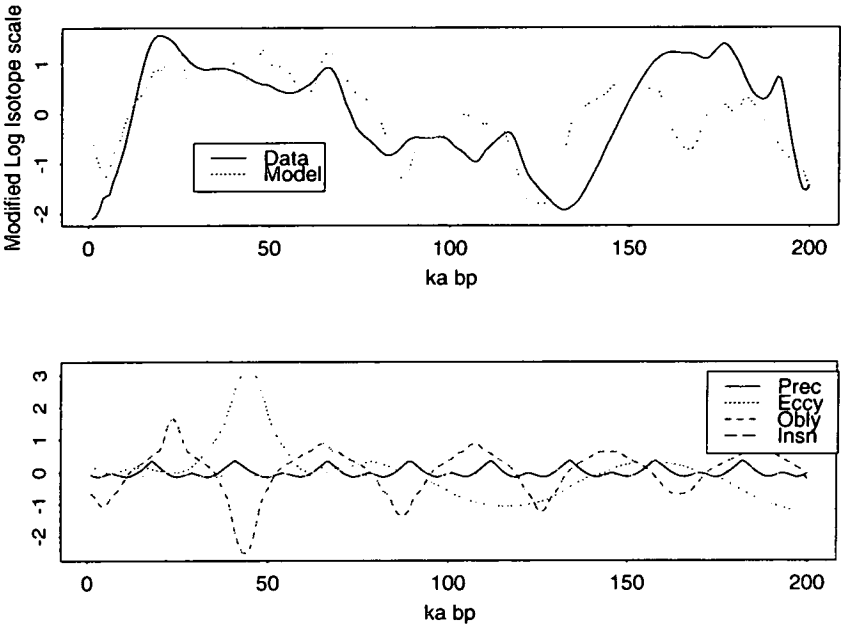

Figure 5.21. Devil's Hole model fit for last 200 ka and the contributions of each variable

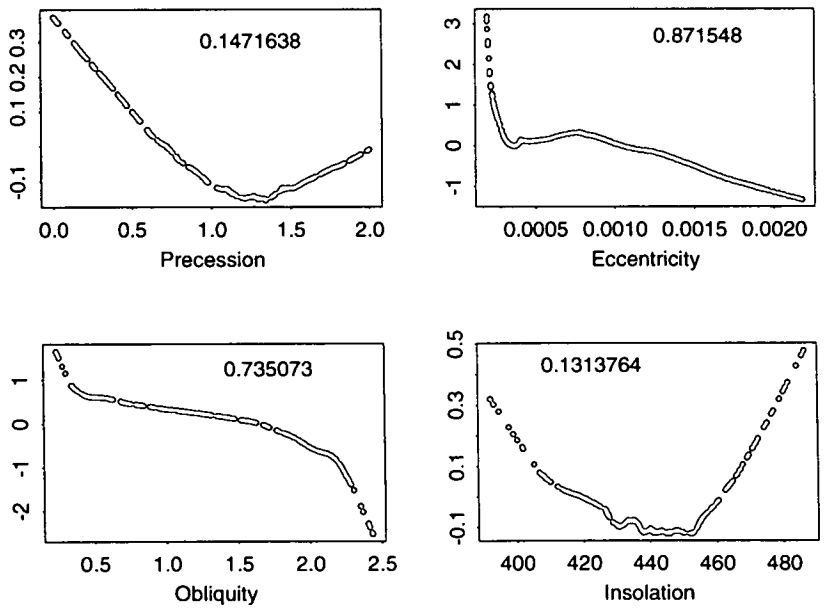

Figure 5.22. Devil's Hole model transforms for last 200 ka and the SD of each variable.

5.8 Characterising the Transforms, and Prediction

If we wish to go on and predict into the future we must first characterise the transformations. This will necessarily be a qualitative process.

There is the question of which transformations to use, as Section 5.7.2 has shown that the relationships are not constant. Should we

- use all the transformations from the last 200 ka, or
- look at the behaviour of the inputs over the next 200 ka and chose the transformation of each from a period when its behaviour was similar?

For the insolation and eccentricity there is no good match within the last 600 ka (eccentricity is small and featureless in the near future) so it was decided to use the transformations from the last 200 ka.

5.8.1 SPECMAP

The approximations used are shown in Figure 5.23. These are not exact (linear) replications of the smooth transforms as the original future prediction overemphasises the obliquity forcing and has an extremely rapid transition into the next glacial from the present day.

Precession This was taken to be linear, with high values correlating with warmer climate.

Eccentricity This is the most complicated to describe, and as a first attempt it was described by 3 linear sections, with thresholds at 0.000505 and 0.000889. The small number of data points for very low eccentricity, which are transformed to large positive values, occur between 40-50 ka bp (Figure 5.10). The corresponding spike in the transformed eccentricity coincides with a negative spike in the obliquity (related to the few obliquity values $> \sim 2.3$). Both these spikes could be removed, so it was felt unnecessary to include high values of the transform for low eccentricity values. However, this still led to an overemphasis of the low eccentricity values in the present and near future. It was therefore decided to restrain the smallest eccentricity values to having zero input.

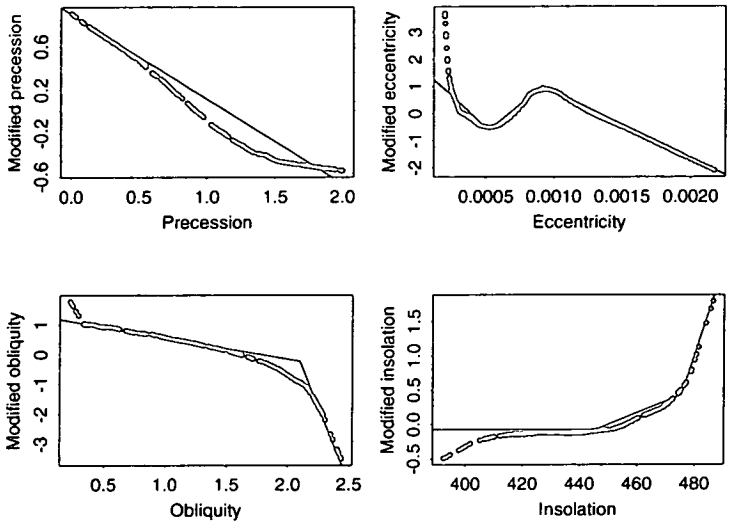

Figure 5.23. The piece-wise linear approximations of the SPECMAP transformations.

Obliquity This was initially divided into 2 linear sections with the threshold at 2.131. This ignores the small kick for very small values, but does model the increased effect of the high values. However, this then overemphasised the strength of the high obliquity induced warming. Experimentation led to a minimum threshold being prescribed of -1.

July Insolation This was initially described by 3 linear segments, with the thresholds at 446.9 and 475.27. However, its role was essentially negligible, and it was ultimately removed from all models.

Using these piecewise linear transforms and the future orbital and insolation variations, we can now make a prediction of the future. Figure 5.24 shows the fitted model and data for the last 200 ka, and the prediction for the next 150 ka.

The final model, using the notation of Page 107 and with Y representing SPECMAP, is:

$$\hat{\phi}_1(X_1) = -0.77 \times X_1 + 0.852$$

$$\hat{\phi}_2(X_2) = \begin{cases} X_2 < 0.00037 & : \quad 0 \\ 0.00037 \leq X_2 < 0.000505 & : \quad -4776 \times X_2 + 1.76 \\ 0.000505 \leq X_2 < 0.000889 & : \quad 4447.5 \times X_2 - 2.89 \\ X_2 \geq 0.000889 & : \quad -2347 \times X_2 + 3.15 \end{cases}$$

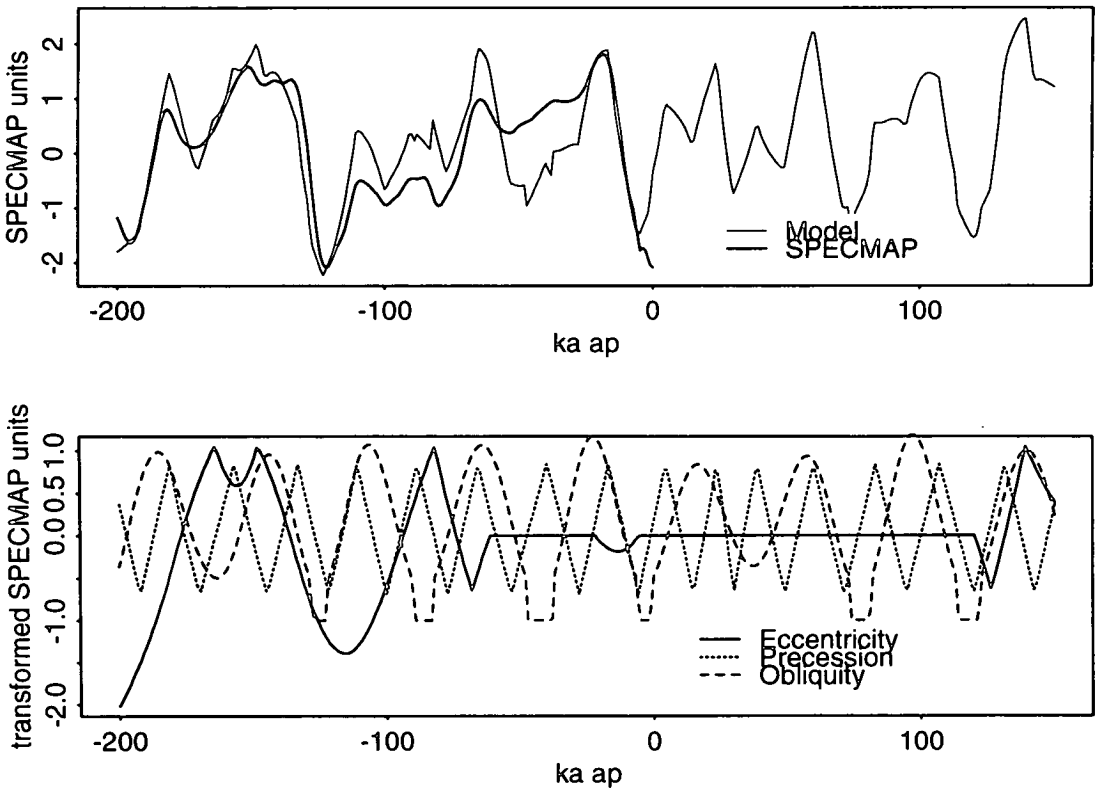

Figure 5.24. The SPECMAP model fit for the last 200 ka, using the linear transform approximations and the resultant prediction for the next 150 ka. This shows a gradual cooling to a glacial maximum at 60 ka ap, followed by a significant deglaciation.

$$\hat{\phi}_3(X_3) = \begin{cases} X_3 < 2.131 & : \quad -0.883 \times X_3 + 1.381 \\ 2.131 \leq X_3 < 2.18 & : \quad -10.09 \times X_3 + 21 \\ X_3 \geq 2.18 & : \quad -1 \end{cases}$$

$$\hat{\phi}_4(X_4) = 0$$

$$\log_{10}(Y + 5) = (\sum_{i=1}^{4} \hat{\phi}_i(X_i) + 7.273)/10.4375$$

The model, even with these piece-wise linear approximations, still reproduces the past climate well, capturing the scale of glacial variation and the rapidity of the deglaciations. There is a slight problem at MIS 3 and 4, where the obliquity forcing is stronger in our model than that evident in the climate record. We observe that, as before, the model expects the Earth to be already cooling before the present day.

In the future we see a general cooling to around 25 ka ap, followed by a period of more temperate climate, and then a glacial maximum at 60 ka ap. This is then followed by a deglaciation. Figure 6 also shows that once again, this deglaciation is forced by obliquity and precession.

5.8.2 Loess

The approximated transforms are shown in Figure 5.25. We model precession as linear. Eccentricity is taken to be constant up to a threshold at 0.000926 (e=0.0304) and then linear. Obliquity is treated as being 3 linear sections with thresholds at 0.9 and 1.535. We ignore the insolation term as insignificant.

The model, with Y representing Loess, is:

$$\hat{\phi}_1(X_1) = 0.4085 \times X_1 - 0.454$$

$$\hat{\phi}_2(X_2) = \begin{cases} X_2 < 0.000926 & : \quad -0.5 \\ X_2 \geq 0.000926 & : \quad 1578.8 \times X_2 - 1.962 \end{cases}$$

$$\hat{\phi}_3(X_3) = \begin{cases} X_3 < 0.9 & : \quad -0.4 \\ 0.9 \leq X_3 < 1.535 & : \quad 0.46 \times X_3 - 0.814 \\ X_3 \geq 1.535 & : \quad 1.17 \times X_3 - 1.9 \end{cases}$$

$$\hat{\phi}_4(X_4) = 0$$

$$\log_e(Y + 5) = (\sum_{i=1}^{4} \hat{\phi}_i(X_i) + 7.11)/1.665$$

The prediction (Figure 5.26) shows a cooling for the next 5ka, another cool minimum at 23 ka ap, and then again at 60 ka ap. The behaviour for the next

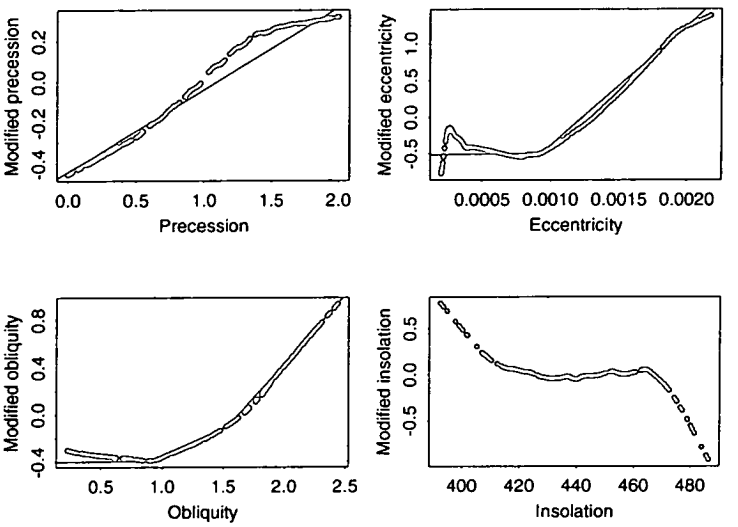

Figure 5.25. The piece-wise linear approximations of the Loess transformations.

150 ka contains values as high as those for the Holocene, but not as high as those for the preceeding two interglacials. The eccentricity contribution is constant up until 140 ka ap, so all behaviour until then is from precession and obliquity, with obliquity dominating.

5.8.3 ODP 677

The transforms are in Figure 5.27. Precession is linear up to 1.26, and then constant. Obliquity is three linear segments, and we choose to ignore the insolation term as its standard deviation is less than a fifth of any other variable. Eccentricity is very similar to SPECMAP in that initially it was characterised as three linear segments, but again the low eccentricity values gave problems, and the future prediction was considered excessively cold (conditions more extreme than the LGM in less than 8 ka ap). The three linear segments were retained, but values of eccentricity less than 0.000449 were given value zero.

The model with Y representing ODP 677, is:

$$\hat{\phi}_1(X_1) = \begin{cases} X_1 < 1.26 & : \quad -0.544 \times X_1 + 0.4614 \\ X_1 \geq 1.26 & : \quad -0.224 \end{cases}$$

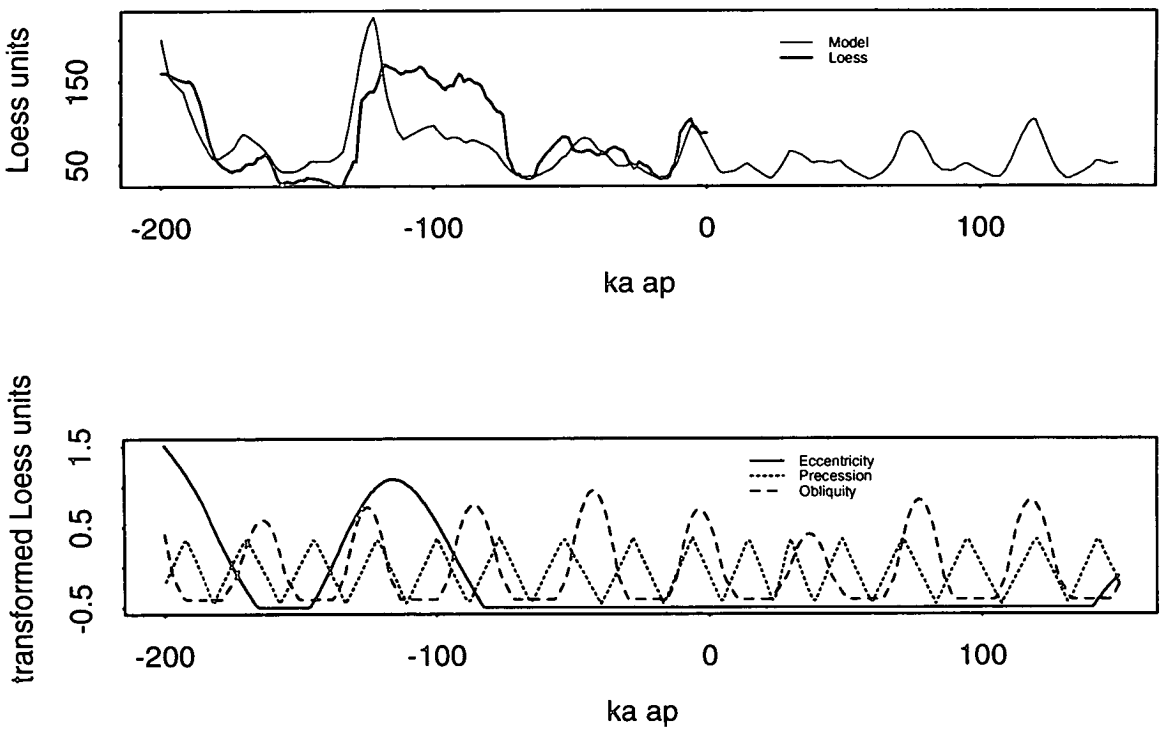

Figure 5.26. The Loess model fit for the last 200 ka, using the linear transform approximations and the resultant prediction for the next 150 ka.

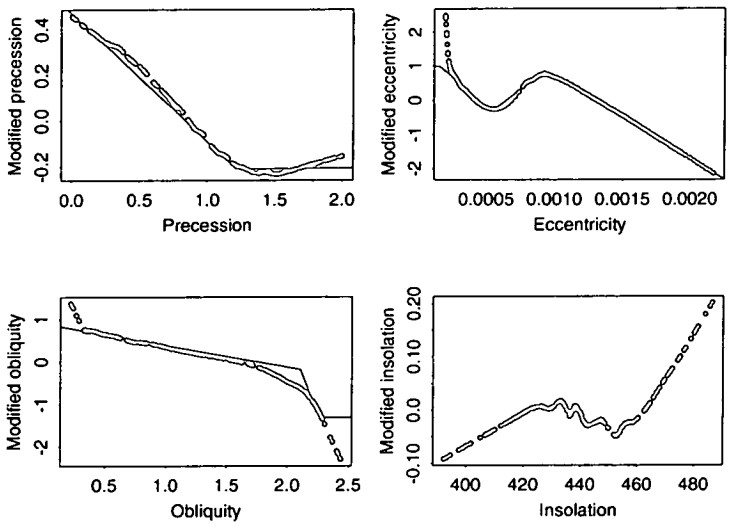

Figure 5.27. The piece-wise linear approximations of the ODP 677 transformations.

$$\hat{\phi}_2(X_2) = \begin{cases} X_2 < 0.000449 & : \quad 0 \\ 0.000449 \leq X_2 < 0.00055 & : \quad -3451 \times X_2 + 1.55 \\ 0.00055 \leq X_2 < 0.000926 & : \quad 3287 \times X_2 - 2.15 \\ X_2 \geq 0.000926 & : \quad -2398.8 \times X_2 + 3.1 \end{cases}$$

$$\hat{\phi}_3(X_3) = \begin{cases} X_3 < 2.095 & : \quad -0.625 \times X_3 + 1.08 \\ 2.095 \leq X_3 < 2.29 & : \quad -5.95 \times X_3 + 12.24 \\ X_3 \geq 2.29 & : \quad -1.39 \end{cases}$$

$$\hat{\phi}_4(X_4) = 0$$

$$\log_e(Y) = (\textstyle\sum_{i=1}^{4} \hat{\phi}_i(X_i) + 15.1)/10.04$$

Figure 5.28 shows the model again cooling from 4 ka bp. The next glacial maximum is at 59 ka ap, followed by a large deglaciation. The deglaciation arises due to the combination of obliquity and precession.

5.8.4 Devil's Hole

The precession transform was described by three linear sections (Figure 5.29), obliquity by three, and insolation was ignored. The eccentricity term was linear for values above 0.00079, and constant for values below this, thus removing the problems experienced earlier with the low eccentricity values.

The model with Y representing Devil's Hole, is:

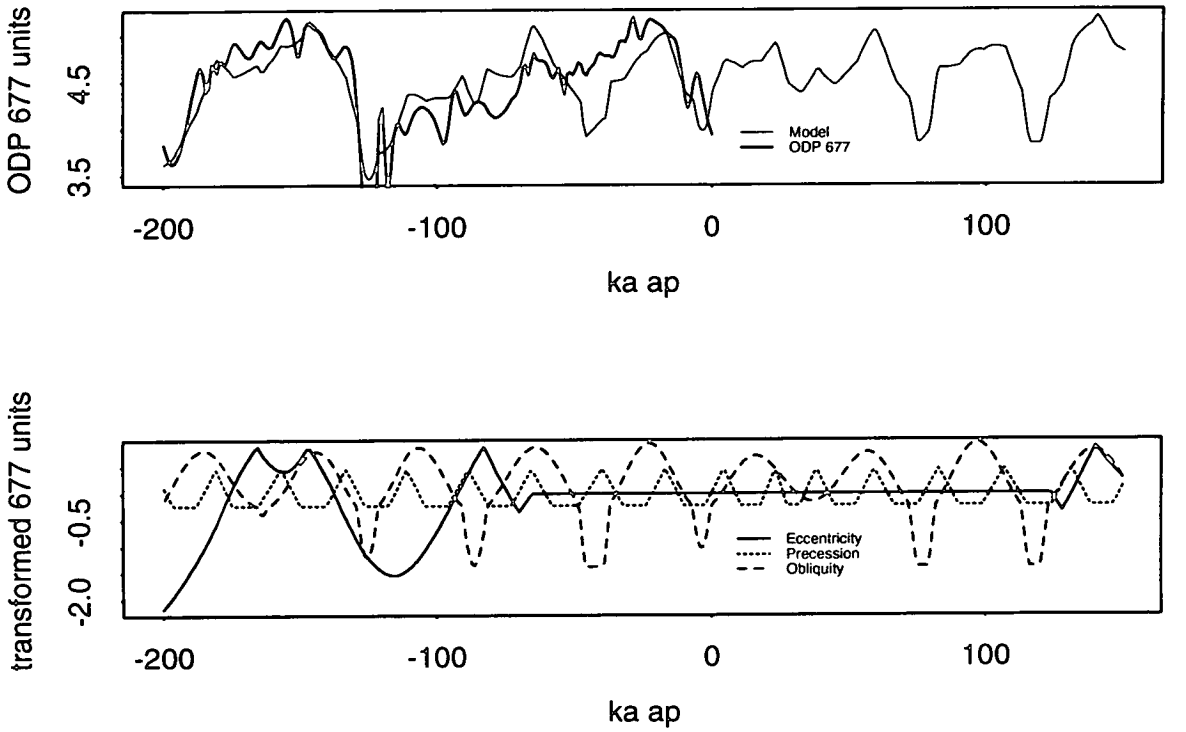

Figure 5.28. The ODP 677 model fit for the last 200 ka, using the linear transform approximations and the resultant prediction for the next 150 ka.

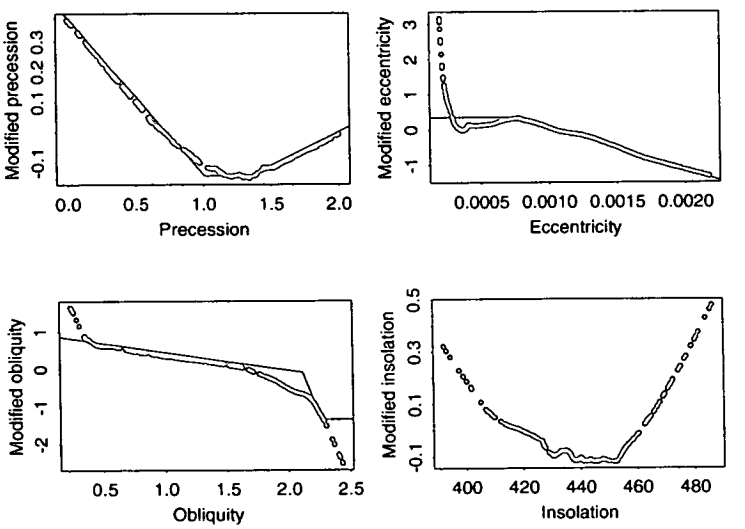

Figure 5.29. The piece-wise linear approximations of the Devil's Hole transformations.

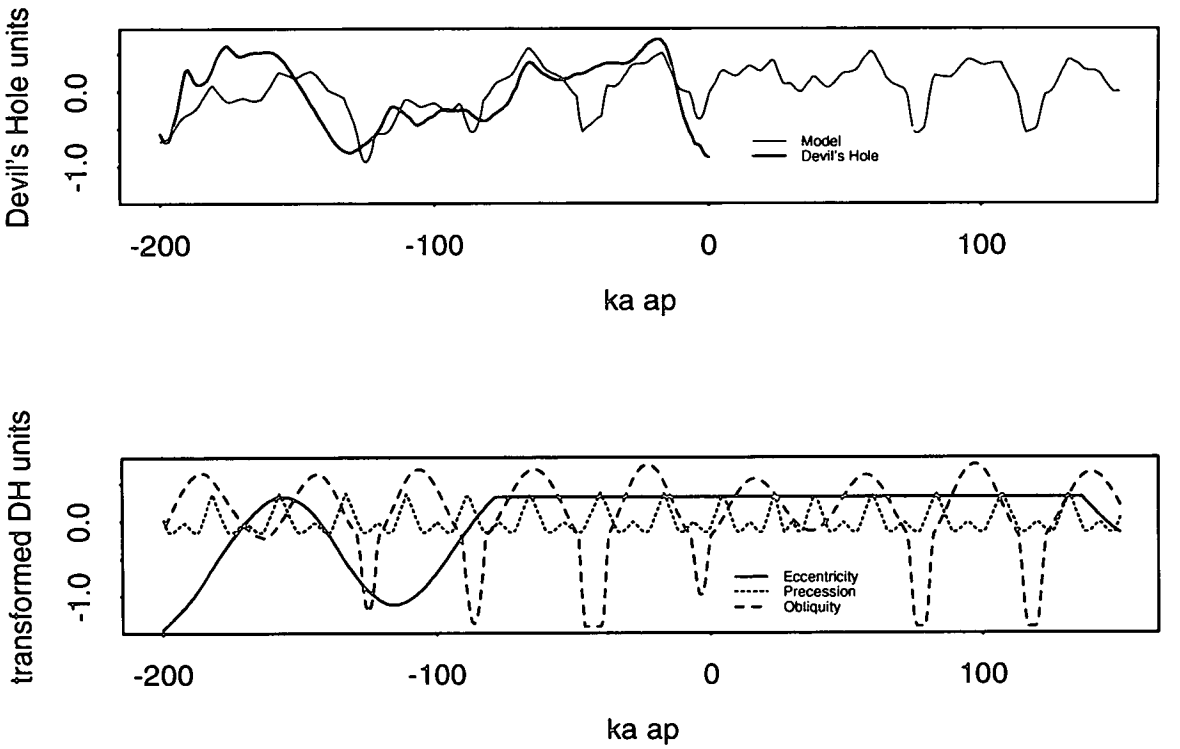

Figure 5.30. The Devil's Hole model fit for the last 200 ka, using the linear transform approximations and the resultant prediction for the next 150 ka.

$$\hat{\phi}_1(X_1) = \begin{cases} X_1 < 1 & : \quad -0.53 \times X_1 + 0.376 \\ 1 \leq X_1 < 1.33 & : \quad -0.154 \\ X_1 \geq 1.33 & : \quad 0.21 \times X_1 - 0.43 \end{cases}$$

$$\hat{\phi}_2(X_2) = \begin{cases} X_2 < 0.00079 & : \quad 0.32 \\ X_2 \geq 0.00079 & : \quad -1251.7 \times X_2 + 1.309 \end{cases}$$

$$\hat{\phi}_3(X_3) = \begin{cases} X_3 < 2.12 & : \quad -0.506 \times X_3 + 0.863 \\ 2.12 \leq X_3 < 2.29 & : \quad -7.06 \times X_3 + 14.76 \\ X_3 \geq 2.29 & : \quad -1.41 \end{cases}$$

$$\hat{\phi}_4(X_4) = 0$$

$$\log_e(Y + 5) = (\textstyle\sum_{i=1}^{4} \hat{\phi}_i(X_i) + 18.105)/11.306$$

The behaviour for the future is very similar to those described above, with the glacial maximum at 60 ka ap. However, the magnitude of the Holocene, or any subsequent interglacials, appears to be restricted by the model. Also, obliquity is again too strong during the stage 3 warming.

5.8.5 Summary

For each of the data sets we have characterised the transformations by linear segments. In each case we still model the last 200 ka well, and capture the general behaviour. The future climate behaviour is similar for each of the models. We see a cooling for the next 5/6 ka, another cool maximum at 24/25 ka ap, and then an apparent glacial maximum at around 59/60 ka ap, followed by a deglaciation.

5.9 Summary and Conclusions

Nonlinear Transformation Regression has two main potential benefits in this area of palaeoclimatology. Firstly, the smoothed scatter plots give us a visual description of the contribution of each variable, and can suggest transformations, including threshold values, which we can then try to explain in a physical sense. Secondly, it represents an excellent method for statistical prediction. Care is needed when interpreting the transformations, and we have shown the importance of understanding their physical significance before blindly accepting their behaviour.

A comparison of the ACE and AVAS methods has shown that it is reasonable to concentrate on AVAS. This is due to its improved theoretical benefits and was

highlighted by analysis of a synthetic time series and a real data set.

Analysis of the different climate records has shown that the deglaciations are generally characterised by periods of increasing obliquity and perihelion approaching the vernal equinox. When the perihelion is close to the vernal equinox this will increase the insolation being received during the Northern hemisphere autumn, and therefore lead to an extended summer. This may provide the necessary pulse to start the collapse of the ice-sheets, a process with a strong positive feedback.

We conclude that obliquity and precession, and not eccentricity, are responsible for the Earth's succession of interglacials and therefore the predominant 100 ka period in the climate records. For example, note that the timing between the pre-Eemian and pre-Holocene deglaciations is approximately 120 ka, and is three obliquity cycles. This conclusion corresponds well with the observation in Section 3.6.3 that the deglaciations correspond with periods of stronger 41 ka variation.

The future climate predictions show a general cooling for the next 5ka, followed by a slightly milder period, another cold period around 25 ka ap, a milder period from 30 to 50 ka ap, and then the glacial maximum at 60 ka ap and the subsequent deglaciation.

The application of AVAS to palaeoclimate reconstruction in this chapter has been very succesful. However, we would like to investigate the interactions between these regression variables, e.g. the combination of obliquity and precession precipitating the deglaciations. In Chapter 6 we will exploit the Generalised Additive Model technique, which will enable us to explore these interactions.

Chapter 6

Interaction Models

6.1 Introduction

In Chapter 5 it was concluded that the interaction between precession and obliquity was the dominant forcing behind the deglaciations. In this chapter we investigate another nonlinear regression technique which will allow us to visualise the interactions between these and other regression variables. The other main difference from the previous chapter is that these models do not include a transformation of the response variable (the Θ in AVAS).

Generalised Additive Models (GAM) are related to additive models in the same way as Generalised Linear Models (GLM) are to regression models. In GAM or GLM the predictor effects are assumed to be linear in the parameters, but the response distribution and the link between this distribution and the predictors can be general. GAM replace the linear form $\alpha + \sum_j \beta_j X_j$ with the additive form $\alpha + \sum_j f_j(X_j)$.

Time does not permit a full description of the GAM technique, and we refer the reader to Hastie and Tibshirani (1990) for full theoretical details.

6.2 Generalised Linear Models

There follows a brief outline of Generalised Linear Models as an introduction to the theory of Generalised Additive Models. We follow the definitions and notation of Hastie and Tibshirani (1990).

A GLM consists of a random component, a systematic component, and a link

function. It assumes that the response Y has exponential family density

$$\rho_Y(y;\Theta;\phi) = \exp\left\{\frac{y\Theta - b(\Theta)}{a(\phi)} + c(y,\phi)\right\} \tag{6.1}$$

where Θ is the natural parameter and ϕ is the dispersion parameter. This represents the random component of the model. The model also assumes that E(Y), denoted μ, is related to the covariates $X_1, ..., X_p$ by $g(\mu) = \eta$, where $\eta = \alpha + \beta_1 X_1 + \ldots + \beta_p X_p$. The parameter η is the systematic component, also known as the linear predictor, and $g(\cdot)$ is the link function.

6.3 Generalised Additive Models

In a GAM we assume that the response Y is distributed as in Equation 6.1, and that the mean $\mu = E(Y|X_1, ..., X_p)$ is linked to the predictors via

$$g(\mu) = \alpha + \sum_{j=1}^{p} f_j(X_j). \tag{6.2}$$

The α and $f_1, ..., f_p$ are estimated by replacing the weighted linear regression of GLMs by a weighted additive model algorithm. This is achieved by utilising the local scoring procedure (Hastie and Tibshirani 1990). Although Equation 6.2 contains only univariate terms this restriction is avoidable. Use of multivariate regression methods, such as surface smoothers, can allow the inclusion of interaction terms.

6.4 Comparison with AVAS

The motivation for this chapter is to exploit the interaction capabilities of GAM. However, before this we provide a comparison of the results of GAM and AVAS.

The most succesful AVAS analysis of the SPECMAP record used the four regression variables listed on Page 107. These four variables, and the SPECMAP record of the last 200 ka as response, gave the results shown in Figure 6.1. The transformations from the AVAS and GAM analyses are very similar, and this is a reassuring indication of the robustness of the two algorithms.

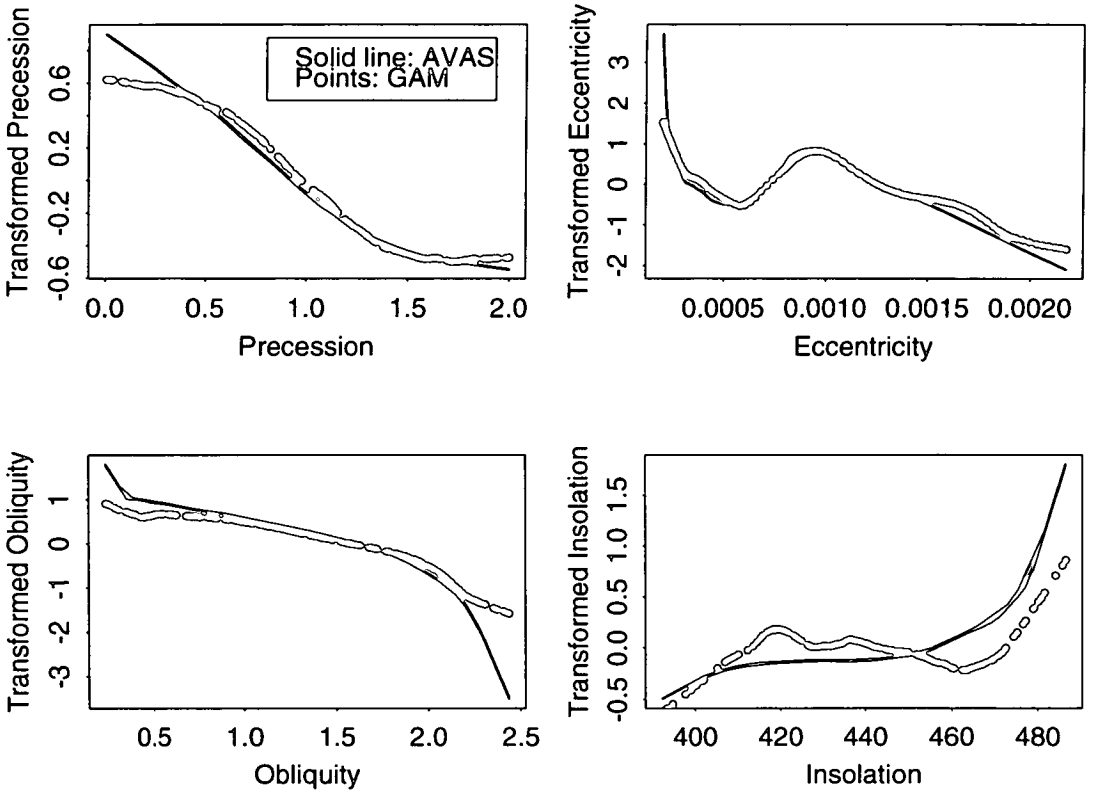

Figure 6.1. A comparison of the GAM and AVAS transformations. Regression variables are precession, lagged obliquity, eccentricity, and insolation, and the response variable is SPECMAP for the last 200 ka. The transforms for Precession, Eccentricity and Obliquity are very similar. The insolation transform shows more inconsistency between the models, but both transforms are predominantly around zero, and our analyses using AVAS confirmed the unreliability of the insolation variable.

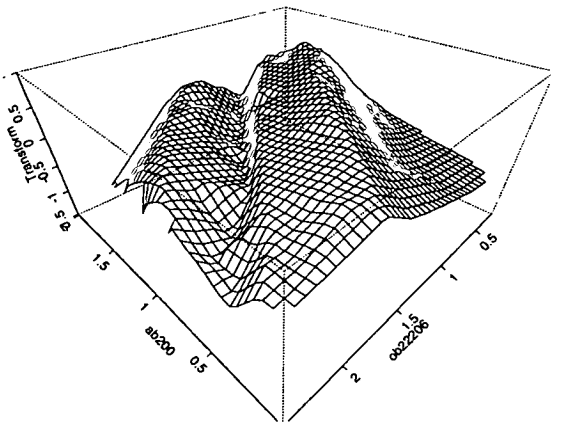

Figure 6.2. An example persp plot.

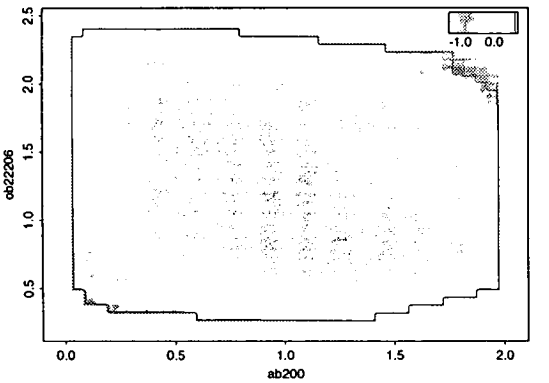

Figure 6.3. An example image plot.

6.5 Displaying the Interactions

S-Plus has three techniques for displaying data in three dimensions. These are:

persp: A perspective plot of the surface;

image: A grey-scale image;

contour: A contour plot of the data.

Figures 6.2, 6.3, and 6.4 show examples of these for the same sample data set. We will generally use persp as it provides the clearest visualisation of the transform surface.

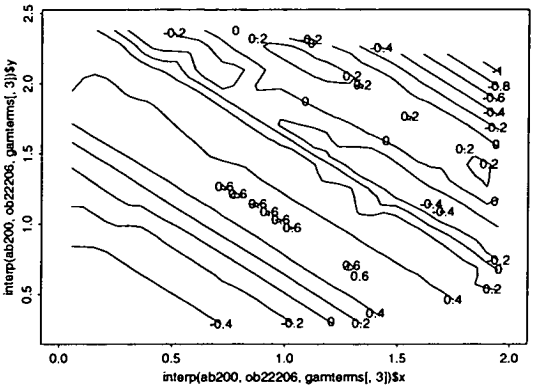

Figure 6.4. An example contour plot.

6.6 Results

The number of possible combinations of regression variables is greatly increased by including interactions. We limit discussion here to those sets of regressors that yielded informative or interesting results. All analyses are of the SPECMAP record for the last 200 ka.

For simplicity, the regression variables are labelled as follows:

- X_1 : precession variable ($|\omega - 180|/90$);
- X_2 : eccentricity (e);
- X_3 : squared eccentricity (e^2);
- X_4 : obliquity ($\epsilon - 22$);
- X_5 : obliquity, lagged 6 ka ($\epsilon - 22$);
- X_6 : insolation at 65°N during July;

and $*$ is used to indicate an interaction term e.g. $X_1 * X_3$.

6.6.1 Interactions Between Precession and Obliquity

This is the main combination of interest, as AVAS has shown that the combination of precession and obliquity has a strong effect on climate change.

As these two variables have such importance, an analysis is carried out using only precession, obliquity, and their interaction (X_1, X_4, and $X_1 * X_4$). A plot of the fit of the model is shown in Figure 6.5. The fitted model has no ice

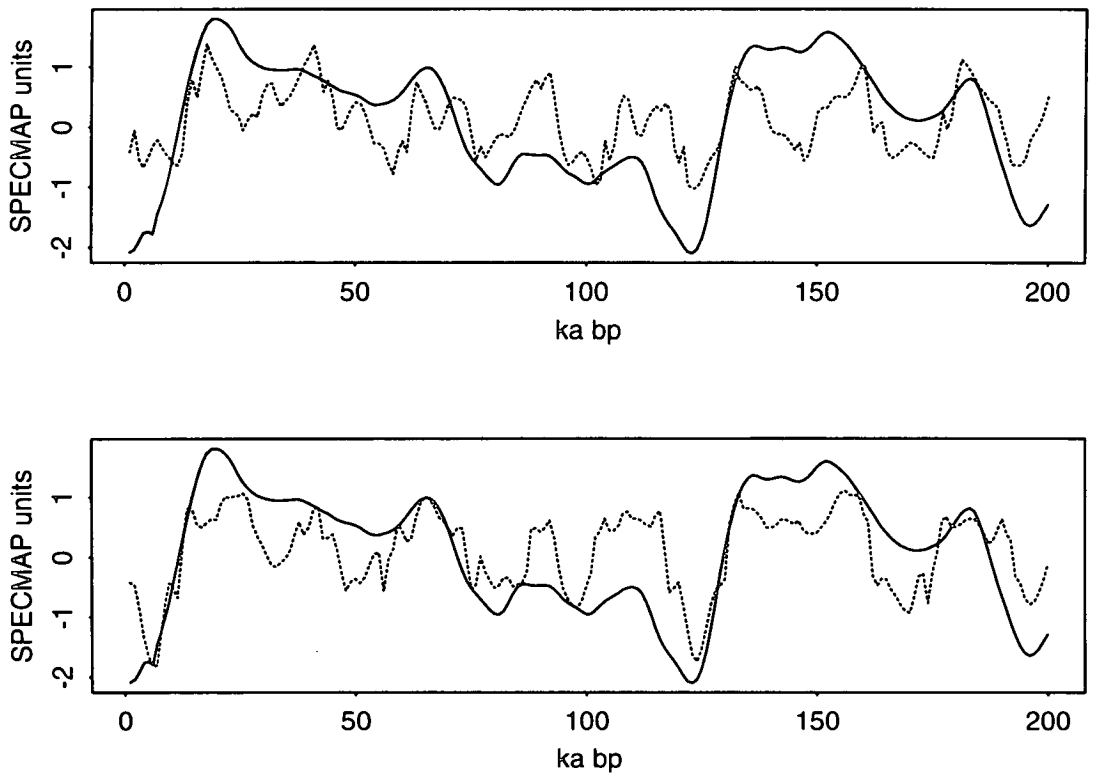

Figure 6.5. Top: Fit of model with $X_1 * X_4$,X_1 and X_4 as regressors. Bottom: Fit of model with $X_1 * X_5$, X_1 and X_5 as regressors. Solid line is SPECMAP. Analysis using the unlagged obliquity variable (top) shows no glacial/interglacial variations. However, the analysis including obliquity lagged 6 ka (bottom) displays strong interglacials at the correct times.

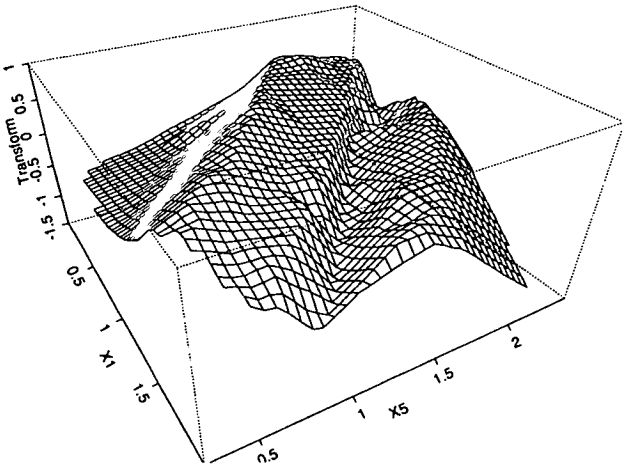

Figure 6.6. Interaction surface of $X_1 * X_5$ with X_1 and X_5 as additional regressors.

age behaviour. This analysis is then repeated, but with the obliquity variable (X_4) replaced with the lagged obliquity variable (X_5). This model fit (Figure 6.5) does not reproduce the ice ages, but does have pronounced interglacials, again highlighting the combined warming effect of obliquity and precession. The interaction surface for X_1 and X_5 is shown in Figure 6.6. As expected, Figure 6.6 has the strongest warming produced by high obliquity and the precession variable near 2 (autumnal perihelion). However, there is also an unexpected slight warming for low obliquity and vernal equinox. As with many of the precession against obliquity plots, the graph is approximately symmetric about $y = x$.

Addition of eccentricity (X_2) yields the transformations shown in Figure 6.7. The precession, obliquity, and eccentricity transforms are very similar to those from the corresponding AVAS analysis (excluding the interaction term).

6.6.2 Interactions Including a Time Variable

The addition of a "time" variable (in these examples, a vector of integers from 1-200) gives GAM the ability to create another variable. This may represent a missing variable, or be representative of some internal processes. We refer to time as X_7.

Figure 6.8 shows the transformations, fit, and the individual contributions to the GAM model with precession, lagged obliquity, and time (X_1, X_5, and X_7). The striking features here are the simplicity of the transforms and the goodness of fit. The time variable has accounted for the overall shape of the glacial cycle,

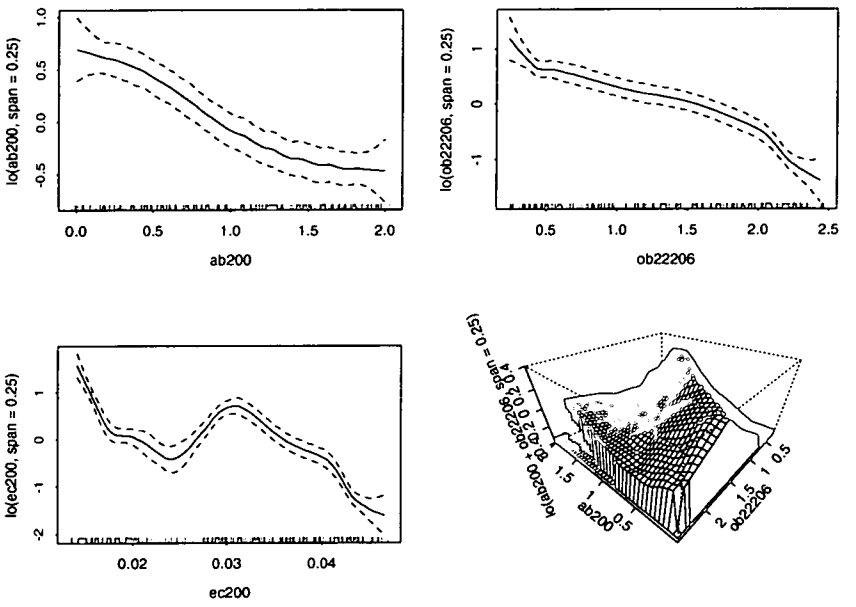

Figure 6.7. Transformations for X_1, X_5, X_2, and $X_1 * X_5$. Includes standard error estimates for the univariate regressors.

and precession and (lagged) obliquity can account for all the deviations from this

.

Figure 6.9 shows the transformations, fit, and the individual contributions to the GAM model with only time and the interaction of precession adn lagged obliquity ($X_1 * X_5$ and X_7). Once again, the time variable accounts for the glacial cycle, and the precession/obliquity interaction provides the detail on top of this. The behaviour of the interaction is very straightforward: as precession and obliquity increase so does the warming effect.

The time variable has provided the basic 100 ka template ontop of which obliquity and precession imposed the higher frequency behaviour. If eccentricity is the cause of ice age variations then it should behave similarly to time. However, Figure 6.10 shows that whilst the precession/obliquity transformation is very similar, eccentricity cannot help the interaction term to achieve full interglacial values in the Holocene. The interaction variables do provide considerable warming around the time of the last deglaciation, but this is not sufficient to produce full interglacial values.

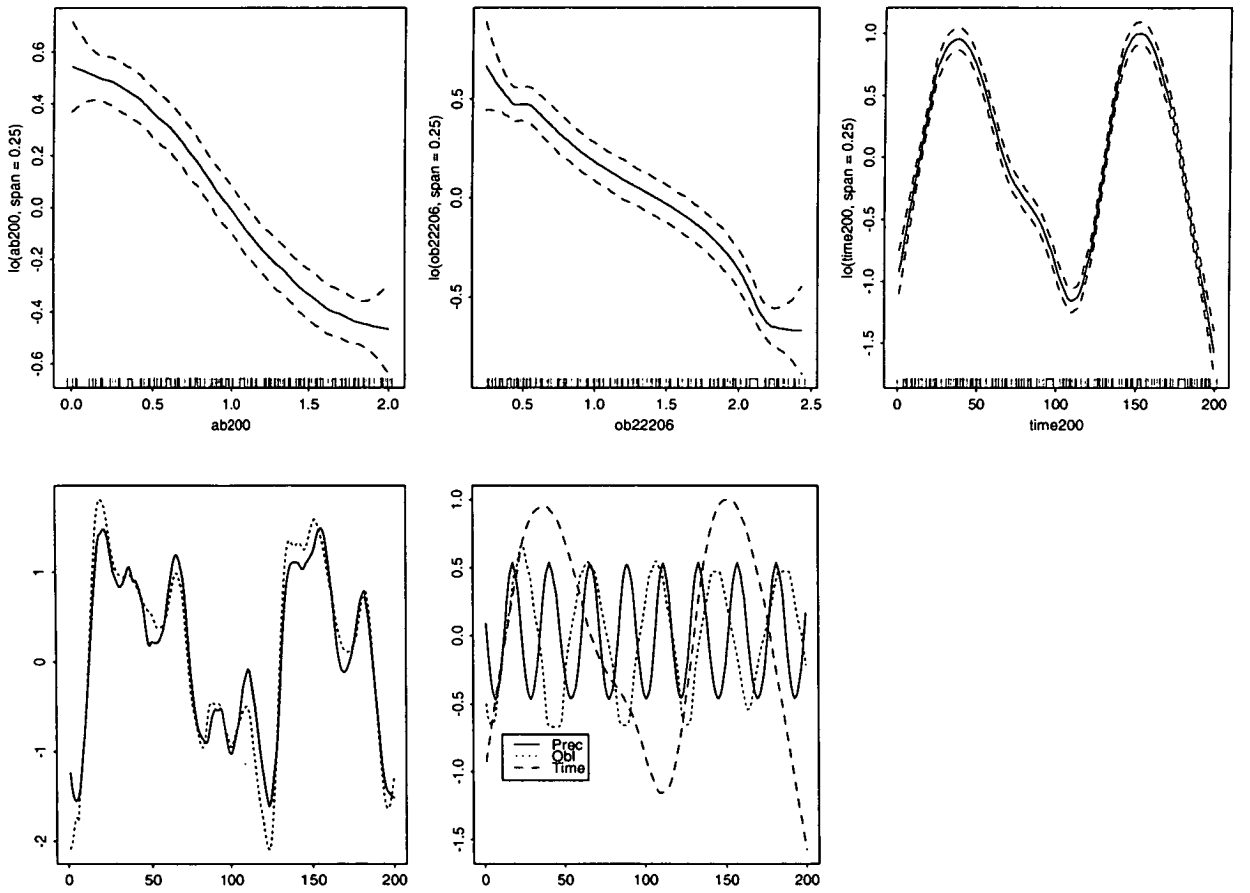

Figure 6.8. Top: Transformations for X_1, X_5, and X_7. Bottom: The model fit, and the contributions to the model. In this example the time variable (X_7) provides the 100 ka variation, on top of which precession and obliquity superimpose the more detailed behaviour.

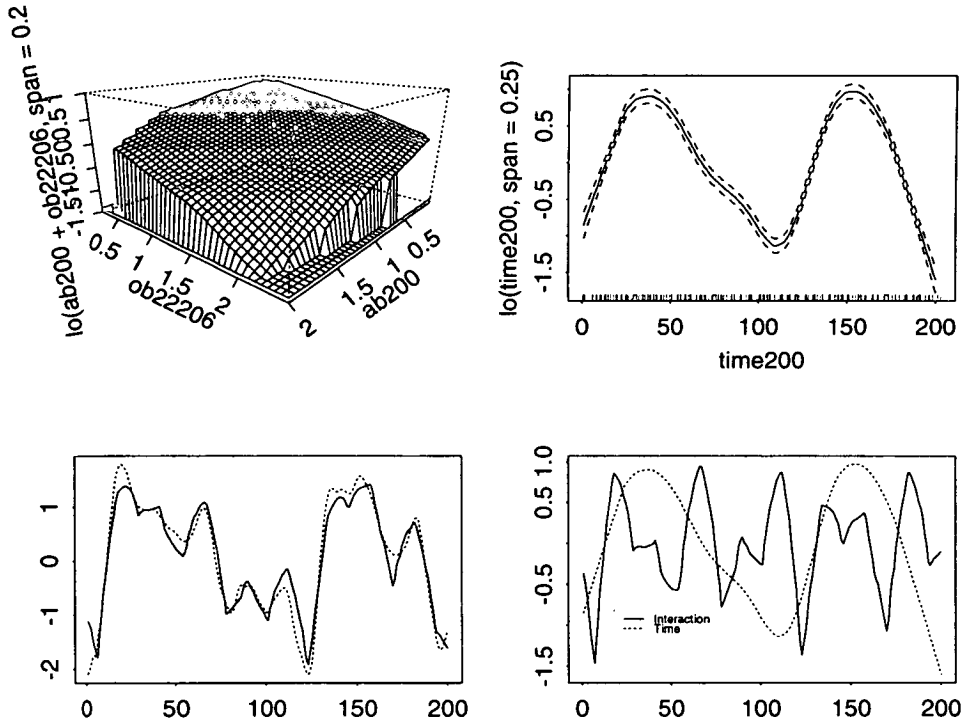

Figure 6.9. Top: Transformations for $X_1 * X_5$, and X_7. Bottom: The model fit, and the contributions to the model. The time variable provides the 100 ka variation, and then the interaction term provides the higher frequency variations. The interaction term is an approximate plane in 3D, with increasing obliquity and precession both implying a warmer climate.

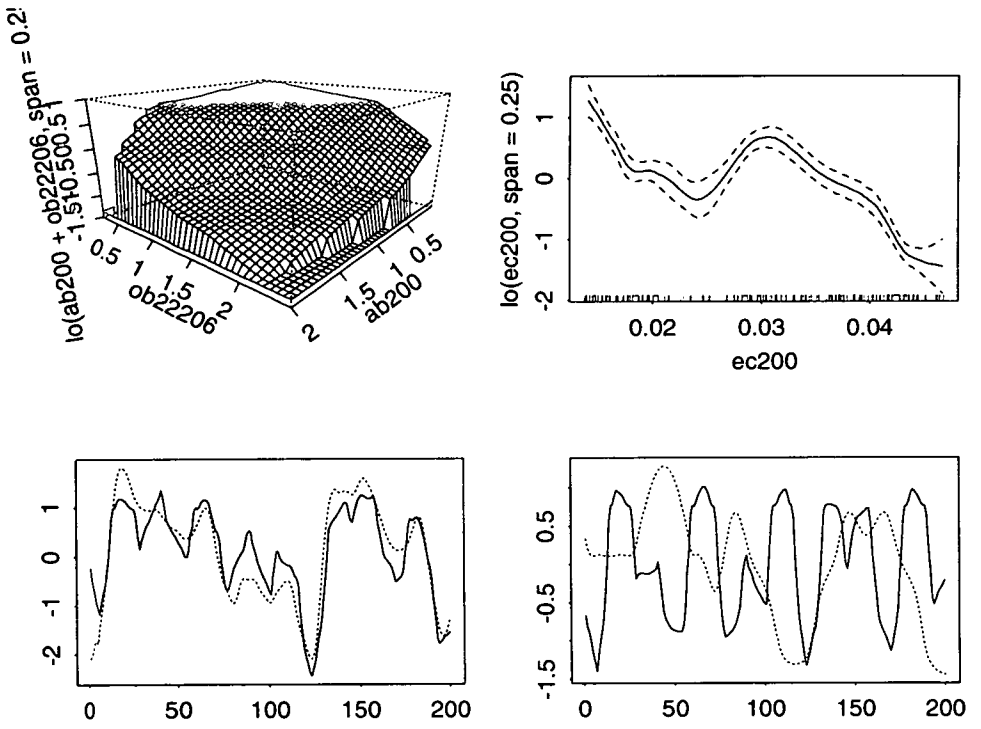

Figure 6.10. Top: Transformations for $X_1 * X_5$, and X_2. Bottom: The model fit, and the contributions to the model. Unlike Figure 6.9, the eccentricity term cannot provide the glacial variations onto which precession and obliquity can impose the higher frequency behaviour. In particular, the LGM and present interglacial are not fully reproduced.

6.7 Summary and Conclusions

In this chapter we have applied the technique of Generalised Additive Models in order to examine the interactions between the orbital variables. Initial tests confirmed the consistency of results from the GAM and AVAS techniques, so that direct comparisons with the previous chapter are possible.

The results have confirmed the cumulative warming effect of precession and obliquity and the importance of precession and obliquity in the deglaciations. Using only precession, obliquity, and an interaction of these two variables it is possible to produce the past interglacials, though not the glacial maxima.

By introducing a time variable we hoped to characterise any missing elements in our models. In situations where the time variable contributes the smooth 100 ka variation, then precession and obliquity can produce all the variations about this longer term behaviour. Replacing the time variable with eccentricity fails to produce the LGM and Holocene temperatures, again providing further evidence that eccentricity is not a direct driver of the deglaciations.

Chapter 7

Summary and Conclusions

7.1 Summary

This thesis contains the following sections.

- An introduction to the climatological, geological, astronomical and statistical theory necessary to understand the scientific field of palaeoclimate analysis.
- A review of the past applications of statistical analysis to palaeoclimatic data, including comments on their assumptions and limitations.
- A discussion of the different spectral algorithms which have been used to discover the periodicities present in the time series.
- The Complex Demodulation technique has been introduced, its application described, and the results interpreted.
- A variety of linear models have been applied to various time series in order to explore the limitations of these models.
- Various climate records have been hindcast by utilising linear models based transformation of a longer, representative time series.
- A comparison of the AVAS and ACE multivariate nonlinear regression techniques.
- A guide to the theory, application and interpretation of the AVAS technique.

- The application of AVAS to four long palaeoclimatic records, culminating in predictions of the next 150 ka based on the behaviour during the last 200 ka.
- An introduction to Generalised Additive Models.
- The application of GAM to the SPECMAP time series, including 3D contour plots of the interactions between the orbital variables.

7.2 Conclusions

We have divided the conclusions into three sections. The first deals with the overall conclusions about the forcing of the Earth's 100 ka ice age cycle. The second section discusses statistical/methodological conclusions, and the third section details the results which have implications for particular palaeoclimatic time series.

7.2.1 The 100 ka Ice Age Cycle

Using the AVAS and GAM techniques it has been possible to model the past climatic variations, including the scale of the glacial/interglacial variations, and the rapidity of the deglaciations. This led to the folowing conclusions:

- As with previous palaeoclimate analyses we conclude that the effect of precession variations is linear, and that the slope of this linear model (and therefore its importance) varies with eccentricity. The linear model has the warmest periods coinciding with perihelion near the vernal equinox.
- The obliquity variations also have an approximately linear effect, though with some indication of a stronger warming for high values.
- The role of eccentricity is more difficult to interpret, although high eccentricity is consistently associated with warmer climate (due to the lower average Earth-Sun distance at these times).
- The deglaciations appear to occur due to the coinciding of precession and obliquity induced warming during a period of high glaciation. This suggests no direct role for eccentricity in the ice age cycle, and this conclusion is supported by the lack of correlation between the amplitude analyses from Complex Demodulation. Complex Demodulation also has the deglaciations

corresponding with periods of strong 41 ka variation in the data, further evidence for the obliquity forcing of deglaciations.

- Future climate predictions show a cooling for the next 5/6 ka, then a slight warming, a cooler period around 24/25 ka ap, and then a glacial maximum at 59/60 ka ap.

A possible scenario for the driving of the Earth's 100 ka ice age cycle can therefore be summarised as follows:

- The Earth naturally accumulates ice;
- After a period of ice accumulation an internal threshold or positive feedback mechanism is activated, leading to a glacial collapse. Possible mechanisms for this are the internal dynamics of the great ice sheets, or positive feedback due to the expansion of the mid-latitude forests;
- The timing of the subsequent glacial collapse is triggered by the warming pulse which results from high obliquity and autumnal perihelion, possibly due to the extended summer experienced in the Northern hemisphere during such an orbital configuration.

7.2.2 The Methodologies

- Complex Demodulation can provide information which is lost in a spectral analysis, and has obvious applications in the field of palaeoclimatology. It can also be of benefit in analysing the time scale of a time series.
- Linear techniques have proven unable to reproduce past climatic variations when using only orbital/insolation variations as input.
- Linear techniques are useful when we wish to hindcast shorter palaeoclimate records by using them in conjunction with longer palaeoclimate time series.
- The AVAS technique has rendered the ACE technique redundant for this application.
- AVAS has great potential in this, and many other areas of the physical sciences, due to its relatively simple application and interpretation.
- The GAM technique has provided 3-D plots of regression variable interactions.

7.2.3 Data Implications

These are mainly from the Complex Demodulation analyses.

- The SPECMAP record 23 ka cycle shows strong similarity with the eccentricity modulated insolation variations at this frequency. Also, the phase behaviour of the 41 ka periodicity highlights the dating error at around 617 ka bp.
- Loess record also shows good correspondence between data and insolation in the 23 ka amplitude variations. The frequency change of the 41 ka cycle (also apparent in the original spectral analyses) may be indicative of a systematic dating error.
- The Devil's Hole 23 ka analysis suggests that the dating of the record at the stage 5/6 deglaciation may be incorrect.

7.3 Future Work

It would be very interesting to apply AVAS and Complex Demodulation to a longer palaeoclimatic record, in particular one which extends back to before 2.5 Ma bp and therefore encompasses periods when the dominant period in climate has been 23, 41, and then 100 ka. This would provide an insight into the changing response to orbital forcing.

The fields of palaeoclimatology and statistics are enormous, and yet presently have a very small overlap. In general, palaeoclimatologists have a set suite of statistical techniques (spectral and cross-spectral techniques, band-pass filtering etc.) which they apply to their data. Whilst we acknowledge the enormous contribution made by these techniques over the last 25 years, there are numerous other techniques which could provide further information on the climatic time series. Therefore, the field would benefit from a greater level of interaction between statisticians and climatologists.

The obvious drawback with much of this thesis is its inability to react to any greenhouse gas induced climate changes. For example, will "global warming" reduce the extent of the Greenland and Antarctic ice sheets in the short term and therefore delay the next glacial maximum? To model this requires a greater understanding of the underlying physical mechanisms, and this is the approach which has been adopted by General Circulation Models (GCM). GCMs have a

major role to play in future climate predictions. However, their computational complexity necessitates a restrictively high CPU requirement, and they cannot yet achieve time dependent runs over geological time scales. The combined use of GCMs and time series techniques can perhaps help overcome this.

Appendix A

Time Series Predictions

This appendix contains the predictions of the four main time series analysed in this thesis, namely the SPECMAP, Devil's Hole, and ODP 677 oxygen isotope records, and the magnetic susceptibility record from the Chinese Loess. The predictions for the next 150 ka are those calculated using the AVAS technique in Section 5.8.

20:02:11 **appen1sp.txt** Page 1

	SPECMAP						
	ka ap	data	ka ap	data	ka ap	data	
3	150	1.20847	100	1.33898		50	-0.10899
4	149	1.238567	99	1.240437		49	-0.06476
5	148	1.270512	98	1.110775		48	-0.07594
6	147	1.299906	97	0.951183		47	-0.02685
7	146	1.32544	96	0.762927		46	-0.07788
8	145	1.341579	95	0.5502		45	-0.11815
9	144	1.345183	94	0.516665		44	-0.04946
10	143	1.333543	93	0.573831		43	0.027509
11	142	1.443852	92	0.609235		42	0.117499
12	141	1.799883	91	0.624753		41	0.221259
13	140	2.151919	90	0.625378		40	0.342282
14	139	2.468733	89	0.614172		39	0.485102
15	138	2.44135	88	0.59764		38	0.467834
16	137	2.385479	87	0.57779		37	0.472746
17	136	2.302056	86	0.56105		36	0.394037
18	135	2.194234	85	0.551612		35	-0.06565
19	134	2.066485	84	0.552576		34	-0.21371
20	133	1.925624	83	0.563559		33	-0.35362
21	132	1.773365	82	0.281671		32	-0.48617
22	131	1.48237	81	-0.34097		31	-0.61815
23	130	0.95362	80	-0.58652		30	-0.75152
24	129	0.469817	79	-0.7115		29	-0.54393
25	128	0.028562	78	-0.83255		28	-0.2052
26	127	-0.3699	77	-0.94995		27	0.175532
27	126	-0.68467	76	-1.06382		26	0.585264
28	125	-0.80108	75	-1.17442		25	1.011792
29	124	-0.9101	74	-1.28177		24	1.442502
30	123	-1.01065	73	-0.99318		23	1.633234
31	122	-1.31784	72	-1.00313		22	1.463453
32	121	-1.51363	71	-0.99115		21	1.302588
33	120	-1.54335	70	-0.76981		20	1.140605
34	119	-1.50411	69	-0.528		19	0.975318
35	118	-1.40671	68	-0.2663		18	0.80175
36	117	-1.3075	67	0.01245		17	0.619722
37	116	-1.20627	66	0.308313		16	0.42722
38	115	-1.10307	65	0.616028		15	0.225036
39	114	-0.94046	64	0.932292		14	0.192407
40	113	-0.37013	63	1.253033		13	0.322253
41	112	-0.14509	62	1.573126		12	0.435124
42	111	0.105403	61	1.888321		11	0.533149
43	110	0.383276	60	2.193592		10	0.615554
44	109	0.689448	59	2.218039		9	0.68502
45	108	1.021353	58	2.033793		8	0.744398
46	107	1.379192	57	1.824723		7	0.79674
47	106	1.416379	56	1.593465		6	0.84401
48	105	1.443404	55	1.344196		5	0.894219
49	104	1.462008	54	1.083022		4	0.75529
50	103	1.464437	53	0.812439		3	0.442177
51	102	1.447915	52	0.53793		2	0.157009
52	101	1.407716	51	0.264396		1	-0.10085

Table A.1. The SPECMAP prediction of the next 150 ka.

20:00:49 **appen1sh.txt** Page 1

	ODP 677						
	ka ap	data	ka ap	data	ka ap	data	
3	150	4.313444	100	4.84337	50	4.615496	
4	149	4.327317	99	4.822269	49	4.584001	
5	148	4.343267	98	4.833088	48	4.551869	
6	147	4.358671	97	4.835796	47	4.519962	
7	146	4.395601	96	4.83008	46	4.489116	
8	145	4.956964	95	4.816269	45	4.459592	
9	144	5.016445	94	4.79473	44	4.475434	
10	143	5.073335	93	4.766162	43	4.497467	
11	142	5.126584	92	4.731574	42	4.522949	
12	141	5.175594	91	4.691665	41	4.551966	
13	140	5.202622	90	4.662046	40	4.585522	
14	139	5.149978	89	4.658994	39	4.624114	
15	138	5.105412	88	4.654524	38	4.619425	
16	137	5.090819	87	4.649162	37	4.56617	
17	136	5.070062	86	4.644617	36	4.516793	
18	135	5.043721	85	4.642015	35	4.47058	
19	134	5.012654	84	4.642192	34	4.427375	
20	133	4.978275	83	4.645046	33	4.385697	
21	132	4.940849	82	4.56858	32	4.380352	
22	131	4.869942	81	4.327723	31	4.399755	
23	130	4.737464	80	4.09684	30	4.422271	
24	129	4.609126	79	3.953214	29	4.44684	
25	128	4.48524	78	3.917274	28	4.473494	
26	127	4.437898	77	3.881731	27	4.539466	
27	126	4.399604	76	3.84658	26	4.651193	
28	125	4.362156	75	3.858175	25	4.761722	
29	124	4.332048	74	4.002572	24	4.868044	
30	123	4.307075	73	4.204374	23	4.913613	
31	122	4.142543	72	4.317544	22	4.873192	
32	121	3.971854	71	4.349105	21	4.834217	
33	120	3.84904	70	4.384171	20	4.794272	
34	119	3.831388	69	4.421996	19	4.752756	
35	118	3.831388	68	4.461813	18	4.710414	
36	117	3.831388	67	4.50227	17	4.71687	
37	116	3.831388	66	4.576373	16	4.718045	
38	115	3.942034	65	4.659449	15	4.713934	
39	114	4.144133	64	4.741662	14	4.703968	
40	113	4.380609	63	4.822041	13	4.689057	
41	112	4.447488	62	4.899501	12	4.66896	
42	111	4.519497	61	4.973299	11	4.644609	
43	110	4.596621	60	5.042606	10	4.659387	
44	109	4.678526	59	5.048093	9	4.677635	
45	108	4.763996	58	5.006643	8	4.693098	
46	107	4.852624	57	4.958688	7	4.706628	
47	106	4.861721	56	4.904452	6	4.718765	
48	105	4.868332	55	4.844511	5	4.731589	
49	104	4.372898	54	4.779953	4	4.695658	
50	103	4.373561	53	4.71104	3	4.612551	
51	102	4.869656	52	4.673321	2	4.533982	
52	101	4.860012	51	4.645476	1	4.460351	
53							

Table A.2. The ODP 677 prediction of the next 150 ka.

19:56:51 **appen1de.txt** Page 1

	Devil's Hole						
	Ka ap	data	Ka ap	data	Ka ap	data	
3	150	0.300533	100	0.355365	50	0.24825	
4	149	-0.0017	99	0.370246	49	0.240685	
5	148	-0.00371	98	0.391113	48	0.203257	
6	147	0.032103	97	0.409951	47	0.158728	
7	146	0.073831	96	0.42219	46	0.115204	
8	145	0.128597	95	0.428017	45	0.0767	
9	144	0.181646	94	0.405844	44	0.054482	
10	143	0.232469	93	0.365621	43	0.060654	
11	142	0.267669	92	0.320628	42	0.089064	
12	141	0.276416	91	0.271451	41	0.12042	
13	140	0.281069	90	0.230064	40	0.155547	
14	139	0.281043	89	0.192514	39	0.194862	
15	138	0.28715	88	0.188341	38	0.191486	
16	137	0.296349	87	0.191149	37	0.140685	
17	136	0.33993	86	0.194602	36	0.091683	
18	135	0.368672	85	0.199504	35	0.045663	
19	134	0.392255	84	0.206833	34	0.001853	
20	133	0.412678	83	0.216008	33	-0.00198	
21	132	0.430092	82	0.147163	32	0.020384	
22	131	0.414692	81	-0.05737	31	0.060379	
23	130	0.337692	80	-0.32672	30	0.105087	
24	129	0.261355	79	-0.49031	29	0.108471	
25	128	0.185888	78	-0.5258	28	0.099947	
26	127	0.11228	77	-0.55699	27	0.111124	
27	126	0.041187	76	-0.55699	26	0.189142	
28	125	-0.00064	75	-0.52198	25	0.290696	
29	124	-0.02608	74	-0.3307	24	0.387842	
30	123	-0.03595	73	-0.06698	23	0.426705	
31	122	-0.14961	72	0.010229	22	0.383747	
32	121	-0.34562	71	0.047449	21	0.342582	
33	120	-0.48334	70	0.060815	20	0.301133	
34	119	-0.50962	69	0.076209	19	0.271423	
35	118	-0.5231	68	0.092954	18	0.280396	
36	117	-0.53641	67	0.111582	17	0.302001	
37	116	-0.54959	66	0.144861	16	0.323653	
38	115	-0.42646	65	0.188413	15	0.340858	
39	114	-0.22212	64	0.261292	14	0.332528	
40	113	-0.03594	63	0.332636	13	0.30026	
41	112	0.024615	62	0.401602	12	0.264064	
42	111	0.089222	61	0.46764	11	0.227256	
43	110	0.157837	60	0.530127	10	0.204146	
44	109	0.230157	59	0.533015	9	0.205644	
45	108	0.305182	58	0.492437	8	0.226235	
46	107	0.38257	57	0.446695	7	0.245279	
47	106	0.383355	56	0.39595	6	0.263205	
48	105	0.381942	55	0.340645	5	0.28168	
49	104	0.378861	54	0.287254	4	0.252888	
50	103	0.372643	53	0.27048	3	0.177916	
51	102	0.362764	52	0.258497	2	0.106538	
52	101	0.348314	51	0.254279	1	0.039112	
53							

Table A.3. The Devil's Hole prediction of the next 150 ka.

20:03:00 **appen1lo.txt** Page 1

Chinese Loess

ka ap	data	ka ap	data	ka ap	data
150	52.15398	100	41.63441	50	49.34989
149	51.62483	99	43.33671	49	53.83296
148	51.06258	98	45.12583	48	53.98612
147	50.52009	97	47.0029	47	53.15549
146	51.35653	96	48.97407	46	52.28574
145	52.38867	95	51.04322	45	51.36791
144	53.38638	94	50.45938	44	52.1251
143	54.34955	93	48.38884	43	52.92431
142	53.55754	92	46.39567	42	53.30893
141	49.80493	91	44.47611	41	53.26836
140	46.65567	90	42.63132	40	52.66807
139	44.61941	89	42.11002	39	51.54373
138	42.67085	88	42.25416	38	52.22874
137	40.80628	87	42.43511	37	55.35637
136	39.02531	86	42.58385	36	58.30593
135	37.32308	85	45.26686	35	60.26161
134	35.699	84	48.18779	34	62.04999
133	34.14931	83	50.86292	33	63.49673
132	32.95326	82	57.62478	32	64.52729
131	33.62578	81	64.3657	31	65.36794
130	36.44651	80	70.83235	30	66.03109
129	39.52583	79	76.74246	29	59.36607
128	42.87849	78	81.68664	28	52.76475
127	47.91186	77	85.54837	27	47.27559
126	54.81837	76	88.02528	26	42.37118
125	62.39229	75	89.11938	25	38.11854
124	70.49041	74	88.90054	24	34.51068
123	78.93859	73	87.38556	23	33.10276
122	87.4414	72	84.81909	22	34.63873
121	95.738	71	80.39088	21	36.74061
120	103.4676	70	70.45154	20	38.87453
119	104.1827	69	61.34347	19	41.05622
118	101.1184	68	53.73976	18	43.30246
117	96.67297	67	49.51363	17	45.62431
116	91.15795	66	45.61115	16	48.03398
115	84.6643	65	42.07562	15	50.54198
114	77.55275	64	38.90018	14	50.51581
113	70.11168	63	36.79774	13	48.05101
112	62.55416	62	35.24453	12	45.72018
111	55.23211	61	33.74583	11	43.51428
110	48.29234	60	32.30029	10	42.10574
109	41.87112	59	32.5611	9	41.24136
108	37.98197	58	34.03871	8	40.70079
107	34.97201	57	35.59502	7	40.14537
106	34.70816	56	37.23365	6	39.65104
105	34.52577	55	38.95728	5	39.37036
104	35.57853	54	40.77181	4	43.48135
103	36.98782	53	42.68016	3	49.54335
102	38.46447	52	44.68757	2	56.04145
101	40.01097	51	46.79834	1	62.8424

Table A.4. The Chinese Loess prediction of the next 150 ka.

Bibliography

Adhemar, J. (1842). Revolutions de la mer, *Privately published, Paris.*

Agassiz, L. (1840). Etudes sur les glaciers, *Privately published, Neuchatel.*

Agricultural Climate of England and Wales (1984). HMSO, London.

Anolik, M., Kranisky, G. and Pius, L. (1969). Trigonometrical theory of the perturbations of major planets, *Trudy Institute Theoreticheskol Astronomii, Leningrad* 14: 1–48.

Arrhenius, G. (1952). *Swedish Deep Sea Expedition (1947-1948) Reports,5*, Elander, Goteborg.

Baksi, A., Hsu, V., McWilliams, M. and Farrer, E. (1992). Ar^{40}/Ar^{39} dating of the Brunhes-Matuyama geomagnetic field reversal, *Science* 256: 356–357.

Banks, R. (1975). Complex demodulation of geomagnetic data and the estimation of transfer functions, *Geophysical Journal of the Royal Astronomical Society* 43: 87–101.

Becker, R., Chambers, J. and Wilks, A. (1988). The New S Language.

Berger, A. (1978a). Long term variations of daily insolations and Quaternary climatic changes, *Journal of Atmospheric Sciences* 35(2): 2362–2367.

Berger, A. (1978b). A simple algorithm to compute long term variations of daily or monthly insolation, *Contribution no. 18, Universite Catholique de Louvain.*

Berger, A. and Loutre, M. (1991). Insolation values for the climate of the last 10 million years, *Quaternary Science Reviews* 10(4): 297–317.

Berger, A., Gallee, H. and Melice, J. (1991). The Earth's future climate at the astronomical timescale, *in* Goodess and Palutikof (1991b), pp. 148–165.

Berger, A., Guiot, J., Kukla, G. and Pestiaux, P. (1981). Long term variations of monthly insolation as related to climate change, *Geologischen Rundschau* 70(2): 748–758.

Berger, A., Loutre, M. and Laskar, J. (1988). Une nouvelle solution astronomique pour les 10 derniers million d'annees, *Sc. Report 1988/14, Universite Catholique de Louvain.*

Berger, A., Melice, J. and Hinnov, L. (1991). A strategy for frequency spectra of Quaternary climate records, *Climate Dynamics* 5: 227–240.

Bingham, C., Godfrey, M. and Tukey, J. (1967). Modern techniques for power spectrum estimation, *IEEE Transactions on Audio and Electroacoustics* AU-15(2): 56–66.

Blackman, R. and Tukey, J. (1958). *The Measurement of Power Spectra*, Dover Publications, New York.

Bloomfield, P. (1976). *Fourier Analysis of Time Series*, Wiley.

Boulton, G. and Payne, A. (1994). Mid-latitude ice sheets through the last glacial cycle: Glaciological and geological reconstructions, *in* J. Duplessy and M. Spyridakis (eds), *Long-Term Climatic Variations: Data and Modelling*, NATO ASI Series, Springer-Verlag, pp. 107–152.

Boulton, G., Hulton, N. and Vautravers, M. (1995). Ice-sheet models as tools for palaeoclimatic analysis: the example of the European ice sheet through the last glacial cycle, *Annals of Glaciology.*

Boulton, G., van Gijssel, K., Dalgleish, A. and Hulton, N. (1996). A synthesis of the Elsterian and post-Elsterian stratigraphy of NW Europe based on data/model comparisons, *In Press: Submitted to Quaternary Science Reviews.*

Box, G. and Cox, D. (1964). An analysis of transformations, *Journal of the Royal Statistical Society, Series B* 26: 211–252.

Box, G. and Jenkins, G. (1976). *Time Series Analysis: Forecasting and Control*, Holden-Day, San Francisco.

Bradley, R. (1985). *Quaternary Paleoclimatology*, Allen and Unwin.

Breiman, L. and Friedman, J. (1985). Estimating optimal transformations for multiple regression and correlation, *Journal of the American Statistical Association* **80**(391): 580–598.

Bretagnon, P. (1974). Termes a longues periodes dans le systeme solaire, *Astronomy and Astrophysics* **30**: 141–154.

Briffa, Atkinson and Coope (n.d.).

Broecker, W., Thurber, D., Goddard.J., Ku, T., Matthews, R. and Mesolella, K. (1968). Milankovitch hypothesis supported by precise dating of coral reefs and deep-sea sediments, *Science* **159**: 297–300.

Brouwer, D. and van Woerkom, A. (1950). The secular variations of the orbital elements of the principal planets, *Astr. Papers Amer. Ephem. Naut. Almanac* **13**(2): 81–107.

Burg, J. (1972). The relation between maximum entropy spectra and maximum likelihood spectra, *Geophysics* **37**: 375–376.

Calder, N. (1974). Arithmetic of the ice ages, *Nature* **252**: 216–218.

Chatfield, C. (1989). *The Analysis of Time Series*, Chapman and Hall.

Coope, G. (1977). Fossil coleoptera as sensitive indicators of climatic change during the Devensian cold stage, *Philosophical Transactions of the Royal Society of London, Series B* **280**: 313–340.

Croll, J. (1864). On the physical cause of the change of climate during geological epochs, *Philosophical Magazine* **28**: 121–137.

Dawson, A. (1992). *Ice Age Earth: Late Quaternary Geology and Climate*, Routledge.

de Beaulieu, J., Guiot, J. and Reille, M. (1991). Long European pollen records and quantitative reconstructions of the last climatic cycle, *in* Goodess and Palutikof (1991b), pp. 116–136.

Dettinger, M., Ghil, M., Strong, C., Weibel, W. and Yiou, P. (1995). Software expedites singular spectrum analysis of noisy time series, *EOS, Transactions of the American Geophysical Union* 76(2): 12–21. WWW ref: http://www.atmos.ucla.edu/w̃eibel/ssa/.

Diggle, P. (1990). *Time Series: A Biostatistical Introduction*, Oxford University Press.

Emiliani, C. (1955). Pleistocene temperatures, *Journal of Geology* 63: 538–575.

Evans, G., Sutherland, G., McCarthy, R. and Omlor, P. (1965). The comparison of power spectral density techniques as applied to digital data records of nonstationary processes, *Technical Report 419493*, Stanford Research Institute.

Francis, O. and Berge, M. (1993). Estimate of the radial orbit error by complex demodulation, *Journal of Geophysical Research* 98(B9): 16083–16094.

Goldthwait, R., Dreimanis, A., Forsyth, J., Carrow, P. and White, G. (1965). Pleistocene deposits of the Erie Lobe, *in* H. Wright and D. Frey (eds), *The Quaternary of the United States*, Princeton University Press, pp. 85–97.

Goodess, C. and Palutikof, J. (1991a). The UK approach to studies of climate change and radioactive waste disposal, in *Future Climate Change and Radioactive Waste Disposal* (Goodess and Palutikof 1991b), pp. 58–76.

Goodess, C. and Palutikof, J. (eds) (1991b). *Future Climate Change and Radioactive Waste Disposal*, number NSS/R257, NIREX Safety Series.

Goodess, C., Palutikof, J. and Davies, T. (1992). *The Nature and Causes of Climate Change*, Belhaven Press, London.

Guiot, J. (1990). Methodology of the last climatic cycle reconstruction in France from pollen data, *Palaeogeography, Palaeoclimatology, Palaeoecology* 80: 49–69.

Guiot, J., Reille, M., de Beaulieu, J. and Pons, A. (1992). Calibration of the climatic signal in a new pollen sequence from La Grand Pile, *Climate Dynamics* 6: 259–264.

Hastie, T. and Tibshirani, R. (1990). *Generalized Additive Models*, Chapman and Hall.

Hays, J., Imbrie, J. and Shackleton, N. (1976). Variations in the Earth's orbit: Pacemaker of the ice ages, *Science* 194(4270): 1121–1132.

Henderson-Sellers, A. and Robinson, P. (1986). *Contemporary Climatology*, Longman Scientific and Technical.

Imbrie, J. (1985). A theoretical framework for the Pleistocene ice ages, *Journal of the Geological Society of London* 142: 417–432.

Imbrie, J. and Imbrie, J. (1980). Modelling the climatic response to orbital variations, *Science* 207: 943–953.

Imbrie, J. and Imbrie, K. (1979). *The Ice Ages: Solving the mystery*, Harvard.

Imbrie, J. and Kipp, N. (1971). A new micropaleontological method for quantitative paleoclimatology: Application to a late Pleistocene Caribbean core, *in* K. Turekian (ed.), *Late Cenozoic Glacial Ages*, Yale University Press, pp. 71–147.

Imbrie, J., Berger, A., Boyle, E., Clemens, S., Duffy, A., Howard, W., Kukla, G., Kutzbach, J., Martinson, D., McIntyre, A., Mix, A., Molfino, B., Morley, J., Petersen, L., Pisias, N., Prell, W., Raymo, M., Shackleton, N. and Toggweiler, J. (1992). On the structure and origin of major glaciation cycles: 1. linear responses to Milankovitch forcing, *Paleoceanography* 7(6): 701–738.

Imbrie, J., Berger, A., Boyle, E., Clemens, S., Duffy, A., Howard, W., Kukla, G., Kutzbach, J., Martinson, D., McIntyre, A., Mix, A., Molfino, B., Morley, J., Petersen, L., Pisias, N., Prell, W., Raymo, M., Shackleton, N. and Toggweiler, J. (1993). On the structure and origin of major glaciation cycles: 2. the 100,000 year cycle, *Paleoceanography* 8(6): 699–735.

Imbrie, J., Hays, J., Martinson, D., McIntyre, A., Mix, A., Morley, J., Pisias, N., Prell, W. and Shackleton, N. (1984). The orbital theory of Pleistocene climate: support from a revised chronology of the marine $\delta^{18}O$ record, pp. 269–305.

Jacobs, J. (1994). *Reversals of the Earth's Magnetic Field*, second edn, Cambridge University Press.

Jenkins, G. and Watts, D. (1968). *Spectral Analysis and its Applications*, Holden-Day, San Francisco.

Kemp, W. and Eger, D. (1967). The relationships among sequences with applications to geological data, *Journal of Geophysical Research* 72(2): 739–751.

Kominz, M., Heath, G., Ku, T. and Pisias, N. (1979). Brunhes timescale and the interpretation of climatic change, *Earth and Planetary Science Letters* 45: 394–410.

Kopka, H. and Daly, P. (1993). *A guide to* LaTeX, Addison Wesley.

Koppen, W. and Wegener, A. (1924). *Die Klimate der Geologischen Vorzeit*, Gebruder Borntraeger, Berlin.

Kukla, G. (1970). Correlation between loesses and deep-sea sediments, *Forh. Geol. Foren. Stockholm* 92: 148–180.

Kukla, G., An, Z., Melice, J., Gavin, J. and Xiao, J. (1990). Magnetic susceptibility record in Chinese loess, *Transactions of the Royal Society of Edinburgh* 81(4): 263–288.

Kukla, G., Berger, A., Lotti, R. and Brown, J. (1981). Orbital signature of interglacials, *Nature* 290: 295–300.

Lamport.L. (1985). LaTeX*: A document preparation system*, Addison Wesley.

Laskar, J. (1986). Secular terms of classical planetary theories using the results of general theory, *Astronomy and Astrophysics* 157: 59–70.

Laskar, J. (1988). Secular evolution of the solar system over 10 million years, *Astronomy and Astrophysics* 198: 341–362.

Le Verrier, U. (1855). Recherches astronomiques, *Ann. Observ. Imp. Paris, II.*

Lowe, J. and Walker, M. (1984). *Reconstructing Quaternary Environments*, Longman Scientific and Technical.

Ludwig, K. et al. (1992). Mass-spectrometric $Th^{230} - U^{234} - U^{238}$ dating of the Devil's Hole calcite vein, *Science* 258: 284–287.

Maher, B. and Thompson, R. (1992). Paleoclimatic significance of the mineral magnetic record of the Chinese loess and paleosols, *Quaternary Research* 37: 155–170.

Mesolella, K., Matthews, R., Broecker, W. and Thurber, D. (1969). The astronomical theory of climatic change: Barbados data, *Journal of Geology* 77: 250–274.

Milankovitch, M. (1936). Mathematische klimalehre und astronomische theorie der klimaschwankungen, *in* W. Koppen and R. Geiger (eds), *Handbuch der Klimatologie*, Gebruder Borntraeger, Berlin.

Mommersteeg, H., Loutre, M., Young, R., Wijmstra, T. and Hooghiemstra, H. (1995). Orbital forced frequencies in the 975000 year pollen record from Tenagi Philippon (Greece), *Climate Dynamics* 11: 4–24.

Moore, T., Pisias, N. and Heath, G. (1977). Climate changes and lags in Pacific carbonate preservation, sea surface temperature and global ice volume, *The Fate of Fossil Fuel CO2 in the Oceans*, Plenum Press.

ODP Shipboard Scientific Party (1988). 111: 253–346.

Penland, C., Ghil, M. and Weickmann, K. (1991). Adaptive filtering and maximum entropy spectra with application to changes in atmospheric angular momentum, *Journal of Geophysical Research* 96(D12): 22659–22671.

Petersen, E. and Larsen, S. (1978). A statistical study of a composite isotopic paleotemperature series from the last 700,000 years, *Tellus* 30: 193–200.

Pisias, N. and Moore, T. (1981). The evolution of Pleistocene climate : A time series approach, *Earth and Planetary Science Letters* 52: 450–458.

Pisias, N. et al. (1973). Spectral analysis of late Pleistocene-Holocene sediments, *Quaternary Research* 3: 3–9.

Pisias, N., Mix, A. and Zahn, R. (1990). Nonlinear response in the global climate system: Evidence from benthic oxygen isotope record in core RC13-110, *Paleoceanography* 5(2): 147–160.

Pollard, D. (1982). A simple ice-sheet model yields realistic 100 kyr glacial cycles, *Nature* 296: 334–341.

Priestley, M. (1981). *Spectral Analysis and Time Series, Vol 1 and 2*, Academic Press.

Ruddiman, W., Raymo, M. and McIntyre, A. (1986). Matuyama 41,000 year cycles: North Atlantic ocean and Northern hemisphere ice sheets, *Earth and Planetary Science Letters* **80**: 117–129.

S-PLUS (1996). Statistical Sciences Europe, 52 Sandfield Road, Headington, Oxford, OX3 7RJ, UK.

Saltzman, B. and Maasch, K. (1990). A first-order global model of the late Cenozoic climatic change, *Transactions of the Royal Society of Edinburgh* **81**: 315–325.

Shackleton, N. and Opdyke, N. (1973). Oxygen isotope and paleomagnetic stratigraphy of equatorial Pacific core v28-238, *Quaternary Research* **3**: 39–55.

Shackleton, N., Berger, A. and Peltier, W. (1990). An alternative astronomical calibration of the lower Pleistocene timescale based on ODP site 677, *Transactions of the Royal Society of Edinburgh* **81**: 251–261.

Shackleton, N., Hagelberg, T. and Crowhurst, S. (1995). Evaluating the success of astronomical tuning: Pitfalls of using coherence as a criterion for assessing pre-Pleistocene timescales, *Paleoceanography* **10**(4): 693–697.

Sharaf, S. and Boudnikova, N, A. (1967). Secular variations of the Earth's orbit which influences the climates of the geological past, *Trudy Institute Theoreticheskol Astronomii, Leningrad* **11**(4): 231–261.

Tabony, R. (1979). A spectral filter analysis of long period records in england and wales, *Meteorological Magazine* **108**: 102–112.

Tauxe, L., Deino, A., Behrensmeyer, A. and Potts, R. (1992). Pinning down the Brunhes/Matuyama and upper Jaramillo boundaries: a reconciliation of orbital and isotopic time scales, *Earth and Planetary Science Letters* **109**: 561–572.

Thompson, R. (1994). Complex demodulation and the estimation of the changing continentality of Europe's climate, *International Journal of Climatology.*

Thomson, D. (1982). Spectrum estimation and harmonic analysis, *Proceedings of the IEEE.*

Thomson, D. (1990a). Quadratic inverse spectrum estimates: applications to palaeoclimatology, *Philosophical Transactions of the Royal Society of London* **332**: 539–597.

Thomson, D. (1990b). Time series analysis of Holocene climatic data, *Philosophical Transactions of the Royal Society of London* **330A**: 601–616.

Tibshirani, R. (1988). Estimating transformations for regression via additivity and variance stabilization, *Journal of the American Statistical Association* **83**(402): 394–405.

Tudhope, A., Chilcott, C., Fallick, A., Jebb, M., Shimmield, G. and Dalgleish, A. (1995). Recent changes in climate in the far Western equatorial Pacific and their relationship to the Southern Oscillation, *Earth and Planetary Science Letters* **136**: 575–590.

Tukey, J. (1961). Discussion, emphasising the connection between analysis of variance and spectrum analysis, *Technometrics* **3**: 191–219.

van den Heuvel, E. (1966). On the precession as a cause of Pleistocene variations of the Atlantic Ocean water temperatures, *Geophysical Journal of the Royal Astronomical Society* **11**: 323–336.

Weedon, G. and Shimmield, G. (1991). Late Pleistocene upwelling and productivity variations in the Northwest Indian Ocean deduced from spectral analysis of geochemical data from sites 722 and 724, *Proceedings of the ODP, Scientific Results*, Vol. 117.

Whittaker, E. and Robinson, G. (1932). *The Calculus of Observations*, Blackie, London.

Winograd, I., Coplen, T., Landwehr, J., Riggs, A., Ludwig, K., Szabo, B., Kolesar, P. and Revesz, K. (1992). Continuous 500,000 year climate record from vein calcite in Devil's Hole, Nevada, *Science* **258**: 255–260.

Yiou, P., Genthon, C., Ghil, M., Jouzel, J., Le Treut, H., Barnola, J., Lorius, C. and Korotkevitch, Y. (1991). High frequency paleovariability in climate and CO_2 levels from Vostok ice core records, *Journal of Geophysical Research* **96**(B12): 20365–20378.